STUDIES ON PERFORMANCE CHARACTERISTICS OF OPEN-CYCLE DIAGONAL TYPE MHD POWER GENERATOR

By

Masaharu YOSHIDA

August 1980

Department of Electrical Engineering

Kyoto University, Kyoto, Japan

STUDIES ON PERFORMANCE CHARACTERISTICS OF OPEN-CYCLE DIAGONAL TYPE MHD POWER GENERATOR

By

Masaharu YOSHIDA

August 1980

Department of Electrical Engineering

Kyoto University, Kyoto, Japan

ACKNOWLEDGEMENTS

The author wishes to express his sencere and hearty appreciation to Professor Juro Umoto of Kyoto University for his continual guidances and encouragements throughout the course of the present work.

The author also wishes to express his thanks to Associate Professor Takehisa Hara and Instructor Tsuguo Ando of Department of Electrical Engineering, Kyoto University for their useful advices.

The author makes a grateful acknowledgment for several valuable advices of Associate Prefessor Kiyoshi Yoshikawa, Instructor Motoo Ishikawa, and Dr. Daijiro Tanaka of Institute of Atomic Energy.

The author also acknowledges hearty assistances of Miss Yoko Shibata, Mr. Kiyotoshi Komaya, Mr. Toshikazu Inui, and other staffs of Professor J. Umoto's Laboratory.

All numerical computations were performed at the Data Processing Center, Kyoto University, Kyoto, Japan.

CONTENTS

CHAPTER 1

GENERAL INTRODUCTION

1.1 Importance and Present Status of MHD Power Generation

As is generally known, the amount of electrical energy consumption is increasing all over the world, and on the other hand, it is foreseen that production of crude oil which is the present main primary energy will be decreased in early future [1-4]. Further, we have to wait for many years until nuclear energy will be able to be utilized as the main primary energy [5]. Accordingly, we should economize and use effectively fossil fuels such as petroleum and coal, and for the effective use of them many new ideas have been proposed and many means are being developed.

Magnetohydrodynamic (MHD) power generation is very important one of those means, by which in high efficiency thermal energy of a large amount of high temperature gas plasma can be converted into electrical energy according to Faraday's law by running it across a strong magnetic field with high speed .

MHD generators are classified into two types of the open- and the closed-cycles according to sort of the working gas. In the open-cycle MHD generator, a combustion gas of fossil fuel is used, and in the closed-cycle one, a noble gas such as A or He is done, whose thermal energy will be given by future nuclear fusion reactor, sun furnace,

etc. It is expected that the turbine efficiency of the open-cycle MHD generator exceeds 60% and the one of the closed-cycle generator 70%. Consequently, an MHD-steam power plant, in which the open-cycle MHD generator and the conventional turbine generator of the thermal efficiency of about 40% are coupled, will be able to have the total thermal efficiency of about 50% [6]. As a result, it is expected that fossil fuel is economized and thermal pollusion is much reduced.

In addition, the alkali metal such as K or Cs, which is seeded into the combustion gas to heighten the electrical conductivity, reacts to S contained in the gas, and it can be almost collected in the form of K_2SO_4 or Cs_2SO_4. Consequently, air pollution due to SO_2 gas can be prevented, and even S-rich fuel of low-grade can be used.

For about 20 years since the first success in MHD power generation in 1959 by Kantrowitz, Rosa, et al., at AVCO Everett Research Laboratory in USA [7], many workers have reported a large number of excellent experimental and theoretical studies on the open-cycle MHD generator.

What is specially noteworthy in the experimental study is achievement of the U-25 pilot plant driven by combustion gas of petroleum and natural gas in High Temperature Institute in USSR. Namely in 1977, the RM-duct was successfully operated during long time of about 250 hours with generated output of 10 MW, and the ID-duct was done with high output of 20.4 MW for 30 minutes [6, 8]. Further, in USSR, it has been planned that the 500 MW commercial MHD power plant with coal combustion gas is set in operation in upper 1980's.

In USA, for example, in 1976, Mark VI of AVCO was successfully operated for about 100 hours under electrical stresses comparable to those contemplated for future efficient operation [9]. Moreover in University of Tenessee Space Institute (UTSI), et al., a large scale experiments aimed at setting in running of the commercial coal fired

MHD generator in 1980's are being carried out [10-12].

In Japan, experimental researches of the open-cycle MHD generator driven by combustion gas of light oil have been carried out mainly in Electrotechnical Laboratory as a National Project since 1966 [13-16].

In this connection, it is preestimated that the closed-cycle MHD generator has advantage that it can be operated in lower temperature and can give higher efficiency and output power density than the open-cycle one. In USA, Europe, Japan, et al., fundamental experiments and theoretical analyses of the closed-cycle one are performed eagerly and continually [17-21].

1.2 Purpose and Significance of This Thesis

1.2.1 Diagonal type generator

From the point of connection of electrodes and load resistances, MHD generators are classified into three kinds of Faraday, Hall, and diagonal types. In general, the Faraday type generator can give the heihest output power density and efficiency among the above three types. However, it needs many distributed output electrode pairs, and each load resistance is connected between each electrode pair. Consequently, a power plant system with the Faraday type generator requires many DC-AC inverters, and so the system will be complicated.

The Hall type generator can be operated with only a single load in principle, but it has been seen that the Hall type needs high Hall parameter to give good performance. However, it is difficult to obtain high Hall parameter in combustion gas plasma in practice. In addition, as shown later on in chapter 3, the Hall type can not necessarily give so good performance even in the case of high Hall parameter.

As an intermediate of the above two type generators, the diagonal

type generator is thought to give output power density and efficiency compared favorably with the Faraday type even for comparatively low Hall parameter. It can be operated with a single load or a few ones, and therefore, it needs only one or a few DC-AC inverters. Thus it has merits of both the Faraday and the Hall types.

From the above mentioned, it is seen that the diagonal type generator has hopeful prospect as a large scale commercial one. In fact, the R-duct of U-25 [22], the duct of Mark VI of AVCO [9, 23, 24], the generator ducts in UTSI [10, 11, 25-28], and the ones in USA and USSR facility [29, 30] are all diagonal type.

1.2.2 Past analyses

Up to now, many workers have investigated numerically electrical characteristics of central or end region of MHD generators with two- or three-dimensional theory using conformal transformation, finite difference method (FDM), finite element method (FEM), equivalent circuit method (ECM), etc., and they have studied the whole electrical and gasdynamical characteristics by a conventional quasi-one-dimensional MHD theory.

Hurwitz, et al. [31], and Dzung [32] calculated two-dimensionally the local electrical characteristics of the MHD generators by the conformal transformation. In this method, there are not considered nonuniformity of the working gas plasma, leakage current on the insulating wall surface, etc. Besides, their method can not be applicable to analysis of the whole generator.

In Refs. 33 and 34, there are seen some examples of two-dimensional numerical analyses of local electrical characteristics of the diagonal type generators by the FDM. Although it is said that numerical calculation by the FDM can give the accurate solutions, to obtain them, we need many meshes or node points and so much memory size, central proccessing unit (cpu) time, etc. Also, it is troublesome to take into consideration the leakage current on the insulating wall surfaces in the FDM. Consequently, this method is not

applicable to analysis of whole generator.

The FEM was applied to two- and three-dimensional numerical analyses of local characteristics of the MHD generator by Hara, et al. [35]. The numerical solution by the FEM can converge rapidly to an accurate one by using coarser meshes than in the case by the FDM. Therefore, the FEM is effective to reduce memory size and cpu time. However, it is thought to be difficult to apply the FEM to analysis of the whole generator, too.

As another method of two- or three-dimensional analysis, the ECM is known. Gruber [36], Ogiwara [37], Celinski [38,39], Shirakata [40], et al. have derived two-dimensional equivalent circuits of the Faraday and the Hall type generators, and investigated the electrical characteristics of the generators. Especially the calculation results by the Shirakata's equivalent circuit employing a negative resistance have enough agreed with the experimental ones of a small scale Faraday generator. However, their equivalent circuits can not be applied to analysis of the diagonal type generator. And though boundary layer and leakage currents are taken account in the circuits, yet ion-slip and finite electrode segmentation effects are not considered. In addition, they have not attempted to analyse not only electrical but also gasdynamical performances of the whole generator.

In general, the ECM has desirable advantages that it needs only fairly small memory size and cpu time to calculate the generator characteristics compared with the FDM and the FEM. Therefore, if we can find out a simple equivalent circuit effectively applicable to the diagonal type, it is thought possible to analyse and investigate two- or three-dimensionally not only the local electrical characteristics but also the whole performances of the generator by using both the equivalent circuit and the MHD flow equations.

As previously described, the whole generator performances have been studied so far by means of the conventional quasi-one-dimensional MHD theory [41,42]. However, by this theory, the generator performances can not be evaluated and grasped so accurately, because in the

theory the socalled end effect of the generator can not be considered and the effects of the finite electrode segmentation, the boundary layer, etc. are considered only in coarse approximation.

1.2.3 Purpose and significance of this thesis

As described in subsections 1.2.1 and 1.2.2, the diagonal type MHD generator has hopeful prospect as a large scale commercial generator, but there are remained many problems to be solved and clarified theoretically. The ECM has desirable advantages that it needs only small memory size and short cpu time for calculating the generator characteristics compared with the FDM and the FEM. However, the ECM which can be applied to the diagonal type generator has not been found out by other workers.

In view of the above-mentioned, this thesis intends to get some new reliable two-dimensional equivalent circuit of a large scale open-cycle diagonal type generator, to clarify the basic electrical characteristics of the central and end regions of the generator, to derive new quasi-two-dimensional theory of whole electrical and gasdynamical performances of the generator from the above circuit and the MHD flow equations, to make clear the whole generator performance characteristics, and so on.

By attaining the above purposes, the thesis will present sufficiently useful data to optimum design of excellent commercial scale diagonal type generators.

1.3 Synopsis of This Thesis

In chapter 2, from a generalized Ohm's law considering the Hall and the ion-slip effects, a new two-dimensional equivalent circuit of the diagonal type generator with single load is derived, by which the electrical characteristics such as current or potential distributions, output power, its density, electrical efficiency of the

generator can be calculated. In the circuit, finite electrode segmentation effect, leakage current on the insulating wall surfaces, etc. are considered. The circuit can be easily applied to both the Hall and the Faraday type generators.

In chapter 3, the equivalent circuit derived in chapter 2 is applied to analysis of the electrical characteristics of the central part of large scale diagonal and Hall type generators. First of all, it is confirmed that the relations between the Hall voltage per one electrode pitch and load current calculated by the ECM agree well with the ones by the FDM and the FEM, and so the author's new ECM gives reliable results. And the fewest number of space elements per one electrode pitch region to be used for obtaining sufficiently accurate calculation results by the ECM is determined. Next, the influences of the leakage current, the ion-slip effect, the boundary layer, the finite electrode segmentation, the Hall parameter, the diagonal angle, etc. on the generator characterisitcs are investigated numerically in detail.

In chapter 4, the circuit derived in chapter 2 is applied to analysis of inlet and exit regions of a large scale diagonal type generator. It is ascertained that current and potential distributions obtained by the ECM agree with the one by the FDM. Further, there are examined influences of the applied magnetic flux distribution, the load current, the number of output electrodes installed in the generator duct ends. In this connection, the lengthes of the nozzle and the diffuser in the flow direction to be considered for obtaining sufficiently accurate calculation results are determined.

In chapter 5, first, there are introduced a new quasi-two-dimensional theory which can numerically analyse whole electrical and gasdynamical performances of the single-load diagonal type generator with no boundary layer. Next, with many numerical calcualtion results by the new theory concerning a large scale diagonal type generator of constant square cross-section driven by combustion gas

of heavy oil fuel, influences of the applied magnetic flux distribution, the finite electrode segmentation, number of output electrode, etc. on the output power, electrical efficiency etc. of the whole generator, current concentration at the output electrode ends, etc. are clarified. Also the results obtained by the quasi-two-dimensional and ideal quasi-one-dimensional theories are comparatively studied.

In chapter 6, there is proposed a improved quasi-two-dimensional theory which can numerically analyse whole electrical and gasdynamical performances of the diagonal type generator in which turbulent velocity and thermal boundary layers are assumed to occur. With respect to a large scale linearly-diverging diagonal generator with the thermal input of about 2,000 MW driven by combustion gas of heavy oil, influences of the length, wall temperature, and diverging angle of the duct, the diagonal angle, the load current etc. on performance characteristics of the single-load generator are examined in detail. Furthermore, the characteristics of the multiple-load generator are calculated and compared with the ones of the single-load generator.

CHAPTER 2

DERIVATION OF TWO-DIMENSIONAL EQUIVALENT CIRCUIT OF SINGLE-LOAD GENERATOR

2.1 Introduction

As already described, Celinski [38,39], Shirakata [40] et al. have introduced two-dimensional equivalent circuits of the Faraday and the Hall type generators. However, their circuits can not be applied to analysis of electrical characteristics of a diagonal type generator. Further, in their circuits, although influences of boundary layer and leakage current on the insulating wall surfaces are considered, ion-slip, finite electrode segmentation effects, etc. are not considered.

Accordingly this chapter is devoted to derivation of a new two-dimensional equivalent circuit of the single-load diagonal type generator. First, from a generalized Ohm's law considering both Hall and ion-slip effects, is derived a new two-dimensional equivalent four-terminal circuit for any space element (see subsection 2.2.1) in not only core flow but also boundary layer in the diagonal type generator duct.

Next, the equivalent network of the diagonal type generator is accomplished, in which the leakage current on the insulating wall surface, the boundary layer, the finite electrode segmentation effect, etc. are taken into consideration. It is shown that the net-

work can be easily applied to both the Faraday and the Hall generators.

Finally, formulation of the electrical characteristics such as the Joule heat, the generated output, the electrical efficiency of the generator are carried out.

2.2 Space Element and Its Equivalent Circuit [43-45]

2.2.1 Equivalent four-terminal circuit with voltage sources

(1) Equivalent circuit for space element in gas core flow

Figure 2.1 shows a diagonal type MHD generator with the x, y, and z coordinate axes used, in which pairs of anodes and cathodes 1-1' to N-N' are arranged at a slant angle φ from a working gas flow direction, which is called the diagonal angle. In the figure, $\mathbb{B}$, $\mathbb{u}$, and R_L are the magnetic flux density, the gas velocity, and the load resistance, respectively.

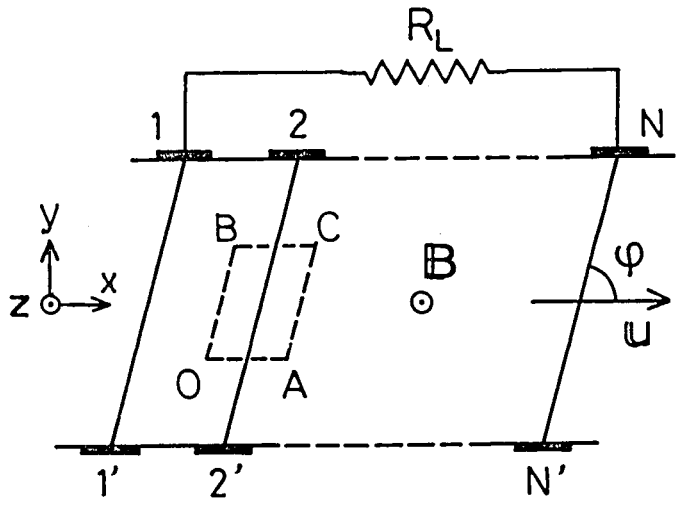

Fig. 2.1 Single-load diagonal type generator.

In general, physical quantities of the working gas plasma are not spatially uniform in a generator duct. Hence, let us divide a generator duct space into a large number of space elements, in which the values of the electrical conductivity σ, the Hall parameter β, the current density $\mathbf{J}$, the electric field $\mathbf{E}$, the magnetic flux density $\mathbf{B}$, the velocity $\mathbf{u}$, etc. can be assumed constant. This assumption is valid in a short distance of one electrode pitch in the core flow, because gasdynamical quatities are almost constant there, Firstly, for such space elements, we derive a new equivalent circuit.

Figure 2.2(a) shows one of the space elements in the generator shown in Fig. 2.1, in which s_e, h_e, and d_e are the length, height, and width, respectively, of the space element, where d_e is taken as the generator duct width in the two-dimensional analysis.

Now, as is well known, when the gradient of the partial electron pressure can be neglected as in usual MHD generator duct, a generalized Ohm's law is given by

$$\mathbf{J} = \sigma(\mathbf{E} + \mathbf{u}\times\mathbf{B}) - \frac{\beta}{B}(\mathbf{J}\times\mathbf{B}) + \frac{\beta\,\beta_i}{B^2}(\mathbf{J}\times\mathbf{B})\times\mathbf{B} \quad , \qquad (2.1)$$

where β and β_i are the Hall parameters for electron and ion, respectively.

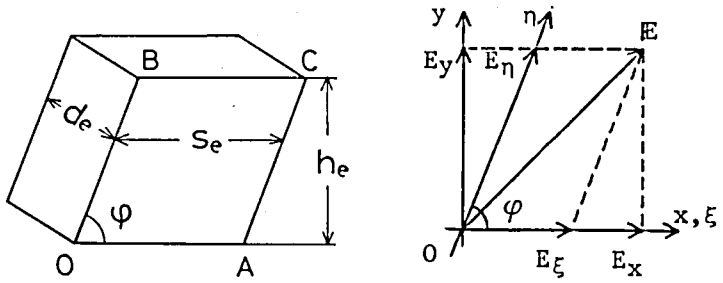

(a) Space element (b) Coordinates

Fig. 2.2 Space element and coordinates.

Next, let us assume $\mathbb{E}$, $\mathbb{J}$, $\mathbb{B}$, and $\mathbb{u}$ as follows:

$$\left.\begin{aligned} \mathbb{E} &= (E_x, E_y, 0), \quad \mathbb{J} = (J_x, J_y, 0), \\ \mathbb{B} &= (0, 0, B), \quad \mathbb{u} = (u, 0, 0). \end{aligned}\right\} \tag{2.2}$$

Then, the x and y components of Eq. (2.1) are expressed by

$$\left.\begin{aligned} J_x &= \sigma' E_x - \beta' J_y, \\ J_y &= \sigma' (E_y - uB) + \beta' J_x, \end{aligned}\right\} \tag{2.3}$$

where

$$\left.\begin{aligned} \sigma' &= \sigma / (1 + \beta \beta_i), \\ \beta' &= \beta / (1 + \beta \beta_i). \end{aligned}\right\} \tag{2.4}$$

Equations (2.3) are rewritten as

$$\begin{pmatrix} E_x \\ E_y - uB \end{pmatrix} = \frac{1}{\sigma'} \begin{pmatrix} 1 & \beta' \\ -\beta' & 1 \end{pmatrix} \begin{pmatrix} J_x \\ J_y \end{pmatrix}. \tag{2.5}$$

in matrix form.

Now, to simplify the analysis, let us introduce a new oblique coordinates (ξ, η) as shown in Fig. 2.2(b) for the space element given in Fig. 2.2(a). Then, the voltages V_ξ and V_η in the ξ and η directions, respectively, between both end surfaces of the space element are given by

$$\begin{pmatrix} V_\xi \\ V_\eta \end{pmatrix} = - \begin{pmatrix} s_e & 0 \\ h_e \cot\varphi & h_e \end{pmatrix} \begin{pmatrix} E_x \\ E_y \end{pmatrix}. \tag{2.6}$$

Also, the currents I_ξ and I_η in the ξ and η directions, respectively, in the space element are obtained as follows:

$$\begin{pmatrix} I_\xi \\ I_\eta \end{pmatrix} = \begin{pmatrix} d_e\, h_e & 0 \\ 0 & d_e\, s_e \sin\varphi \end{pmatrix} \begin{pmatrix} J_\xi \\ J_\eta \end{pmatrix} , \qquad (2.7)$$

where

$$\begin{pmatrix} J_\xi \\ J_\eta \end{pmatrix} = \begin{pmatrix} 1 & \cos\varphi \\ 0 & \sin\varphi \end{pmatrix}^{-1} \begin{pmatrix} J_x \\ J_y \end{pmatrix} . \qquad (2.8)$$

Using Eqs. (2.5) to (2.8), we obtain

$$\begin{pmatrix} V_\xi \\ V_\eta + e_\eta \end{pmatrix} = \begin{pmatrix} R_\xi & R_{\xi\eta} \\ -R_{\eta\xi} & R_\eta \end{pmatrix} \begin{pmatrix} -I_\xi \\ -I_\eta \end{pmatrix} , \qquad (2.9)$$

in which

$$\left.\begin{aligned} e_\eta &= h_e\, u\, B, \\ R_\xi &= s_e / (\sigma'\, d_e\, h_e), \\ R_{\xi\eta} &= (\beta' + \cot\varphi) / (\sigma'\, d_e), \\ R_{\eta\xi} &= (\beta' - \cot\varphi) / (\sigma'\, d_e), \\ R_\eta &= h_e / (\sigma'\, d_e\, s_e \sin^2\varphi). \end{aligned}\right\} \qquad (2.10)$$

From Eq. (2.9), an equivalent four-terminal circuit for the space element in Fig. 2.2(a) is derived as shown in Fig. 2.3(a), where the voltage sources $v_{\xi\eta}$ and $v_{\eta\xi}$ are

$$v_{\xi\eta} = R_{\eta\xi}\ I_\eta, \quad v_{\eta\xi} = R_{\xi\eta}\ I_\xi . \qquad (2.11)$$

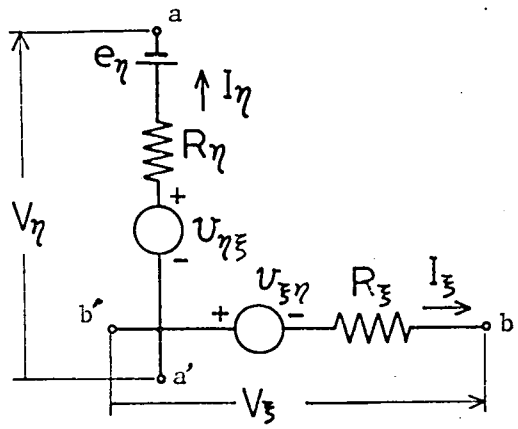

(a) Equivalent four-terminal circuit.

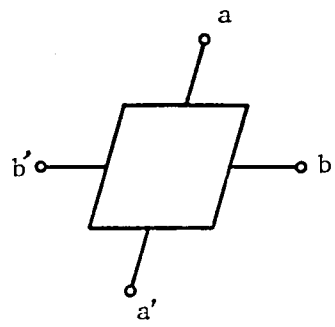

(b) Simplified illustration of (a).

Fig. 2.3 Equivalent four-terminal circuit with voltage sources for space element.

In Eqs. (2.10), (2.11), and Fig. 2.3(a), e_η is the Faraday electromotive force, R_ξ and R_η are the internal resistances of the working gas plasma in the ξ and η directions, respectively, and $v_{\xi\eta}$ and $v_{\eta\xi}$ are the voltages induced by I_η and I_ξ in the ξ and η directions, respectively, which contain influence of the Hall effect.

In addition, Fig. 2.3(b) is a simplified illustration of the equivalent circuit in (a).

(2) Equivalent circuit for space element in boundary layer

When the duct wall temperature is lower than the core flow temperature, not only velocity boundary layer but also thermal one grows along the duct wall surface. In the boundary layer, the values of σ, u, J_x, E_y, etc. vary steeply in the y direction. Accordingly in a space element in the bounday layer, the assumption that the magnitudes of the physical quantities are constant in the element can not be held so long as space elements of very small size are not adopted. Therefore, according to Rosa's idea [46], we will utilize the averaged

Ohm's law in the element.

Now, let us consider the boundary layer of a gas flow which is developed on a semi-infinitely wide flat plate parallel to the x-z plane, which corresponds to the generator duct wall. When it is assumed that physical quantities in the boundary layer depend on only y, the following Maxwell equations for steady state

$$\text{rot } \mathbb{E} = 0, \quad \text{div } \mathbb{J} = 0, \tag{2.12}$$

are reduced to

$$\frac{d E_x}{d y} = 0, \quad \frac{d J_y}{d y} = 0, \tag{2.12'}$$

respectively, under the assumption of Eqs.(2.2). From these equations, we obtain

$$E_x = \text{const.}, \quad J_y = \text{const.} \tag{2.13}$$

In this connection, E_y, J_x, σ' , β' , etc. are, of course, functions of y only by the above assumption.

Then, on the average in the y direction in the boundary layer, the first equation of Eqs. (2.3) is transformed as follows:

$$\langle J_x \rangle = \langle \sigma' \rangle E_x - \langle \beta' \rangle J_y , \tag{2.14}$$

where < > denotes an averaged value in the y direction. Next, by averaging in the y direction an equation which is obtained by eliminating J_x from Eqs. (2.3), we get

$$\left\langle \frac{1+\beta'^2}{\sigma'} \right\rangle J_y = \langle E_y - u B \rangle + \langle \beta' \rangle E_x. \tag{2.15}$$

Eliminating E_x from Eqs. (2.14) and (2.15), we obtain

$$J_y = \frac{\langle\sigma'\rangle}{G}\langle E_y - uB\rangle + \frac{\langle\beta'\rangle}{G}\langle J_x\rangle \quad , \tag{2.16}$$

where

$$G = \langle\sigma'\rangle\langle\frac{1+\beta'^2}{\sigma'}\rangle - \langle\beta'\rangle^2 \quad . \tag{2.17}$$

Equations (2.14) and (2.16), which express the averaged Ohm's law in the boundary layer, are rewritten as

$$\begin{pmatrix} E_x \\ \langle E_y - uB\rangle \end{pmatrix} = \frac{1}{\langle\sigma'\rangle}\begin{pmatrix} 1 & \langle\beta'\rangle \\ -\langle\beta'\rangle & G \end{pmatrix}\begin{pmatrix} \langle J_x\rangle \\ J_y \end{pmatrix} \quad , \tag{2.18}$$

in matrix form.

Then, the voltages V_ξ and V_η are given by

$$\begin{pmatrix} V_\xi \\ V_\eta \end{pmatrix} = -\begin{pmatrix} s_e & 0 \\ h_e \cot\varphi & h_e \end{pmatrix}\begin{pmatrix} E_x \\ \langle E_y\rangle \end{pmatrix} \quad , \tag{2.19}$$

and the currents I_ξ and I_η by

$$\begin{pmatrix} I_\xi \\ I_\eta \end{pmatrix} = \begin{pmatrix} d_e h_e & 0 \\ 0 & d_e s_e \sin\varphi \end{pmatrix}\begin{pmatrix} \langle J_\xi\rangle \\ J_\eta \end{pmatrix} \quad , \tag{2.20}$$

where

$$\begin{pmatrix} \langle J_\xi\rangle \\ J_\eta \end{pmatrix} = \begin{pmatrix} 1 & \cos\varphi \\ 0 & \sin\varphi \end{pmatrix}^{-1}\begin{pmatrix} \langle J_x\rangle \\ J_y \end{pmatrix} \quad . \tag{2.21}$$

Using Eqs. (2.18) to (2.21), we obtain

$$\begin{pmatrix} V_\xi \\ V_\eta + e_\eta \end{pmatrix} = \begin{pmatrix} R_\xi & R_{\xi\eta} \\ -R_{\eta\xi} & R_\eta \end{pmatrix} \begin{pmatrix} -I_\xi \\ -I_\eta \end{pmatrix} , \qquad (2.22)$$

in which

$$\left.\begin{aligned} e_\eta &= h_e \langle u \rangle B, \\ R_\xi &= s_e / (\langle \sigma' \rangle d_e h_e), \\ R_{\xi\eta} &= (\langle \beta' \rangle + \cot\varphi) / (\langle \sigma' \rangle d_e), \\ R_{\eta\xi} &= (\langle \beta' \rangle - \cot\varphi) / (\langle \sigma' \rangle d_e), \\ R_\eta &= h_e (G + \cot^2\varphi) / (\langle \sigma' \rangle d_e s_e). \end{aligned}\right\} \qquad (2.23)$$

By comparing Eq. (2.22) with Eq. (2.9), it is seen that an equivalent circuit for the space element in the boundary layer has the same form as the one in the core flow shown in Fig. 2.3(a).

2.2.2 Equivalent four-terminal circuit with current sources

In the previous subsection, we derived the equivalent circuit with voltage sources for the space element in the MHD generator. Here let us introduce another type of equivalent circuit.

Now, Eq. (2.9) or (2.22) is transformed as follows:

$$\begin{pmatrix} -I_\xi \\ -I_\eta \end{pmatrix} = \begin{pmatrix} G_\xi & -G_{\xi\eta} \\ G_{\eta\xi} & G_\eta \end{pmatrix} \begin{pmatrix} V_\xi \\ V_\eta + e_\eta \end{pmatrix} , \qquad (2.24)$$

where

$$\begin{pmatrix} G_\xi & -G_{\xi\eta} \\ G_{\eta\xi} & G_\eta \end{pmatrix} = \begin{pmatrix} R_\xi & R_{\xi\eta} \\ -R_{\eta\xi} & R_\eta \end{pmatrix}^{-1} , \qquad (2.25)$$

in which

$$
\left.
\begin{aligned}
G_\xi &= R_\eta / \Delta, \\
G_{\xi\eta} &= R_{\xi\eta} / \Delta, \\
G_{\eta\xi} &= R_{\eta\xi} / \Delta, \\
G_\eta &= R_\xi / \Delta, \\
\Delta &= R_\xi R_\eta + R_{\xi\eta} R_{\eta\xi}.
\end{aligned}
\right\} \qquad (2.25')
$$

From Eq. (2.24), we can derive an equivalent circuit shown in Fig. 2.4, in which the current sources $G_{\xi\eta}\, e_\eta$ and $G_{\eta\xi}\, e_\eta$ are contained. This circuit is essentially the same as the circuit with voltage

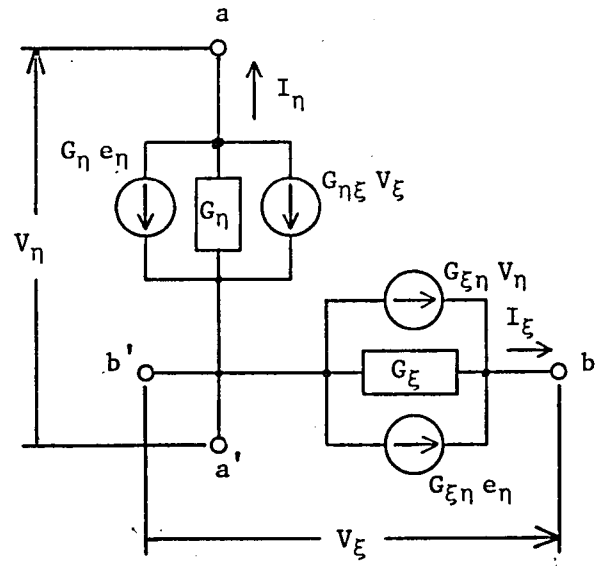

Fig. 2.4 Equivalent four-terminal circuit with current sources.

sources in Fig. 2.3(a); the former is used when node potentials are unknown, while the latter is used when loop currents are unknown. When the former is adopted to the analysis of Faraday generator, it needs much cpu time and memory size. Accordingly in this thesis, the former is not used.

2.2.3 Equivalent four-terminal circuit with negative resistance

For the Faraday type generator, an equivalent circuit with negative resistance has been proposed by Shirakata [40]. For the diagonal type generator, this type of circuit is derived as follows.

The resistance matrix in Eq. (2.9) or (2.22) can be transformed to the following form

$$\begin{pmatrix} R_\xi & R_{\xi\eta} \\ -R_{\eta\xi} & R_\eta \end{pmatrix} = \begin{pmatrix} R_\xi + R_{\eta\xi} & R_{\eta\xi} + R_{\xi\eta} \\ 0 & R_\eta + R_{\eta\xi} \end{pmatrix} + \begin{pmatrix} -R_{\eta\xi} - R_{\eta\xi} \\ -R_{\eta\xi} - R_{\eta\xi} \end{pmatrix} . \tag{2.26}$$

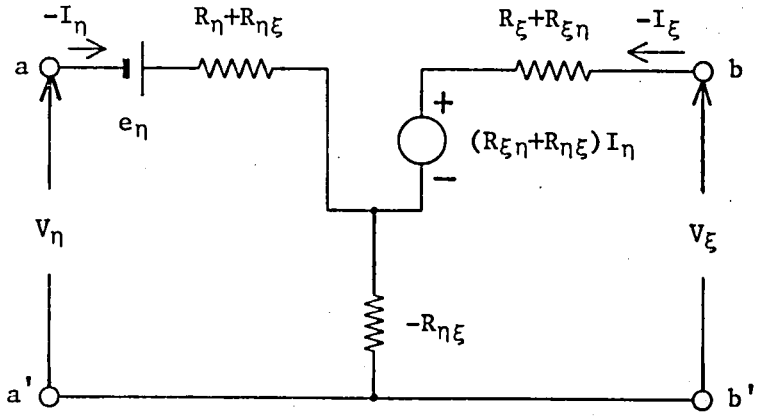

Fig. 2.5 Equivalent four-terminal circuit with negative resistance (1).

Then, Eq. (2.9) or (2.22) is rewritten as follows:

$$\begin{pmatrix} V_\xi \\ V_\eta \end{pmatrix} = \left\{ \begin{pmatrix} R_\xi + R_{\eta\xi} & R_{\eta\xi} + R_{\xi\eta} \\ 0 & R_\eta + R_{\eta\xi} \end{pmatrix} + \begin{pmatrix} -R_{\eta\xi} - R_{\eta\xi} \\ -R_{\eta\xi} - R_{\eta\xi} \end{pmatrix} \right\} \begin{pmatrix} -I_\xi \\ -I_\eta \end{pmatrix} . \tag{2.27}$$

This equation brings forth a four-terminal equivalent circuit with negative resistance $-R_{\eta\xi}$ as shown in Fig. 2.5. This circuit may be redrawn as Fig. 2.6 in comparison with the circuit in Fig. 2.3(a). The equivalent circuit with negative resistance, however, is not utilized in numerical analysis in this thesis, because the circuit equations are more or less complicated than those in the circuit with voltage sources.

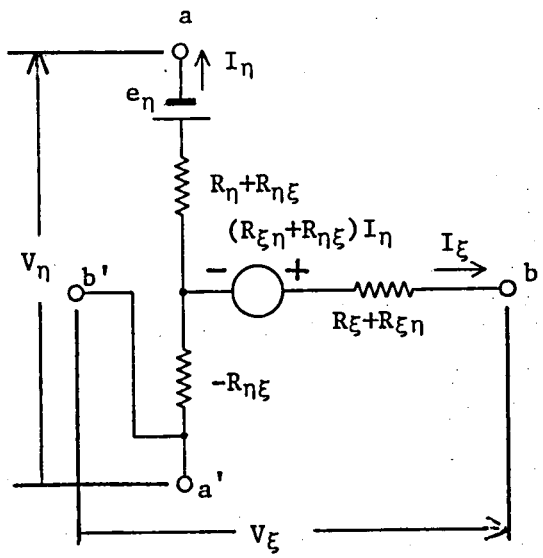

Fig. 2.6 Equivalent four-terminal circuit with negative resistance (2).

2.3 Application of Equivalent Circuit to Multi-Electrode Generators

2.3.1 Diagonal type generator

(1) Diagonal type generator

Here, the equivalent circuit derived in section 2.2 is applied to the analysis of multi-electrode diagonal generator shown in Fig. 2.1. One space element must be taken very small compared with the whole volume of generator, since gas property in the generator is not spatially uniform. If each space element is expressed by the equivalent circuit shown in Fig. 2.3(a), the diagonal generator can be represented by one equivalent circuit. Now, for convenience, let us devide space between a pair of anode and cathode into the anode boundary layer, the core flow, and the cathode boundary layer. Then, in Fig. 2.2(a), s_e and h_e are chosen as the electrode pitch s and each height of the layers, respectively. Also, the space near the electrode pairs i-i' and (i+1)-(i +1)' (i=1, 2, ..., N; N is the number

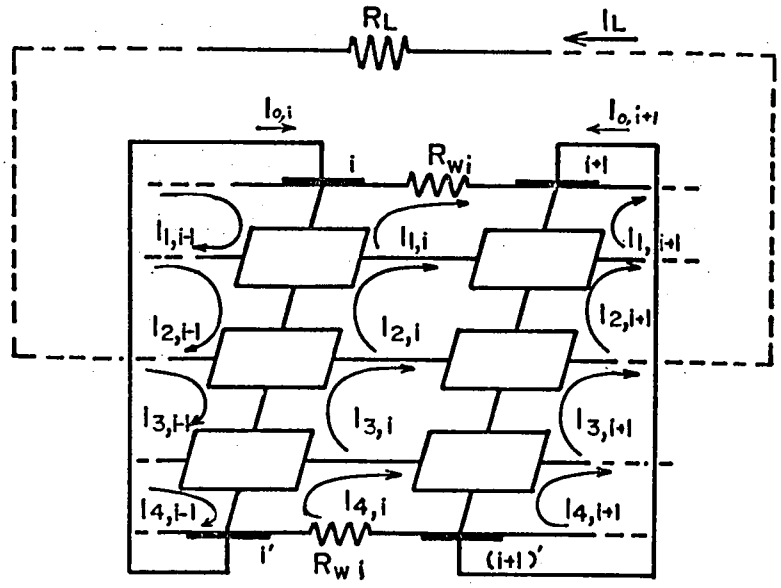

Fig. 2.7 Equivalent circuit of diagonal type generator.

of electrode pairs) is represented by an equivalent circuit as shown in Fig. 2.7, where R_{wi} is the leakage resistance of insulating spacer surface between the i or i'-th adjacent electrodes, $I_{1,i-1}$, $I_{1,i}$, etc. the loop currents, and I_L the load current.

In this connection the equivalent circuit in Fig. 2.7 can be easily applied to a multiple-load generator (see section 6.5).

(2) Network equations

For unknown currents $I_{0,i}$, $I_{0,i+1}$ and $I_{1,j-1}$ to $I_{4,j+1}$ in Fig. 2.7, we get a set of the following simultaneous equations

$$
\begin{aligned}
&- (R_{\eta 1,i} - R_{\xi\eta 1,i})\, I_{1,i-1} + (R_{wi} + R_{\eta,i} + R_{\eta 1,i+1} + R_{\xi 1,i} \\
&+ R_{\eta\xi 1,i} - R_{\xi\eta 1,i})\, I_{1,i} - (R_{\eta 1,i+1} + R_{\eta\xi 1,i+1})\, I_{1,i+1} \\
&- R_{\xi 1,i} + R_{\eta\xi 1,i})\, I_{2,i} + R_{\eta\xi 1,i+1}\, I_{2,i+1} - (R_{\eta 1,i} - R_{\xi\eta 1,i}) \\
&I_{0,i} + R_{\eta 1,i+1}\, I_{0,i+1} = e_{\eta 1,i+1} - e_{\eta 1,i} \,, \\
&- R_{\xi\eta 1,i}\, I_{1,i-1} - (R_{\xi 1,i} - R_{\xi\eta 1,i})\, I_{1,i} - (R_{\eta 2,i} - R_{\xi\eta 2,i}) \\
&I_{2,i-1} + (R_{\eta 2,i} + R_{\xi 1,i} + R_{\eta 2,i+1} + R_{\xi 2,i} + R_{\eta\xi 2,i} \\
&- R_{\xi\eta 2,i})\, I_{2,i} - (R_{\eta 2,i+1} + R_{\eta\xi 2,i+1})\, I_{2,i+1} - (R_{\xi 2,i} \\
&+ R_{\eta\xi 2,i})\, I_{3,i} + R_{\eta\xi 2,i+1}\, I_{3,i+1} - (R_{\eta 2,i} + R_{\xi\eta 1,i} \\
&- R_{\xi\eta 2,i})\, I_{0,i} + R_{\eta 2,i+1}\, I_{0,i+1} - (R_{\xi 2,i} + R_{\eta\xi 2,i} \\
&- R_{\eta\xi 2,i+1})\, I_L = e_{\eta 2,i+1} - e_{\eta 2,i} \,, \\
&- R_{\xi\eta 2,i}\, I_{2,i-1} - (R_{\xi 2,i} - R_{\xi\eta 2,i})\, I_{2,i} - (R_{\eta 3,i} - R_{\xi\eta 3,i}) \\
&I_{3,i-1} + (R_{\eta 3,i} + R_{\xi 2,i} + R_{\eta 3,i+1} + R_{\xi 3,i} + R_{\eta\xi 3,i}
\end{aligned}
$$

$$
\begin{aligned}
&- R_{\xi\eta 3,i})\ I_{3,i} - (R_{\xi 3,i} + R_{\eta\xi 3,i})\ I_{4,i} + R_{\eta\xi 3,i+1}\ I_{4,i+1} \\
&- (R_{\eta 3,i} + R_{\xi\eta 2,i} - R_{\xi\eta 3,i})\ I_{0,i} + R_{\eta 3,i+1}\ I_{0,i+1} \\
&+ R_{\xi 2,i}\ I_L - (R_{\eta 3,i+1} + R_{\eta\xi 3,i+1})\ I_{3,i+1} \\
&= e_{\eta 3,i+1} - e_{\eta 3,i}\ , \\
&- R_{\xi\eta 3,i}\ I_{3,i-1} - (R_{\xi 3,i} - R_{\xi\eta 3,i})\ I_{3,i} \\
&+ (R_{\xi 3,i} + R_{wi})\ I_{4,i} - R_{\xi\eta 3,i}\ I_{0,i} = 0\ , \\
&R_{\eta 1,i}\ I_{1,i-1} - (R_{\eta 1,i} + R_{\eta\xi 1,i})\ I_{1,i} + R_{\eta 2,i}\ I_{2,i-1} \\
&- (R_{\eta 2,i} + R_{\eta\xi 2,i} - R_{\eta\xi 1,i})\ I_{2,i} + R_{\eta 3,i}\ I_{3,i-1} \\
&- (R_{\eta 3,i} + R_{\eta\xi 3,i} - R_{\eta\xi 2,i})\ I_{3,i} + R_{\eta\xi 3,i}\ I_{4,i} \\
&+ R_{\eta\xi 2,i}\ I_L + \sum_{j=1}^{3} R_{j,i}\ I_{0,i} = \sum_{j=1}^{3} e_{j,i} \\
&\sum_{i=1}^{N} \{- R_{\xi\eta 2,i}\ I_{2,i-1} - (R_{\xi 2,i} - R_{\xi\eta 2,i})\ I_{2,i} + R_{\xi 2,i}\ I_{3,i} \\
&- R_{\xi\eta 2,i}\ I_{0,i} + R_{\xi 2,i}\ I_L \} + R_L\ I_L = 0\ ,
\end{aligned}
\qquad (2.28)
$$

where

$$
\begin{aligned}
R_{\xi j,i} &= s_i / (\sigma'_{j,i}\ d_i\ h_{j,i})\ , \\
R_{\xi\eta j,i} &= (\beta'_{j,i} + \cot\varphi_i) / (\sigma'_{j,i}\ d_i)\ , \\
R_{\eta\xi j,i} &= (\beta'_{j,i} - \cot\varphi_i) / (\sigma'_{j,i}\ d_i)\ , \\
R_{\xi j,i} &= h_{j,i} / (\sigma'_{j,i}\ d_i\ s_i \sin^2\varphi_i)\ ,
\end{aligned}
\qquad (2.28')
$$

$$e_{\eta j,i} = h_{j,i}\, u_{j,i}\, B \quad ,$$

$$j = 1,2,3 \qquad i = 1,2,\ldots,N \quad ,$$

by using Kirchhoff's law.

When it can be assumed that all electrical quantities vary periodically in the period of the electrode pitch in the direction of gas flow, as in the central region, the Eqs. (2.28) are much simplified, since the mesh currents, the resistances, and the electromotive forces in Eqs. (2.28) become as follows:

$$\left.\begin{aligned} & I_{j,i-1} = I_{j,i} = I_{j,i+1} \equiv I_j \quad , \\ & R_{\eta j,i} = R_{\eta j,i+1} \equiv R_{\eta j} \quad , \quad R_{\xi j,i} = R_{\xi j} \quad , \\ & R_{\eta\xi j,i} = R_{\eta\xi j} \quad , \quad R_{\xi\eta j,i} = R_{\xi\eta j} \quad , \\ & e_{\eta j,i} = e_{\eta j,i+1} \equiv e_{\eta j} \quad , \\ & R_{wi} \equiv R_w \quad , \quad j=1,2,3. \end{aligned}\right\} \qquad (2.29)$$

Furthermore, when the electrical quantities in the anode and cathode boundary layers are identical, we have

$$\left.\begin{aligned} & e_{\eta 1} = e_{\eta 3} \equiv e_{\eta b} \quad , \\ & R_{\xi 1} = R_{\xi 3} \equiv R_{\xi b} \quad , \quad R_{\eta 1} = R_{\eta 3} \equiv R_{\eta b} \quad , \\ & R_{\xi\eta 1} = R_{\xi\eta 3} \equiv R_{\xi\eta b} \quad , \quad R_{\eta\xi 1} = R_{\eta\xi 3} \equiv R_{\eta\xi b}. \end{aligned}\right\} \qquad (2.30)$$

If subscript 2 of $e_{\eta 2}$, $R_{\xi 2}$, $R_{\eta\xi 2}$, $R_{\xi\eta 2}$, and $R_{\eta 2}$ are replaced by 0 for convenience, using Eqs. (2.29) and (2.30), Eqs. (2.28) are reduced as follows:

$$(R_w + R_{\xi b})\, I_1 - R_{\xi b}\, I_2 + R_{\xi\eta b}\, I_0 = 0,$$

$$
\left.
\begin{aligned}
&- R_{\xi b}\, I_1 + (R_{\xi 0} + R_{\xi b})\, I_2 - R_{\xi 0}\, I_3 \\
&\qquad - (R_{\xi \eta b} - R_{\xi \eta 0})\, I_0 - R_{\xi 0}\, I_L = 0 , \\
&- R_{\xi 0}\, I_2 + (R_{\xi 0} + R_{\xi b}) I_3 - R_{\xi b}\, I_4 \\
&\qquad - (R_{\xi \eta 0} - R_{\xi \eta b})\, I_0 + R_{\xi 0}\, I_L = 0 , \\
&- R_{\xi b}\, I_3 + (R_w + R_{\xi b})\, I_4 - R_{\xi \eta b}\, I_0 = 0 , \\
&- R_{\eta \xi b}\, I_1 - (R_{\eta \xi 0} - R_{\eta \xi b})\, I_2 \\
&\qquad - (R_{\eta \xi b} - R_{\eta \xi 0})\, I_3 + R_{\eta \xi b}\, I_4 + (R_{\eta 0} \\
&\qquad + 2\, R_{\eta b})\, I_0 + R_{\eta \xi 0}\, I_L = e_{\eta 0} + 2\, e_{\eta b} , \\
&- R_{\xi 0}\, I_2 + R_{\xi 0}\, I_3 - R_{\xi \eta 0}\, I_0 + (R_{\xi 0} + R_L')\, I_L = 0.
\end{aligned}
\right\} \quad (2.31)
$$

where R_L' is the equivalent load resistance per one electrode pair in the central region of the duct. The currents, Joule heat, etc. in each space element can be obtained from solutions of these simultaneous equations.

2.3.2 Hall and Faraday type generators

The above-mentioned analysis by the equivalent circuit can be easily applied to the Hall and Faraday type MHD generators.

Since $\varphi = \pi/2$ in Figs. 2.1 and 2.2 in the Hall type generator, for it we obtain the same equivalent network as in Fig. 2.7. Accordingly for analyzing its performances, the same technique as the one analysing those of the diagonal type generator can be used.

For the Faraday type, similarly $\varphi = \pi/2$ in Figs. 2.1 and 2.2, and after elimination of the load resistance R_L and short-circuit conductor between anode and cathode in Figs. 2.1 and 2.7, separate load resistance is connected between the anode i and the cathode i'.

Further, leakage resistances of insulating side wall surfaces in the y direction must be connected in parallel to the load resistance. Network equations which are obtained from the equivalent network of the Faraday type generator are more or less different from those of the diagonal type one in the previous subsection, where the former equations are neglected here since the performance characteristics of the Faraday type generator are little discussed in this thesis.

2.4 Equivalent Circuit Considering Finite Electrode Segmentation[47]

In the MHD generator, the Hall field is short-circuited through the electrode because of its finite width. This is called the effect of finite electrode segmentation and causes deterioration of the gen-

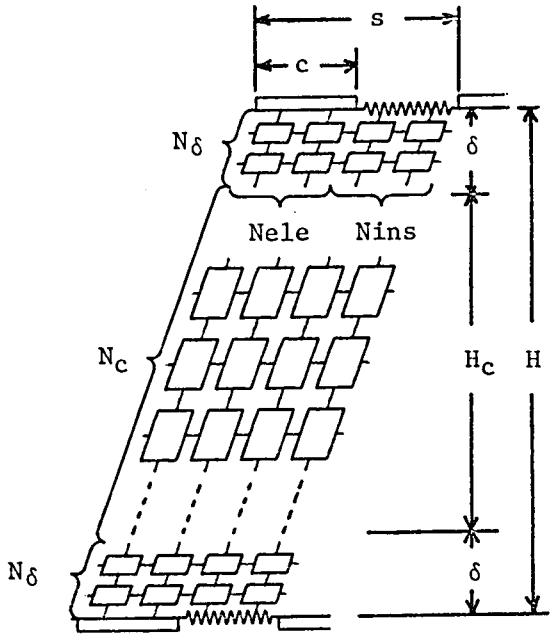

Fig. 2.8 Equivalent circuit considering finite electrode segmentation.

erator performance. To avoid such difficulty, the electrode width should be made infinitesimal, and furthermore, to short-circuit effectively the electric field in the direction of electrode pairs, the insulating width between adjacent electrodes should be done infinitesimal, too. This is called "ideal segmentation." In practice, however, it is impossible. Therefore in this section, there is proposed a composition of equivalent network considered the electrodes with finite width.

The finite segmentation effect mainly appears as current concentration near electrode end, which makes considerable difference in the current and potential distributions between upper and lower stream sides near the electrode and the insulating spacer. Accordingly, it is proposed that the number of space elements or their equivalent circuits per one electrode pitch s of the duct is increased, for instance, as shown in Fig. 2.8, in which electrode and insulating spacer regions are divided into N_{ele} and N_{ins}, respectively, by the planes parallel to the η-z plane. In the figure, δ and H_c are the boundary layer thickness and the core flow height, respectively, which are divided into N_δ and N_c, respectively, by the planes perpendicular to the y axis, and also c and H are the electrode width and the duct height, respectively. In this connection, in section 3.3, number of space elements will be discussed.

Dzung [32] has analysed the finite segmentation effect by a comformal mapping method, but his analysis is not applicable to the practical generator since the boundary layer, leakage current, etc. are not considered.

2.5 Formulation of Electrical Characteristics

2.5.1 Current density and Joule heat

By solving numerically the simultaneous Eqs. (2.28) or (2.31) under given numerical conditions, the values of I_ξ and I_η are obtain-

ed. Using the results and the following relation

$$\begin{pmatrix} J_x \\ J_y \end{pmatrix} = \frac{1}{d_e h_e s_e} \begin{pmatrix} s_e & h_e \cot\varphi \\ 0 & h_e \end{pmatrix} \begin{pmatrix} I_\xi \\ I_\eta \end{pmatrix} \tag{2.32}$$

which is derived from Eqs. (2.7) and (2.8), we can get the values of J_x and J_y to obtain the two-dimensional current pattern in a duct.

Next, Joule heat P_{eo} in a space element is given by

$$\begin{aligned} P_{eo} &= \int_{v_e} \mathbf{J} \cdot (\mathbf{E} + \mathbf{u} \times \mathbf{B}) \, dv = \{ J_x E_x + J_y (E_y - u B) \} s_e h_e d_e \\ &= (J_x^2 + J_y^2) s_e h_e d_e / \sigma' \\ &= R_\xi I_\xi^2 + R_\eta I_\eta^2 + (R_{\xi\eta} - R_{\eta\xi}) I_\xi I_\eta , \end{aligned} \tag{2.33}$$

where v_e is the volume of the space element.

2.5.2 Generated output and electrical efficiency

The input power to a space element is

$$P_e = \int_{v_e} \mathbf{J} \cdot (\mathbf{u} \times \mathbf{B}) \, dv = J_y u B s_e h_e d_e = e_\eta I_\eta . \tag{2.34}$$

Furthermore in Fig. 2.7, the power P_e which is supplied from gas plasma to the MHD generator is

$$P_e = \sum_{i=1}^{N} \sum_{j=1}^{3} P_{e\,j,i} , \tag{2.35}$$

where

$$\left.\begin{aligned} P_{e_{j,i}} &= u_{j,i} B h_{e_{j,i}} I_{\eta_{j,i}} , \\ I_{\eta_{j,i}} &= I_{j,i} - I_{j,i-1} - I_{0,i} , \end{aligned}\right|$$

$$I_{\xi j,i} = \begin{cases} I_{j+1,i} - I_{j,i} \text{ (boundary layer)}, \\ I_{j+1,i} - I_{j,i} + I_L \text{ (core flow)}, \end{cases} \qquad (2.36)$$

$$i = 1,2, \ldots,N, \quad j = 1,2,3.$$

The total output power P of the generator i.e. the total power P_L received by the load is

$$P = P_L = R_L I_L^2 \ . \qquad (2.37)$$

Accordingly the electrical efficiency η_e of the generator is given by

$$\eta_e = P / P_e = R_L I_L^2 \Big/ \sum_{i=1}^{N} \sum_{j=1}^{3} P_{e\,j,i} \ . \qquad (2.38)$$

In this connection, the output power density P_o is given by

$$P_o = R_L I_L^2 \Big/ \sum_{i=1}^{N} \sum_{j=1}^{3} \Delta v_{i,j} \ , \qquad (2.39)$$

where Δv is the volume of a space element.

2.6 Concluding Remarks

The main conclusions derived from the above investigation are as follows:

(1) From the generalized Ohm's law considering the Hall and the ion-slip effects, a new two-dimensional equivalent circuit of the diagonal type generator was derived. In the circuit, the boundary layer, the finite electrode segmentation effect, the leakage current on the insulating wall surface, etc. were considered.

(2) The above equivalent circuit can be easily applied to both the Hall and the Faraday type generators, by changing the diagonal angle,

connections of electrode and load resistances, etc.

(3) The expressions of the Joule heat, the output power, the electrical efficiency of the generator were introduced.

CHAPTER 3

ELECTRICAL CHARACTERISTICS OF CENTRAL REGION OF SINGLE-LOAD GENERATOR

3.1 Introduction

Roughly speaking, an MHD generator is consist of the central region and the end regions viz. the inlet and exit ones. In the central region, most electrical output is generated, and electrical quantities can be assumed to vary periodically in the period of one electrode pitch when the gas pressure, temperature, velocity, etc. little vary along the gas flow.

In this chapter, let us study numerically on the electrical characteristics of the central region of large scale single-load diagonal and Hall type generators by means of the ECM derived in chapter 2. First, it is verified that the relation between Hall voltage per one electrode pitch and load current calculated in much shorter cpu time by the ECM agrees well with the one by the FDM and the FEM. And the fewest number of space elements per one electrode pitch region to be used for obtaining reliable calculated results by the ECM is determined. Next, the influences of the leakage current, the ion-slip effect, the boundary layer, the finite electrode segmentation, the effect of the Hall parameter, the diagonal angle, etc. on the output power density and electrical efficiency of the generator are investigated in detail.

3.2 Numerical Conditions

3.2.1 When boundary layer is not considered

The conditions assumed in the numerical calculation are listed in Table 3.1, where they are the values almost corresponding to a practical MHD generator. In the table, D is the duct width, μ electron mobility, and R_x the plasma resistance per one electrode pitch along to the x axis, which is given by

$$R_x = s / (\sigma D H) \cdot [\mathcal{V}] \tag{3.1}$$

When boundary layer is not considered, we adopt

$$\left.\begin{aligned} &\sigma = 10\ \mathcal{V}/[\mathrm{m}], \\ &\beta = \mu B = 0.5 \text{ to } 10, \\ &\beta_i / \beta = 0 \text{ to } 10^{-2}, \end{aligned}\right\} \tag{3.2}$$

which are the values assumed in usual MHD generator driven by combustion gases.

Table 3.1 Numerical conditions used in calculation.

H (m)	1	φ (°)	25 to 90
D (m)	1	B (T)	6
s (m)	0.05 to 0.1	μ (T^{-1})	1/12 to 5/3
c/s	0.5 to 0.8	u (m/s)	800, 1000
δ (m)	0.025 to 0.1	R_w/R_x	10^2 to ∞

3.2.2 When boundary layer is considered

Since temperature and velocity vary abruptly in boundary layer, influence of temperature on σ and β should be taken into consideration. Now, in section 3.3 and chapters 5 and 6, the dependences of σ and β on the gas temperature T, the static gas pressure p, and the applied magnetic flux density B are determined as follows:

$$\left.\begin{aligned} \sigma &= 3.21\times10^{4}\, p^{-0.51}\, T^{1.06} \exp(-2.52\times10^{4}/T)\ [\mho/m], \\ \beta &= 40.2\, p^{-0.99}\, T^{0.97}\, B. \end{aligned}\right\} \quad (3.3)$$

where p is in atm. and T in K. These were derived from the numerical data [48] of a combustion product of heavy-oil fuel and oxygen of a stoichiometric factor 1.1, where KOH and K_2SO_4 are seeded so that the potassium atom is contained in a ratio 1 weight % to the combustion gas. But in section 3.4, in which influences of β and thickness of boundary layer on the output power are investigated, for simplicity, the follwoing expressions

$$\left.\begin{aligned} \sigma_b / \sigma &= (T_b / T)^{10}, \\ \beta_b / \beta &= (T_b / T)^{0.97}, \end{aligned}\right\} \quad (3.4)$$

are used for σ and β [25, 49], where sufix b denotes the quantity in the boundary layer.

Next, for the thickness δ of the velocity boundary layer of turbulent flow on a smooth flat plate, Schlichting obtained the following expression [50]

$$\left.\begin{aligned} \delta &= 0.37\ x\ R_e^{-0.2}\ [\mho/m], \\ \text{where} \quad R_e &= \rho\, u\, x / \mu_\nu \quad . \end{aligned}\right\} \quad (3.5)$$

In these equations, x is the distance from the plate end in the gas flow direction, R_e the Reynolds number, and ρ and μ_ν

the mass density and viscosity of gas, respectively, where for μ_ν Sutherland has derived the following expression [50]

$$\mu_\nu = 0.249\times10^{-6}\ T^{0.75}\ \ [\mathrm{kg/m/sec}]. \tag{3.6}$$

Using Eqs. (3.5) and (3.6), we obtain, for example, δ=0.04m at x=5m along the wall of a duct with a working gas of ρ=0.27kg/m , T=2500K and u=1000m/s. We will use δ=0.025 to 0.1m, as shown in Table 3.1, to examine the effect of the boundary layer thickness.

When the pressure gradient in the duct can be ignored, the 1/7th power law for the velocity holds, and the gas velocity distribution in the boundary layer is expressed by

$$u_b / u = (y / \delta)^{1/7} . \tag{3.7}$$

When the duct wall temperature T_w is lower than core flow temperature T, there exist not only velocity boundary layer but also thermal one. When Prandtl number $Pr \fallingdotseq 1$ as assumed usually in the analysis of MHD generator, the thermal boundary layer thickness is assumed to be equal to the velocity boundary layer one δ. Furthermore, when it is assumed that the distribution of temperature in boundary layer is analogous to that of velocity, we have the following approximate relation [51]

$$\frac{T_b - T_w}{T - T_w} = \frac{u_b}{u} . \tag{3.8}$$

Besides, in numerical investigation, we assume

$$\left.\begin{aligned} &p = 2\ \mathrm{atm.}\ ,\quad T = 2500\ \mathrm{K},\\ &T_w = 1500,\ 2500\ \mathrm{K}. \end{aligned}\right\} \tag{3.9}$$

3.3 Number of Space Elements and Comparison among Calculation Results by ECM, FDM, and FEM

As is well-known, conventionally the two-dimensional distributions of current and potential in the generator duct can be obtained by solving numerically the difference analogue of the partial differential equation for the stream function Ψ or the potential one Φ, which is derived from the Maxwell equations and the generalized Ohm's law, under some appropriate boundary and subsidiary conditions [52]. The above numerical method is called the finite difference method (FDM), and the results by it are thought to be very accurate when the duct is divided into many fine meshes. Furthermore, recently, the finite element method (FEM) has been applied to numerical analysis of performances of the MHD generator [35]. The numerical solutions by the FEM may converge rapidly to accurate ones with coarser meshes than the FDM, and especially it is effective to evaluate nonuniform field as in the boundary layer.

In this section, let us examine how many space elements should be used for one pitch in the central part of the duct to obtain reliable numerical calculation results by the equivalent circuit method (ECM). To achieve it, the results by the ECM are compared with those by the FDM and the FEM. Numbers of division per one electrode pitch of the duct in those calculation methods are listed in Table 3.2. The symbols N_{ele}, N_{ins}, etc. were already defined in section 2.4.

Table 3.2 Number of division.

		Nele	Nins	N_δ	N_c
ECM	case 1	2	1	1	3
	case 2	3	2	2	5
FEM		15	15	5	10
FDM	Tw=2500K	20	20	2	36
	Tw=1500K	20	20	10	380

Figure 3.1 shows relation between the load current I_L and the Hall voltage V_x per one electrode pitch i.e. V_x-I_L characteristics, which are obtained by the above three methods, where s=0.1m, c/s=0.5, and 0.8, φ =45°, δ = 0.05m, p = 2atm, u = 800m/s, T = 2500K, and T_w = 2500 and 1500K. The figure shows that the $V_x - I_L$ characteristics calculated by the ECM(case 2) agree well with those by FEM and FDM. In addition, cpu time needed for the ECM(case 2) is about 1/50 of that for the others.

In Fig. 3.2, there are compared the $V_x - I_L$ characteristics obtained by the ECM(case 1) and the ECM(case 2). It is seen that the calculation results by case 1 agree sufficiently with the ones by case 2. In other words, in numerical calculation by the ECM, using relatively few space elements, we can get relible results.

In this connection, numerical calculations in subsections 3.4.1 to 3.4.3 are performed by using the equivalent circuit in Fig. 2.7,

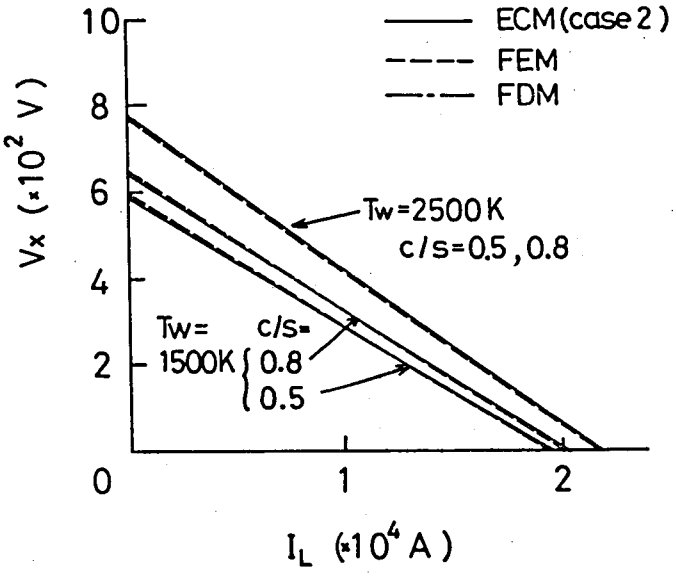

Fig. 3.1 V_x-I_L characteristics calculated by ECM(case 2), FEM, and FDM (s =0.1m, φ= 45°, δ = 0.05m, p = 2atm, u=800m/s, T=2500K).

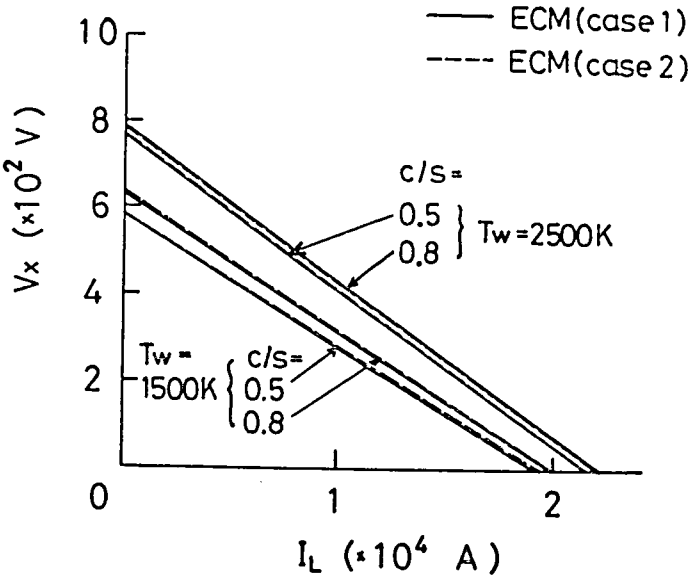

Fig. 3.2 Comparison of V_x-I_L characteristics by ECM(case 1) and ECM(case 2) ($s = 0.1m, \varphi = 45°$, δ=0.05m, p=2atm, u=800m/s, T=2500K).

and those in subsections 3.4.4 and 3.4.5 are carried out by the ECM (case 1) in Table 3.2.

3.4 Electrical Characteristics [53, 54]

3.4.1 Ideal generator

An ideal generator is defined as the generator in which the gas velocity is constant, the ion slip zero, the insulating wall resistance infinite, the electrode segmentation infinitely fine, and any boundary layer does not rise. The electrical characteristics of the generator can be obtained by calculating the values of the equivalent circuit elements by using Eqs. (2.10) and Table 3.1, substituting the results into Eqs. (2.31), and numerically solving the finally obtained simultaneous equations.

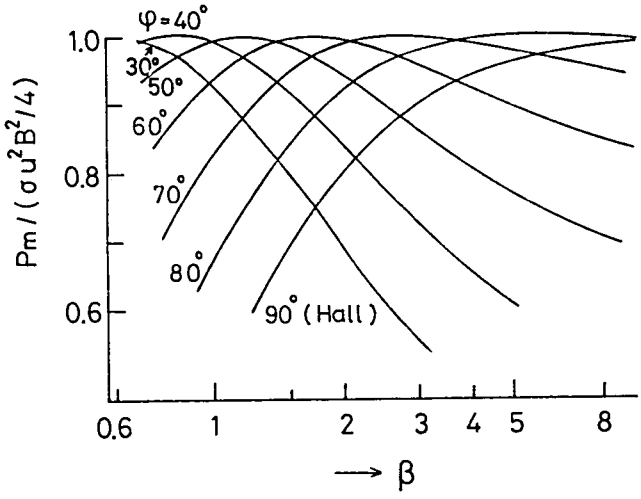

Fig. 3.3 Maximum output power density in ideal generator (u = 1000m/s).

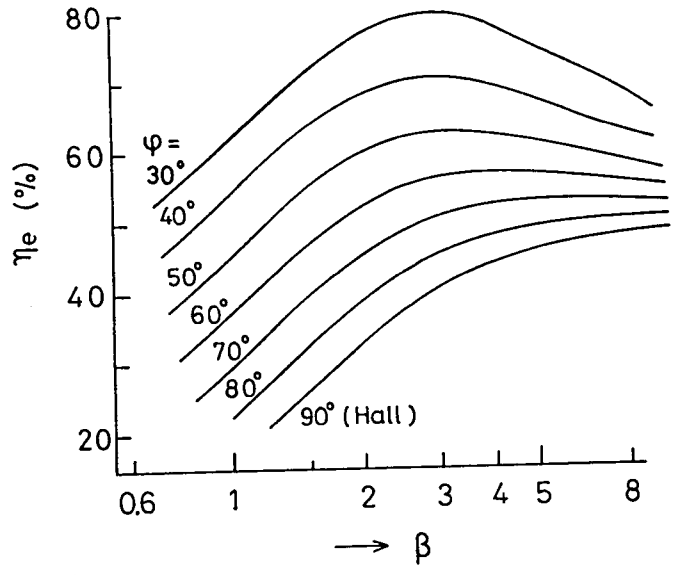

Fig. 3.4 Electrical efficiency for maximum output power (u = 1000m/s).

Figure 3.3 shows the relation between β and the maximum output power density $P_o = P_m$ normalized by the one $\sigma u^2 B^2/4$ of the ideal Faraday generator, where $u = 1000$m/s. This result coincides with the one obtained by the socalled quasi one-dimensional analysis. In this connection, there exists the diagonal angle $\varphi = \varphi_m$ which maximizes P_m for any β, and it is given by

$$\varphi_m = \tan^{-1} \beta. \tag{3.9}$$

Figure 3.4 shows the efficiency η_e for $P = P_m$ evaluated by Eq. (2.38). Besides, it was known that for small β the load resistance which gives the maximum efficiency η_{em} agrees with the load resistance which maximizes P_m, but for large β the magnitudes of both resistances fairly differ.

3.4.2 Influence of leakage current

To examine influence of leakge current on the generator characteristics, we assume that R_w is finite for the ideal generator in the

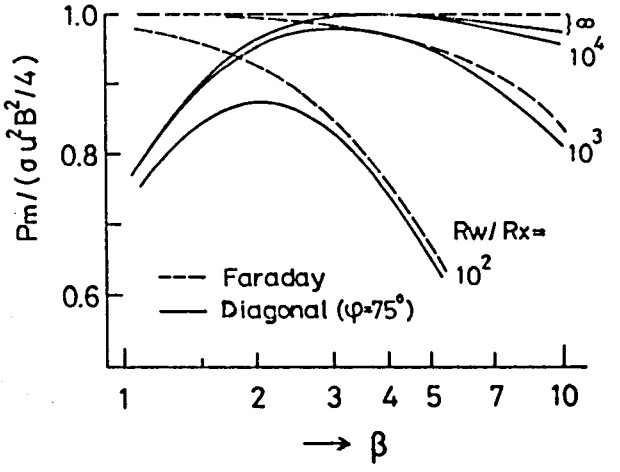

Fig. 3.5 Influence of leakage resistance of insulating spacer surface ($u = 1000$m/s).

previous subsection. Figure 3.5 shows the relation between β and P_m, where $\varphi = 75°$ is chosen since Pm is maximized for 70 to 75° with $\beta \doteqdot 3$ in Fig. 3.3. As shown in Fig. 3.5, as a parameter R_w/R_x is used instead of Rw. From the figure, it is seen that the influence of the leakage current on Pm appears when $R_w/R_x < 10^3$ for $\beta > 3$, and $R_w/R_x < 10^4$ for $\beta > 10$. In this connection the Faraday type generator also exhibits large influence of the leakage current as β is large.

3.4.3 Influence of ion slip

To study the influence of ion slip on the generator characteristics, we assume $\beta_i \neq 0$ for the ideal generator in subsection 3.4.1. Figure 3.6 shows the influence of the ion slip on Pm when $\varphi = 70°$. When $\beta_i/\beta > 10^{-3}$, large one is seen in high β region. The characteristics of the Hall type generator are also shown for comparison. When $\beta_i/\beta = 0$, the Hall type is superior to the diagonal one for $\beta > 6$. However, when $\beta_i/\beta = 10^{-2}$, the former is inferior to the latter even in high β region.

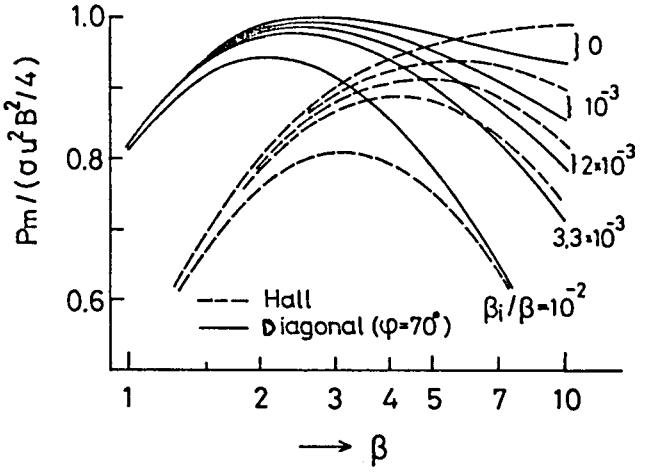

Fig. 3.6 Influence of ion slip (u = 1000m/s).

3.4.4 Influence of boundary layer

We investigate the influence of boundary layer on the generator characteristics with the assumption that the thickness of the thermal boundary layer is equal to that of the velocity one as described in subsection 3.2.2.

In the boundary layer, u, σ, and β vary steeply in the y direction. Even in such case, we can evaluate very accurately the electrical characteristics of the generator as in section 3.3 by using the equivalent circuit derived in subsection 2.2.1.

Figure 3.7 shows the relation between β and Pm when $\sigma = 10$℧/m, T = 2500K, and Tw = 1500K. As seen from the figure, the influence of the boundary layer on P_m increases with β and δ.

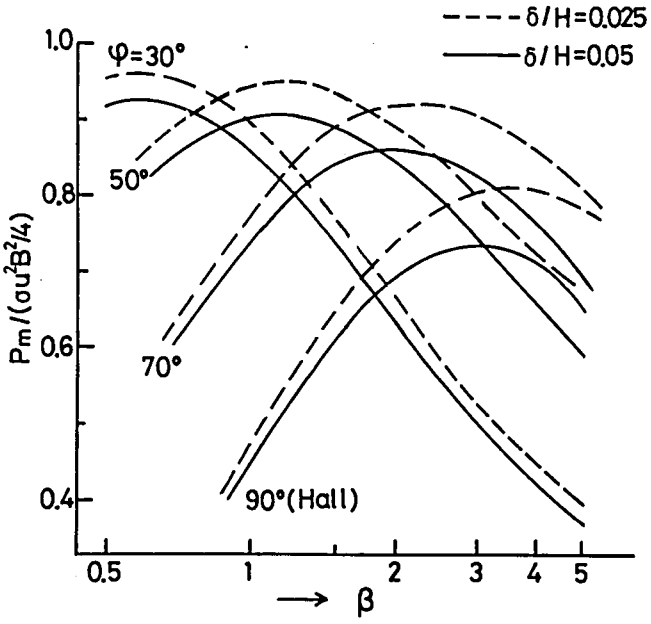

Fig. 3.7 Influence of boundary layer (u = 800m/s, T = 2500K, Tw = 1500K).

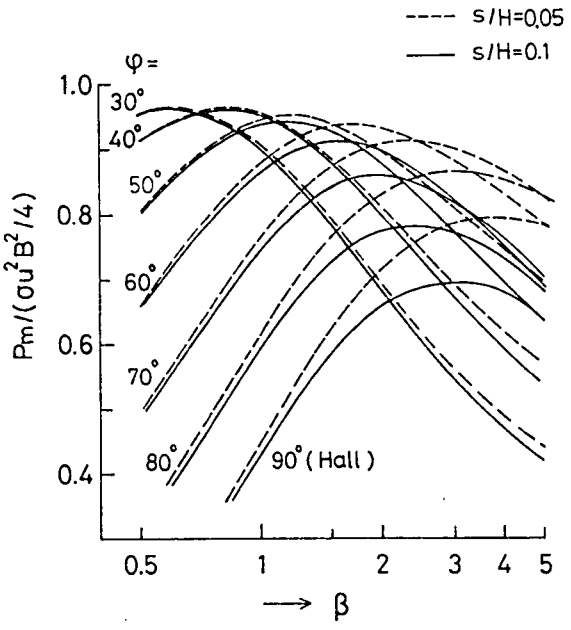

Fig. 3.8 Influence of finite electrode segmentation (s = 0.05m, c/s = 0.5, δ = 0.05m, u = 1000m/s, T = T_W = 2500k).

3.4.5 Influence of finite electrode segmentation

Figure 3.8 shows the relation of Pm vs. β for s/H = 0.05 and 0.1, which is calculated by the ECM(case 1) in Table 3.2, where s = 0.05m, c/s = 0.5, δ = 0.05m, u = 1000m/s, and T = Tw = 2500K. It is seen that as s/H, φ increase, the influence of finite segmentation worsens the generator characteristics.

3.4.6 When above all influences are considered

In Fig. 3.9, there are plotted the results obtained by the equivalent circuit with consideration of leakage current, ion slip, boundary layer and finite segmentation, where s = 0.05m, c/s = 0.5, δ = 0.05m and 0.025m, u = 1000m/s, Rw/Rx = 10^5, T = 2500K, Tw = 1500K, and $\beta_i/\beta = 10^{-3}$.

It is seen that the generator output power can be maximized by using appropriate values of β and φ, which are fairly different from those of the ideal generator. When β is high, for example, $\beta > 5$, the generator characteristics very worsen. The characteristics of the Hall type generator are far inferior to those of the diagonal type one.

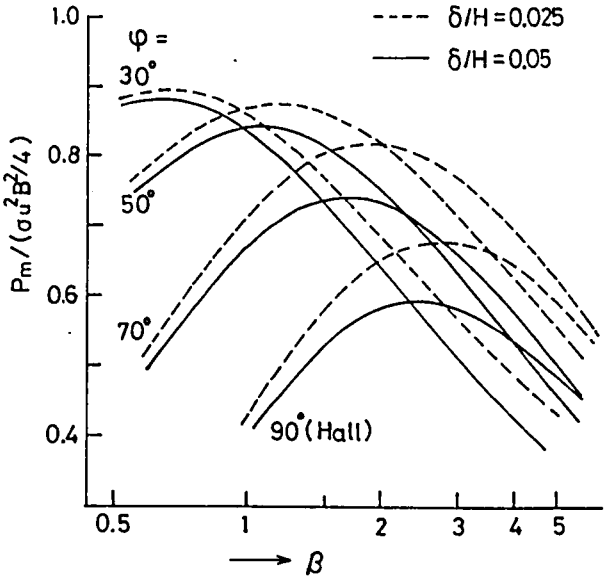

Fig. 3.9 Generation characteristics considering leakage resistance, ion slip, boundary layer, and finite electrode segmentation effect ($s = 0.05$m, $c/s = 0.5$, $u = 1000$m/s, $Rw/Rx = 10^5$, $T = 2500$K, $Tw = 1500$K, $\beta_i/\beta = 10^{-3}$).

Next, Figures 3.10(a), (b), (c), and (d) show the relations between the electrical efficiency η_e and the output power density P_o normalized by P_{Fm} of both Faraday and diagonal type generators when $\beta = 1$, 2, 3, and 4, respectively, where P_{Fm} is the maximum output power density of the Faraday one obtained under the given numerical

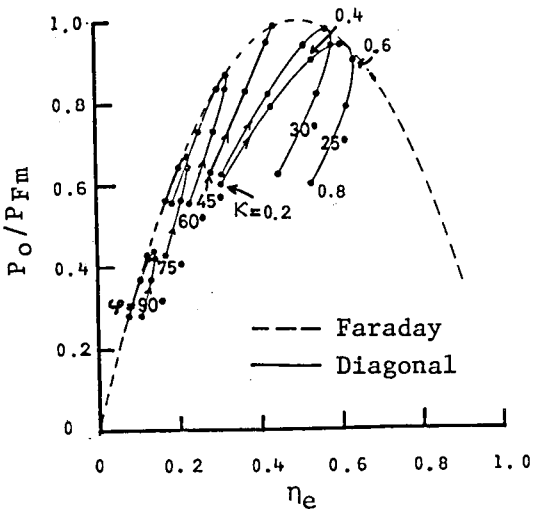

(a) When $\beta = 1$.

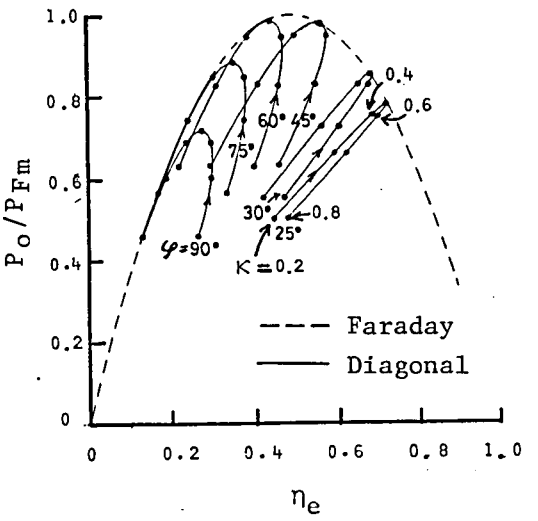

(b) When $\beta = 2$.

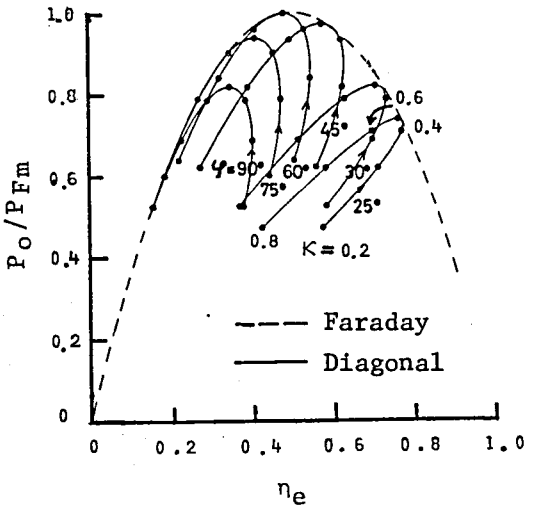

(c) When $\beta = 3$.

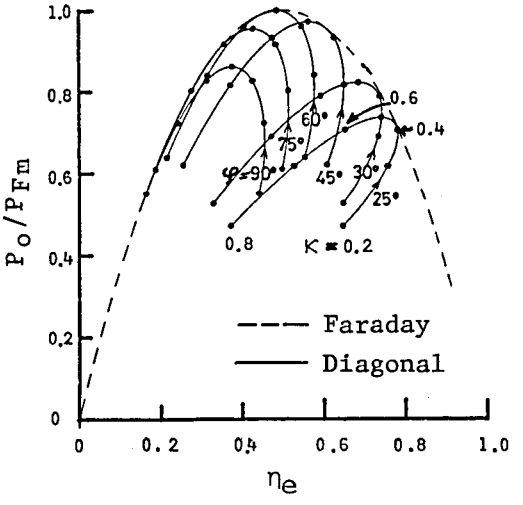

(d) When $\beta = 4$.

Fig. 3.10 Relations between η_e and P_o/P_{Fm} ($s = 0.1m$, $c/s = 0.6$, $\delta = 0.05m$, $u = 800m/s$, $Rw = 10^4\Omega$, $T = 2500K$, $Tw = 1500K$).

conditions, in which $s = 0.1m$, $c/s = 0.6$, $\delta = 0.05m$, $u = 800m/s$, $R_w = 10^4\Omega$, $T = 2500K$, $T_w = 1500K$, $\beta_i = 0$, and $p = 5.34$, 2.65, 1.76, and 1.32 atm are given so that we obtain $\beta = 1$, 2, 3, and 4, respectively. As shown in the figures, we use two parameters of the diagonal angle φ and the load factor κ defined by

$$\kappa = V_x \,/\, V_{xo} \quad , \tag{3.10}$$

where

$$V_{xo} = V_x \,|\, _{I_L = 0} \quad . \tag{3.11}$$

From the figures, it is seen that one point on $P_o/P_{Fm} - \eta_e$ curve of the diagonal type generator for some suitable values of φ and κ about any β approximately agrees with some point on the curve of the Faraday one. In other words, we can expect that the diagonal one are able to have the high output power and electrical efficiency compared favorably with those of the Faraday one.

3.5 Concluding Remarks

The main conclusions derived from the above numerical analysis are as follows:

(1) It was confirmed that $V_x - I_L$ characteristics in the central region of the diagonal type generator calculated in much shorter cpu time by the ECM agree well with those by the FDM and FEM. And the fewest number of space elements to be used for obtaining sufficiently accurate calculated results by the ECM was determined.

(2) The influences of the leakage current on the insulating wall surfaces, the ion-slip effect, the boundary layer, the finite electrode segmentation effect, the Hall parameter, the diagonal angle, etc. on the electrical characteristics of the large scale generators

were investigated in detail. When $R_w/R_x < 10^3$ and $\beta_i/\beta > 10^{-3}$, the characteristics worsen in high β region. The characteristics of the Hall generator is much worse than those of diagonal type.

(3) In the diagonal type generator, the high output power and electrical efficiency compared favorably with the Faraday one can be obtained under the suitable diagonal angle and load factor for any Hall parameter.

CHAPTER 4

ELECTRICAL CHARACTERISTICS OF END REGIONS OF SINGLE-LOAD GENERATOR

4.1 Introduction

In the end regions of a diagonal type generator duct, the output electrodes are located, the distributions of the applied magnetic flux density, the diagonal angle, etc. are usually nonuniform, and the nozzle and the diffuser are connected to the generator inlet and exit, respectively. Consequently the numerical results for the central region in the preceding chapter are not applicable to the end regions. In the end regions, it is more important to extract the load current with relaxing current concentration at the output electrode ends than to heighten the generated output, the electrical efficiency, etc. as in the central region. Ishikawa, et al. [55] have already evaluated the end effects of a middle scale diagonal type generator with nonequilibrium ionization plasma by the FDM.

From the above points of view, this chapter is offered to analyse in detail the electrical characteristics of the end regions of a large scale single-load diagonal type generator by applying the ECM derived in chapter 2 to the end regions [56-58]. First, states of electrode arrangements and applied magnetic flux distribution in the end regions are assumed. And there are introduced the equivalent network of the duct end regions with nozzle or diffuser by using the equivalent circuit in chapter 2, and the ECM and the FDM for evaluating the elec-

trical characteristics. Next, it is ascertained that current and potential distributions obtained by the ECM agree well with the ones by the FDM. Further, there are studied on the lengthes of the nozzle and the diffuser to be considered when the current and potential distributions in the duct end are evaluated. Finally, there are discussed influences of the applied magnetic flux distribution, the load current, number of the output electrodes, etc. on current concentration at the output electrode ends.

In addition, the current and potential distributions in the exit region become symmetric to the one in the inlet region when the gradient of the partial electron pressure can be neglected as in our case. Therefore, numerical calculation in this chapter is carried out only with respect to the inlet region of the duct.

4.2 Arrangement of Electrodes and Distribution of Applied Magnetic Flux

Figure 4.1 shows a schematic diagram of the region from the inlet to the central part of the diagonal type MHD generator duct, which is adopted as the research object in this chapter. In the figure, it is assumed that the diagonal angle φ is given by

$$\varphi = \left\{ \begin{array}{ll} \cot^{-1}\left(x \cot \varphi_0 / x_{t1} \right) & \text{for } 0 \leqq x \leqq x_{t1}, \\ \varphi_0 & \text{for } x_{t1} < x < x_{t2}, \\ \cot^{-1}\left[\cot \varphi_0 \left\{ 1 - \left(x - x_{t2} \right) / \left(L - x_{t2} \right) \right\} \right] & \text{for } x_{t2} \leqq x \leqq L, \end{array} \right\} \quad (4.1)$$

in which L is the duct length, x_{t1} the x coordinate where φ reaches a constant angle φ_0 in the inlet region and x_{t2} the same one where φ

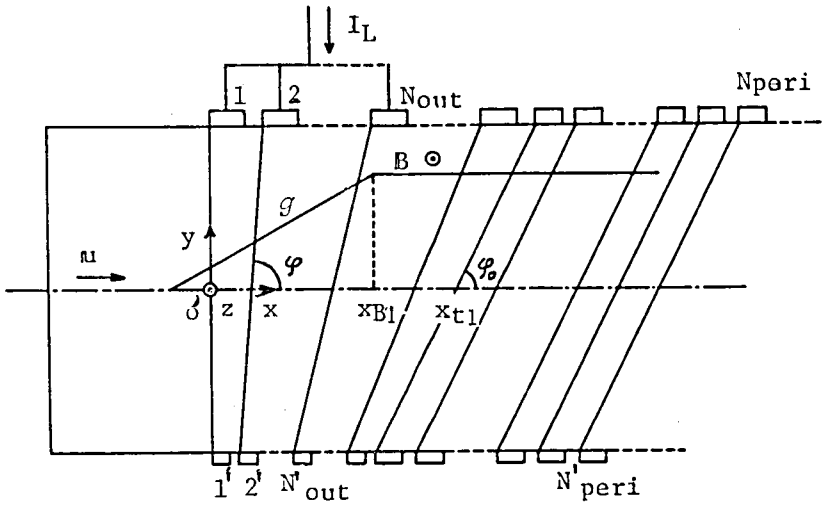

Fig. 4.1 Schematic diagram of duct inlet region of diagonal type generator.

begins to increase from φ_0 in the exit region. Nout (anode side) = N'_{out} (cathode side) is the number of the output electrodes which are short-circuited each other, and Nperi = N'_{peri} the number of the electrodes which the electrical quantities can be assumed to vary periodically in the period of one electrode pitch along the gas flow after. N_{out} must be properly selected in accordance with the magnitude of the load current, and the values of x_{t1} and x_{t2} are decided almost by the value of φ_0 . Besides, as Nout, x_{t1} or x_{B1} becomes large, or as φ_0 becomes small, Nperi must be taken large, where x_{B1} is defined a little later.

To study the influence of the attenuation of the applied magnetic flux density $\mathbb{B}$ = (0, 0, B) on the current concentration at the output electrode ends, as seen from Fig. 4.1, it is assumed that B is a constant value B_0 in the central region and it decreases with a constant gradient of $g = dB/dx$ from $x = x_{B1}$ and x_{B2} in the inlet and exit, respectively. Then B is expressed by

$$B = \begin{cases} 0 \quad \text{for } x \leqq x_{B1} - B_0/g, \text{ and } x \geqq B_0/g + x_{B2} , \\ B_0 + g(x - x_{B1}) \quad \text{for } x_{B1} - B_0/g < x < x_{B1} , \\ B_0 \quad \text{for } x_{B1} \leqq x \leqq x_{B2} , \\ B_0 - g(x - x_{B2}) \quad \text{for } x_{B2} < x < x_{B2} + B_0/g . \end{cases} \tag{4.2}$$

In addition, the secondary magnetic flux density induced by the generator current is assumed to be negligible compared with B, because the magnetic Reynolds number of the gas is much smaller than unity under the operating conditions. The electric conductivity σ and velocity $\mathbf{u} = (u, 0, 0)$ of the gas are assumed to be constant.

4.3 Equivalent Network of Duct End Regions

4.3.1 Equivalent network

In an actual MHD generator, because of spatial nonuniformity of

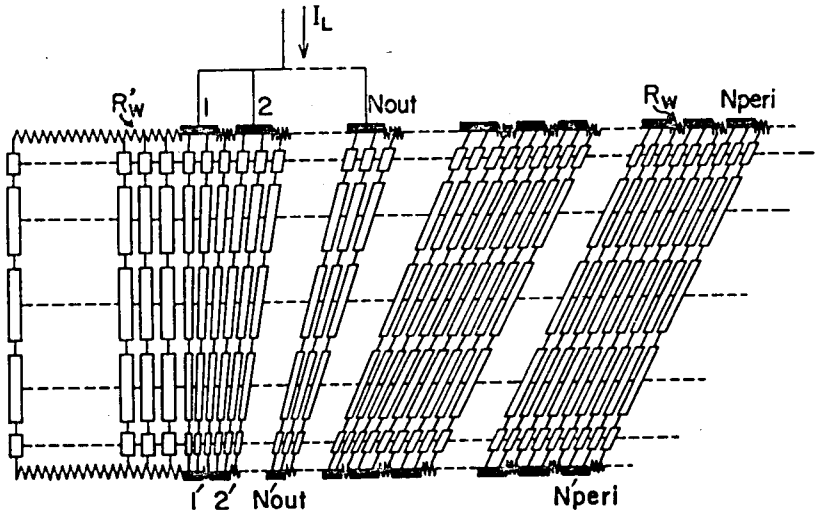

Fig. 4.2 Illustration of duct inlet region by using equivalent network.

the physical quantities in the duct space, each space element has a fairly small volume as compared with the whole duct size as shown in the preceding chapter. Accordingly, replacing each space element by the equivalent circuit in Fig. 2.3, the duct inlet region in Fig. 4.1 is expressed, for example, by an equivalent network as shown in Fig. 4.2. As seen in the figure, the duct space between the anodes and cathodes is divided horizontally into five layers, where both the uppermost and the lowest layers are assumed much more thinner than the other three layers. The thicknesses of the former two layers are taken as being equal to each other, because it was ascertained that by such a technique the accuracy of the numerical calculation by the equivalent circuit becomes good: see the ECM (case 1) in section 3.3. Also the domain of one electrode pitch along the gas flow is divided vertically or diagonally into three columns of two with the electrode and one with the insulating spacer. Moreover, it is assumed that the sizes of the space elements in the nozzle region are the same as the ones in the electrode region.

Also in Fig. 4.2, Rw is the equivalent leakage resistance along the insulator surface between the adjacent electrodes, and Rw' is the equivalent leakage resistance along the nozzle inner surface. In the numerical calculation, the values of Rw and Rw' are chosen as $10^4\Omega$ sufficiently large so as not to affect the calculation results.

4.3.2 ECM and FDM

As already described in subsection 2.2.1, the values of the resistances and electromotive forces in the equivalent circuit of each space element in Fig. 4.2 can be numerically determined when the dimension of each space element and σ, β and β_i in the element are given. Then, many simultaneous circuit equations for the unknown currents flowing in the resistances in the equivalent network shown in Fig. 4.2 are obtained by Kirchhoff's law. When the simultaneous equa-

tions are numerically solved, the values of the currents and consequently their densities in the space elements are obtained. Then, the potential of each electrode can be numerically calculated.

On the other hand, as described in section 3.3, conventionally the two-dimensional distributions of the current or potential in the generator duct have been obtained by the FDM. The numerical calculation results by the FDM are thought to be highly accurate when the duct space is divided into many fine meshes. Therefore, as well as in the central region of the duct in chapter 3, by comparing the calculation results of the current and potential distributions in the duct ends by the ECM with the similar ones by the FDM under the same numerical conditions, the reliability of the ECM should be investigated.

Hitherto, by the FDM, the differential equation for only the stream function Ψ or the potential one Φ has been first solved numerically, and then the other electrical quantities were determined by using the value of Ψ or Φ. On the other hand, here it is tried to solve the equation for Φ in the duct region with electrodes and the equation for Ψ in the nozzle region without electrodes. Through practical calculation under numerical conditions used in this chapter, it was ascertained that the latter calculation method is considerably superior to the former conventional one in the convergence speed.

4.4 Numerical Conditions

The conditions assumed for numerical calculation are listed in Table 4.1. In the table, $N'_{peri} = 17$ and 32 are the number of the cathodes used in the analysis by the FDM, and more cathodes are used in the analysis by the ECM.

Table 4.1 Numerical conditions used in calculation.

φ_0 (°)	45		68.2
N_{out}	1 to 10		6
N'_{peri}	32		17
x_{t1} (m)	1.5		0.45
μ (T^{-1})	1/6	2/3	1/6
I_L ($\times 10^4$A)	6	0.1 to 3	4
x_{B1} (m)	0, 1, 2, 3		0
g (T/m)	0, 1, 2.5, 5		0
H (m)	1.5		
s (m)	0.15		
c/s	0.65		
σ (℧/m)	10		
u (m/s)	800		
B_0 (T)	6		

4.5 Comparison between Calculation Results by ECM and FDM

Figures 4.3(a) and (b) show the potential and current distributions in the generator end region, respectively, which are calculated by the FDM with the conditions of $\varphi_0 = 45°$, $N_{out} = 4$, $\mu = 2/3$, $I_L = 2\times10^4$A, $x_{B1} = 1.5$m, and $g = 2.5$T/m, where the contour intervals are 200V and 500A/m, respectively.

Figure 4.4 shows the distribution of the current density vectors in the space elements in the end domain which are obtained by the ECM under the same numerical conditions as in Figs. 4.3. In this figure, the maximum current density of 3.9×10^4A/m^2 appears at the front end of the upper first output electrode 1. From Figs. 4.3(b) and 4.4, it

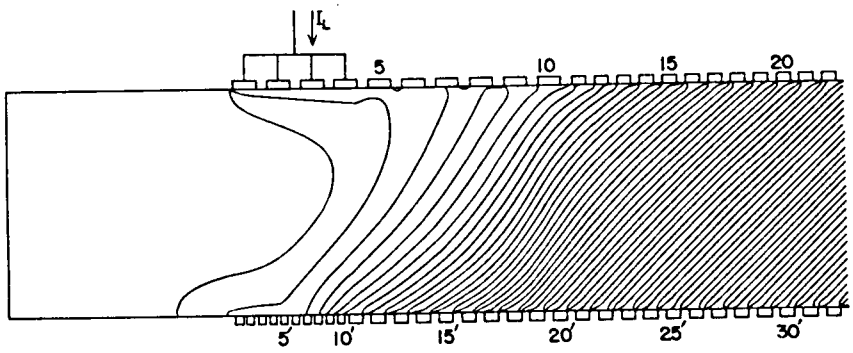

(a) Potential distribution (contour interval: 200V).

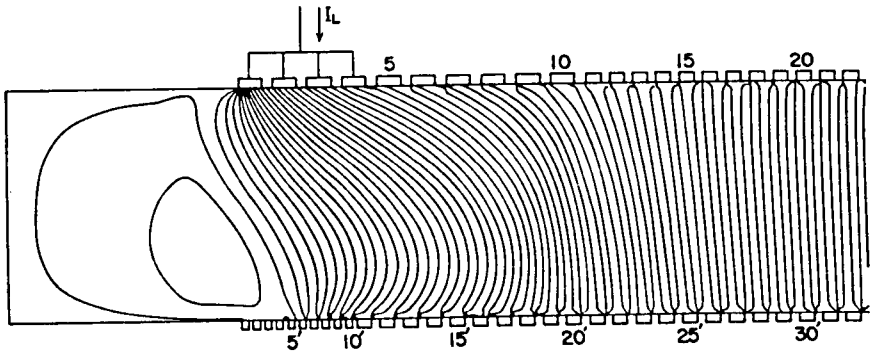

(b) Current distribution (contour interval: 500A/m).

Fig. 4.3 Potential and current distributions calculated by FDM (φ_0=45°, N_{out}=4, μ=2/3, I_L=2×10^{4}A, x_{BI}=2m, g=2.5T/m).

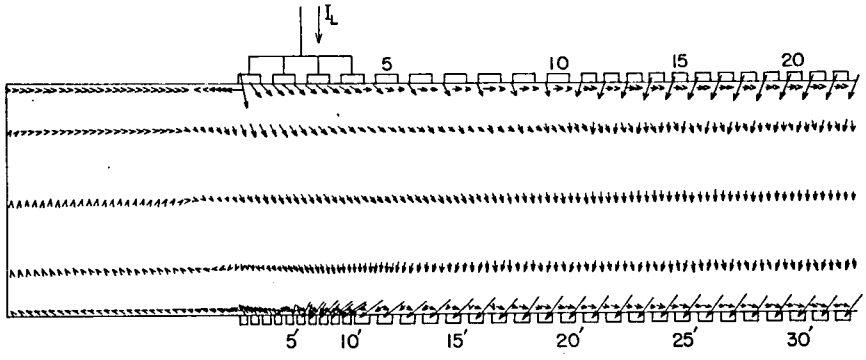

Fig. 4.4 Current pattern calculated by ECM for the same conditions as in Figs. 4.3 (maximum current density: 3.9×10^{4}A/m^2).

will be seen that the current pattern in the latter is quite analogous to the one in the former.

Next, Figure 4.5 represents the potential difference V_n between the output electrodes and the n-th electrode ($N_{out} < n \leq N_{peri}$), which are calculated by the FDM and the ECM with the same numerical conditions as in Figs. 4.3. It is seen that the calculation result of V_n by the ECM sufficiently agrees with the one by the FDM.

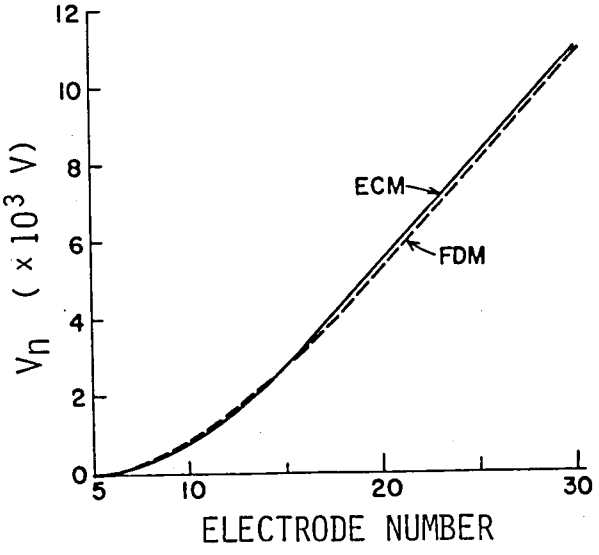

Fig. 4.5 Comparison of V_n calculated by ECM and FDM.

Next, in Figs. 4.6(a) and (b), there are plotted the potential and current distributions, respectively, in the end area, which are obtained by the FDM for $\varphi_0 = 68.2°$, $\mu = 1/6$, $I_L = 4\times10^4$A, and $g = 0$, where the contour intervals are 200V and 1500A/m, respectively. On the other hand, Fig. 4.7 shows the current pattern calculated by the ECM under the same conditions as in Figs. 4.6. It will be recognized that the current pattern in Fig. 4.7 is very similar to the one in Fig. 4.6(b). In addition, the maximum current density of 24.5×10^4A/m^2 is found again at the upstream end of the electrode 1.

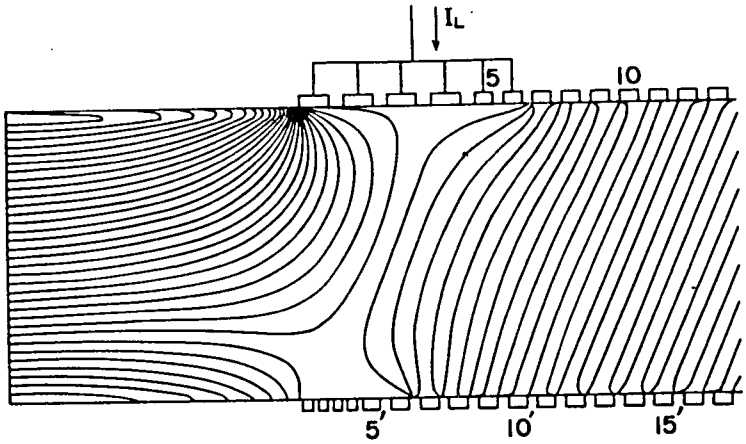

(a) Potential distribution (contour interval: 200V).

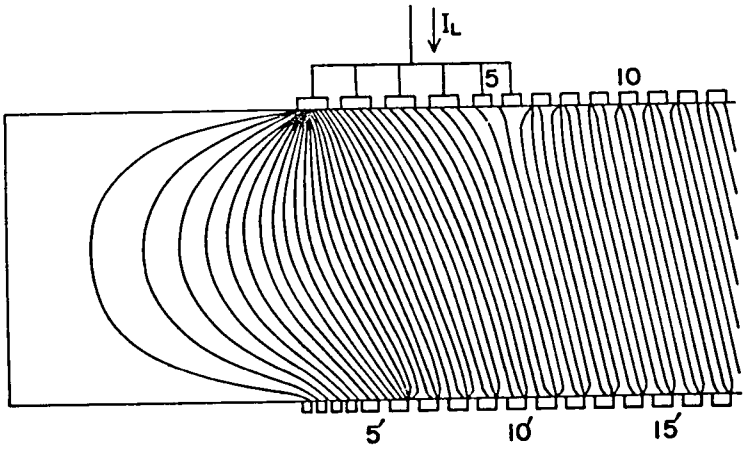

(b) Current distribution (contour interval: 1500A/m).

Fig. 4.6 Potential and current distributions calculated by FDM (φ_0=68.2°, N_{out}=6, μ=1/6, $I_L=4\times10^4$A, g=0).

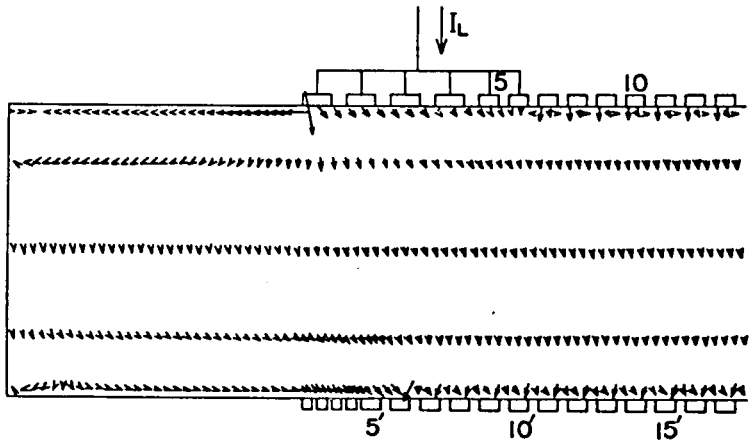

Fig. 4.7 Current pattern calculated by ECM for the same conditions as in Figs. 4.6 (maximum current density: $24.1\times10^4 A/m^2$).

Next, in Fig. 4.8, there is plotted the potential difference V_n which is calculated by the above two methods with the same conditions as in Figs. 4.6.

From the above explanation, it can be said that the calculation

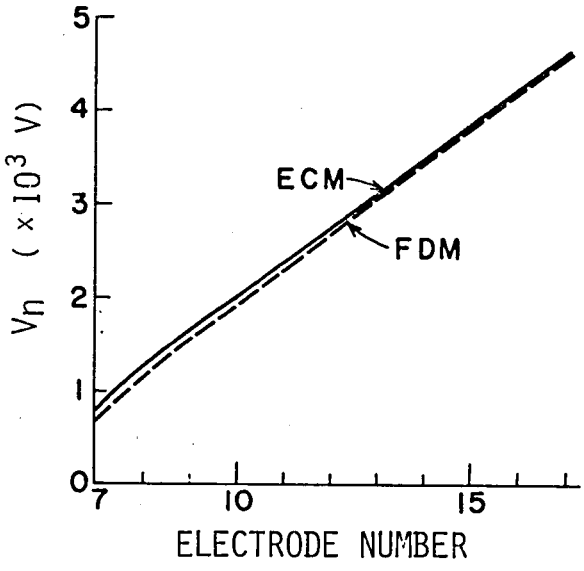

Fig. 4.8 Comparison of V_n calculated by ECM and FDM.

results by the ECM sufficiently agree with the highly accurate ones by the FDM and so are enough reliable.

Next, let us refer to the cpu time. For example, the result by the FDM in Fig. 4.3(b) was obtained with about 36,000 meshes by the successive over relaxation (SOR) method and by using the FACOM M-190 of Data Processing Center, Kyoto University, and it needed about 500 seconds. On the other hand, the result by the ECM in Fig. 4.4 was obtained with about 750 space elements by the direct method, and it needed only 1.3 seconds.

Finally, let us examine the following relations

$$\left.\begin{aligned} E_y &= a\,E_x \quad , \\ I_L &= A\,(J_x + a\,J_y) \quad , \\ \text{where} \quad a &= -\cot\varphi \quad , \end{aligned}\right\} \tag{4.3}$$

in which a is the electrode inclination parameter and A the duct cross-section. The above relations are the well-known diagonal constraints used for usual one-dimensional analysis. From Figs. 4.3(a) and (b), or 4.6(a) and (b), it will be seen that Eqs. (4.3) are no longer held in the end region with the output electrodes because of distortions of the potential and current distributions.

4.6 Electrical Effects of Nozzle and Diffuser Regions near Duct Ends

The inlet and exit of the MHD generator duct are usually connected with a nozzle exit and a diffuser inlet, respectively. In numerical calculation of the current and potential, the whole or a part of the above nozzle and diffuser regions must be also considered with the generator duct. Accordingly, in this section, let us discuss how long we should take the length L_{ins} of the nozzle or the diffuser in the

flow direction which stands for the extent of the above regions.

Figure 4.9 shows the influence of L_{ins} on the current density J^*_{1u} at the upstream end of the upper first output electrode 1, and on $J^*_{1'u}$ at the same end of the lower first output electrode 1'. It also shows the voltage V^*_5 between the output electrodes and the electrode 5 which is nearest to them. Here, those values are normalized by the values of the similar current densities or the voltage for $L_{ins} = 2m$, respectively, and are obtained for $\varphi_0 = 45°$, $N_{out} = 4$, $\mu = 2/3$, $I_L = 2\times10^4 A$, $x_{B1} = 2m$, and $g = 2.5T/m$ by the ECM. From Fig. 4.9, it will be seen that we should take $L_{ins} \fallingdotseq 1.5m$, say $L_{ins} \fallingdotseq H$ for our duct size to evaluate accurately the current concentration at the upstream ends of the output electrodes. On the other hand, we can satisfactorily calculate the potential of the electrodes with $L_{ins} \fallingdotseq 0.5m$, viz. $L_{ins} \fallingdotseq H/3$. From these, for the computation of the potential and current distributions already shown in Figs. 4.3(a), (b) and 4.4, $L_{ins} = 1.5m$ was used.

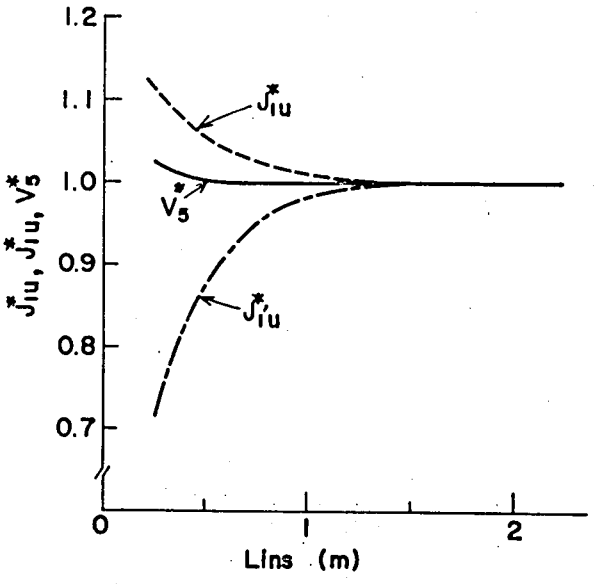

Fig. 4.9 Influence of L_{ins} on J^*_{1u}, $J^*_{1'u}$, and V^*_5 (φ_0=45°, N_{out}=4, μ=2/3, I_L=2×10⁴A, x_{B1}=2m, g=2.5T/m).

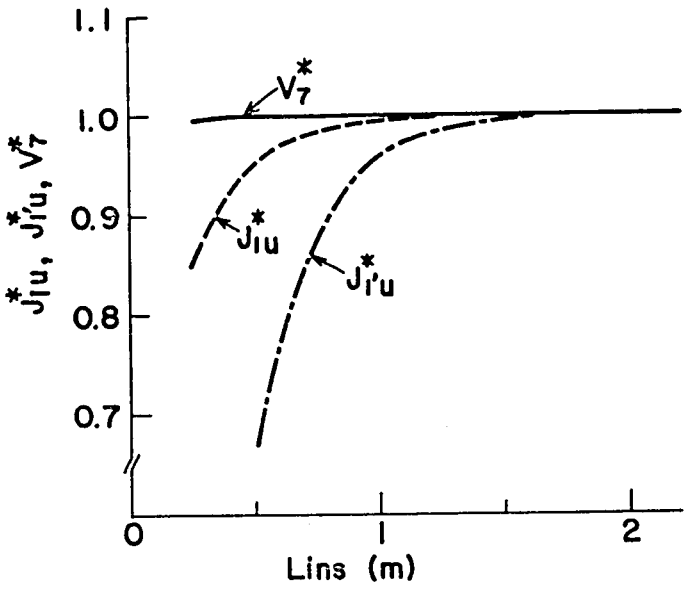

Fig. 4.10 Influence of L_{ins} on J^*_{1u}, $J^*_{1'u}$, and V^*_7 (φ_0=68.2°, N_{out}=6, μ=1/6, I_L=4×10^{4}A, g = 0).

Next, Fig. 4.10 shows the influence of L_{ins} on J^*_{1u}, $J^*_{1'u}$, and V^*_7 which is the normalized voltage between the output electrodes and the electrode 7, where φ_0 = 68.2°, μ = 1/6, I_L = 4×10^{4}A, and g = 0 are used. From this figure, it may be said that the conclusions in this case are almost the same as those in Fig. 4.9, although a great deal of current flows into the nozzle region as seen in Figs. 4.6(b) and 4.7, where we take L_{ins} = 1.5m.

4.7 Current Concentration at Output Electrodes

4.7.1 Influence of distribution of applied magnetic flux

In Table 4.2(a), for the various values of x_{B1} and g, there are

shown the calculated results of the magnitudes J_{1u} and J_{4d} of the current density vectors $\mathbb{J}_{1u}$ and $\mathbb{J}_{4d}$ at the front end of the upper first output electrode 1 and the rear end of the upper last output electrode 4, respectively, and those of the magnitudes $J_{1'u}$ and $J_{4'd}$ of the current density vectors $\mathbb{J}_{1'u}$ and $\mathbb{J}_{4'd}$ at the front end of the lower first output electrode 1' and at the rear end of the lower last output electrode 4', respectively, with the angles θ_{1u}, θ_{4d}, $\theta_{1'u}$, and $\theta_{4'd}$ which are the inclination angles of $\mathbb{J}_{1u}$, $\mathbb{J}_{4d}$, $\mathbb{J}_{1'u}$, and $\mathbb{J}_{4'd}$, respectively, to the x axis. Also, in the same table, there are given the values of the average applied magnetic inductions $\bar{B}_{out}$ in the output electrode region for the various x_{B1} and g.

The table indicates that J_{4d} and $J_{1'u}$ are small, in other words, the current concentration is not so intense at the rear end of the electrode 4 and the front end of the electrode 1'. Also, it indicates that the smaller $\bar{B}_{out}$ becomes, the weaker J_{1u} becomes. Accordingly, when x_{B1} and g become large and therefore $\bar{B}_{out}$ becomes small, the

Table 4.2(a) Influence of x_{B1} and g on current concentration ($\varphi_0 = 45°$, Nout = 4, $\mu = 2/3$, $I_L = 2\times10^4$A).

x_{B1} m	g T/m	$\bar{B}_{out}$ T	Upper Output Electrodes				Lower Output Electrodes			
			$J_{1u}=(J_{1u}, \theta_{1u})$ ($\times10^4$A/m², rad)		$J_{4d}=(J_{4d}, \theta_{4d})$ ($\times10^4$A/m², rad)		$J_{1'u}=(J_{1'u}, \theta_{1'u})$ ($\times10^4$A/m², rad)		$J_{4'd}=(J_{4'd}, \theta_{4'd})$ ($\times10^4$A/m², rad)	
—	0	6	20.2	−1.1	0.3	−1.3	0.3	2.9	7.4	−1.7
0	1	6	19.9	−1.1	0.3	−1.3	0.4	2.9	7.4	−1.7
	2.5	6	19.4	−1.1	0.3	−1.3	0.6	2.9	7.4	−1.7
	5	6	18.4	−1.1	0.3	−1.3	1.0	2.9	7.3	−1.7
1	1	5.30	18.1	−1.1	0.5	−0.8	0.6	2.9	6.5	−1.8
	2.5	4.24	13.7	−1.1	0.8	−0.5	1.3	2.7	4.7	−1.9
	5	2.48	4.5	−1.3	1.4	−0.4	2.2	2.2	1.0	−2.3
2	1	4.30	15.7	−1.1	0.7	−0.6	0.5	2.8	4.6	−1.8
	2.5	1.74	3.9	−1.4	1.5	−0.5	1.3	2.2	1.3	0.5
	5	0	0.6	−1.9	2.0	−1.0	1.2	1.6	4.8	0.2
3	1	3.30	12.5	−1.2	0.9	−0.5	0.4	2.7	2.5	−1.6
	2.5	0.02	0.6	−1.9	2.0	−0.9	1.1	1.6	4.7	0.2
	5	0	0.6	−1.9	1.7	−1.0	1.2	1.6	4.9	0.3

concentration is much more relaxed compared with the current concentration in the case of $g = 0$. In this case, for reference, the value of the current density at the electrode end in the periodic region becomes $3.1 \times 10^4 A/m^2$.

In the case of a large $\bar{B}_{out}$, J_{1u} is enormously large. For such phenomena, the following two reasons are thought. Firstly, as in the case of occurrence of the effect of the finite electrode segmentation, the Hall electric field induced in the vicinity of the output electrodes is short-circuited by the electrodes of a finite width. Secondly, as seen from Fig. 4.6(a), even in the nozzle region near the output electrode 1, a large electromotive force is induced, and to compensate for the force, the current flows into the nozzle region from the upstream end of the electrode 1.

Table 4.2(a) also shows that $J_4'_d$ is fairly heavy when $\bar{B}_{out}$ is large. This is also thought to be owing to the finite electrode

Table 4.2(b) Influence of x_{B1} and g on current concentration ($\varphi_0 = 45°$, Nout = 4, $\mu = 1/6$, $I_L = 6 \times 10^4$A) .

x_{B1} m	g T/m	$\bar{B}_{out}$ T	Upper Output Electrodes				Lower Output Electrodes			
			$J_{1u} = (J_{1u}, \theta_{1u})$ ($\times 10^4$A/m^2, rad)		$J_{4d} = (J_{4d}, \theta_{4d})$ ($\times 10^4$A/m^2, rad)		$J_1'_u = (J_1'_u, \theta_1'_u)$ ($\times 10^4$A/m^2, rad)		$J_4'_d = (J_4'_d, \theta_4'_d)$ ($\times 10^4$A/m^2, rad)	
—	0	6	24.2	−1.4	3.7	−0.7	1.7	−0.8	4.3	−0.3
0	1	6	23.5	−1.4	3.7	−0.7	1.4	−0.8	4.3	−0.3
	2.5	6	22.5	−1.4	3.7	−0.7	0.8	−0.8	4.3	−0.3
	5	6	20.7	−1.4	3.8	−0.7	0.1	2.4	4.3	−0.2
1	1	5.30	19.2	−1.4	4.2	−0.7	1.0	−0.9	5.3	0.1
	2.5	4.24	12.0	−1.5	4.8	−0.7	0.5	2.1	7.4	0.3
	5	2.48	3.5	−1.7	5.6	−0.7	2.5	1.8	10.6	0.4
2	1	4.30	14.8	−1.5	4.6	−0.7	5.9	−1.0	7.7	0.3
	2.5	1.74	3.5	−1.7	5.5	−0.8	2.4	1.7	12.7	0.4
	5	0	1.8	−1.9	5.1	−1.0	3.7	1.6	15.1	0.3
3	1	3.30	10.6	−1.6	5.0	−0.8	0.1	2.0	10.1	0.4
	2.5	0.02	1.8	−1.9	5.2	−0.9	3.7	1.6	15.0	0.3
	5	0	1.8	−1.9	5.0	−1.0	3.7	1.6	14.7	0.3

segmentation. Further, it is a noticeable tendency that as $\bar{B}_{out}$ decreases, $J_4'_d$ decreases first and then increases again. The reason why $J_4'_d$ becomes large in the case of $\bar{B}_{out} = 0$ is perhaps that due to discrepancy of the electrode arrangements in the anode and the cathode, the electric field E_x near the lower down stream in the region with the output electrode is greater than the one near the upper down stream in the same region. Therefore, much load current flows out of the down stream end of the electrode 4'.

Next, the digital calculation results similar to those in Table 4.2(a) are represented in Table 4.2(b), where $\varphi_0 = 45°$, $N_{out} = 4$, $\mu = 1/6$, and $I_L = 6\times10^4$A. Generally speaking, the above concluding remarks obtained from Table 4.2(a) can be applied to the results in Table 4.2 (b). Especially, in the case of $\bar{B}_{out} = 0$, $J_4'_d$ increases very much. And by comparing $J_4'_d$ in Table 4.2(a) with the same in (b), it may be said that $J_4'_d$ is almost proportional to I_L. For reference, Fig. 4.11 shows the current pattern in the case where $\varphi_0 = 45°$, $N_{out} = 4$, $\mu = 1/6$, $I_L = 6\times10^4$A, $x_{B1} = 2$m, and $g = 2.5$T/m. The maximum current density of 12.5×10^4A/m^2 appears at the down stream end of the electrode 4'.

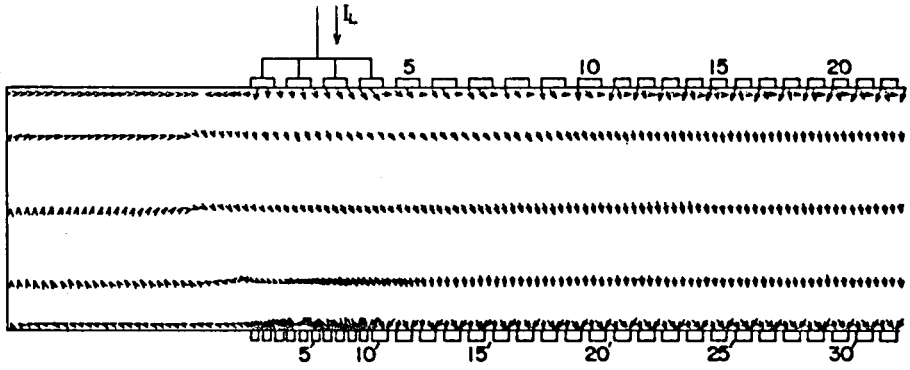

Fig. 11 Current pattern calculated by ECM ($\varphi_0 = 45°$, $N_{out} = 4$, $\mu = 1/6$, $I_L = 6\times10^4$A, $x_{B1} = 2$m, $g = 2.5$T/m, maximum current density: 12.5×10^4A/m^2).

4.7.2 Influence of load current

Table 4.3(a) shows the calculated results of the current densities J_{1u}, J_{4d}, $J_{1'u}$, and $J_{4'd}$ with the angles Θ_{1u}, Θ_{4d}, $\Theta_{1'u}$, and $\Theta_{4'd}$, respectively, for the various load currents I_L in the case of $\varphi_0 = 45°$, $N_{out} = 4$, $\mu = 2/3$, $x_{B1} = 2m$, and $g = 2.5T/m$. In this table, the load current I_L is calculated by the following equations derived from Eqs. (2.3) and (4.3), in which $\beta_i = 0$,

$$\left.\begin{aligned} & I_L = A\sigma u B_0 (\beta_0 - a)(1-\kappa_0)/(1+\beta_0^2), \\ \text{where} \quad & \kappa_0 = -(1+a^2)E_x/\{(\beta_0 - a)uB_0\}, \\ & a = -\cot\varphi_0, \end{aligned}\right\} \qquad (4.4)$$

in which β_0 the Hall parameter for B_0, and κ_0 the load factor in the periodic region, which is listed in Table 4.3(a). From the table, it will be seen that J_{1u} increases more or less with the increase of I_L. On the other hand, $J_{4'd}$ runs into the electrode 4' and decreases with I_L when I_L is small. When I_L is large, inversely it flows out of the same 4' and increases with I_L. The current densities J_{4d} and $J_{1'u}$ are always considerably smaller than J_{1u} and $J_{4'd}$. The current patterns in the case of $I_L = 2\times10^4$A were already shown in Figs. 4.3(b) and 4.4. In addition, we get the interesting result that $J_{1'u}$ and $\Theta_{1'u}$ vary with increase of I_L. It suggests that the position of the

Table 4.3(a) Influence of load current on current concentration ($\varphi_0 = 45°$, $N_{out} = 4$, $\mu = 2/3$, $x_{B1} = 2m$, $g = 2.5T/m$, $\bar{B}_{out} = 1.47T$).

I_L ($\times10^4$A)	κ_0	Upper Output Electrodes				Lower Output Electrodes			
		$J_{1u} = (J_{1u}, \theta_{1u})$ ($\times10^4$A/m², rad)		$J_{4d} = (J_{4d}, \theta_{4d})$ ($\times10^4$A/m², rad)		$J_{1'u} = (J_{1'u}, \theta_{1'u})$ ($\times10^4$A/m², rad)		$J_{4'd} = (J_{4'd}, \theta_{4'd})$ ($\times10^4$A/m², rad)	
0.1	0.97	2.9	−1.4	0.6	−1.1	0.5	−1.0	9.2	−2.2
1	0.69	3.4	−1.4	1.0	−0.6	0.4	2.2	4.3	−2.1
2	0.37	3.9	−1.4	1.5	−0.5	1.3	2.2	1.3	0.5
3	0.06	4.4	−1.4	2.1	−0.4	2.2	2.2	6.8	0.8

Table 4.3(b) Influence of load current on current concentration (φ_0=45°, Nout=4, $\mu = 2/3$, x_{B1}=1m, $g = 2.5$T/m, $\bar{B}$out=4.24T).

I_L (×10⁴A)	κ_0	Upper Output Electrodes				Lower Output Electrodes			
		$J_{1u}=(J_{1u}, \theta_{1u})$ (×10⁴A/m², rad)		$J_{4d}=(J_{4d}, \theta_{4d})$ (×10⁴A/m², rad)		$J_1'_u=(J_1'_u, \theta_1'_u)$ (×10⁴A/m², rad)		$J_4'_d=(J_4'_d, \theta_4'_d)$ (×10⁴A/m², rad)	
0.1	0.97	12.3	−1.1	1.2	−2.8	1.3	−0.4	25.4	−2.0
1	0.69	13.0	−1.1	0.5	−2.1	0.1	−0.4	15.6	−2.0
2	0.37	13.7	−1.1	0.8	−0.5	1.3	2.7	4.6	−1.9
3	0.06	14.4	−1.1	1.7	−0.2	2.6	2.7	6.4	1.0

eddy current changes with I_L in the upstream region of the lower output electrode.

Next, Table 4.3(b) shows the calculated values of κ_0, J_{1u}, θ_{1u}, etc. for the various values of I_L as in Table 4.3(a), in the case of $\varphi_0 = 45°$, $N_{out} = 4$, $\mu = 2/3$, $x_{B1} = 1$m, and $g = 2.5$T/m. Although J_{1u}, etc. in Table 4.3(b) are much larger than those in Table 4.3(a), the above conclusions derived from Table 4.3(a) can be nearly applied to Table 4.3(b).

4.7.3 Influence of number of output electrodes

In Table 4.4, there are listed the calculated values of J_{1u}, J_{Nd}, $J_1'_u$, and $J_N'_d$ for the various values of N_{out} when $\varphi_0 = 45°$, $\mu = 2/3$, and $I_L = 2\times10^4$A, with θ_{1u}, θ_{Nd}, $\theta_1'_u$, and $\theta_N'_d$, respectively,

Table 4.4 Influence of N_{out} on current concentration ($\varphi_0 = 45°$, $\mu = 2/3$, $I_L = 2\times10^4$A, $x_{B1} = 2$m, $g = 2.5$T/m) .

Nout	Upper Output Electrodes				Lower Output Electrodes			
	$J_{1u}=(J_{1u}, \theta_{1u})$ (×10⁴A/m², rad)		$J_{Nd}=(J_{Nd}, \theta_{Nd})$ (×10⁴A/m², rad)		$J_1'_u=(J_1'_u, \theta_1'_u)$ (×10⁴A/m², rad)		$J_N'_d=(J_N'_d, \theta_N'_d)$ (×10⁴A/m², rad)	
1	5.4	−1.3	3.6	−0.7	3.3	2.2	8.7	0.97
2	4.3	−1.4	2.4	−0.6	2.0	2.2	5.5	0.89
4	3.9	−1.4	1.5	−0.5	1.3	2.2	1.3	0.52
6	3.9	−1.4	1.1	−0.4	1.2	2.2	2.4	−2.1
8	3.9	−1.4	0.8	−0.4	1.3	2.2	5.3	−2.4
10	4.0	−1.4	0.4	−0.6	1.4	2.2	7.6	−2.5

where J_{Nd} and $J_{N'd}$ are the magnitudes of the current density vectors $\mathbf{J}_{Nd}$ and $\mathbf{J}_{N'd}$ at the down stream ends of the output electrodes N_{out} and N'_{out}, respectively, and θ_{Nd} or $\theta_{N'd}$ the angle between the x axis and $\mathbf{J}_{Nd}$ and $\mathbf{J}_{N'd}$, respectively. From Table 4.4, it is seen that J_{1u} decreases and reaches a constant value, and J_{Nd} rapidly decreases as N_{out} increases. $J_{N'd}$ flows out of the electrode N'_{out} and decreases with N_{out} when N_{out} is small, and inversely, it runs into the electrode N'_{out} and increases with N_{out} when N_{out} is large, and $J_{1'u}$ decreases first and then increases a little as N_{out} increases. In this connection, from the table, it is made clear that the electrical output power has the maximum value for $N_{out} = 4$ to 6.

By the above discussion, to remove the current concentration and to make the generated power large, it is necessary to determine the suitable output electrode number N_{out}. The current pattern for $N_{out} = 4$ was already shown in Fig. 4.3(b) or 4.4.

4.8 Concluding Remarks

The main conclusions derived from the above numerical analysis are as follows:

(1) It was ascertained that the current and potential distributions in the end regions of the large scale diagonal type generator calculated by the ECM agree well with those by the FDM.

(2) The diagonal constraints used for the usual one-dimensional analysis are no longer held in the duct end regions because of the end effect.

(3) The nozzle and the diffuser must be taken into account in the gas flow direction at least to the extent of the duct height in numerical analysis of the current and potential distributions.

(4) The current concentration occurs intensively at the upstream end of the upper first output electrode and at the downstream end of

the lower last output electrode. The concentration can be largely removed by an appropriately applied magnetic flux distribution. Since the number of output electrodes also gives influences on the current concentration, the generated power, etc., it must be suitably chosen.

CHAPTER 5

QUASI-TWO-DIMENSIONAL ANALYSIS OF SINGLE-LOAD GENERATOR OF CONSTANT SQUARE CROSS-SECTION DUCT WITH NO BOUNDARY LAYER

5.1 Introduction

Already, in chapter 2, a new two-dimensional equivalent circuit of a diagonal type generator has been derived. And in chapters 3 and 4, suitable compositions of the equivalent circuits for the central and end regions of the generator were determined, and the electrical characteristics of these regions were clarified by the ECM. Also it was ascertained that the results calculated by the ECM in much shorter cpu time sufficiently agree with the ones by the FDM and FEM.

In the above calculation, however, variations of gasdynamical quantities such as p, t, u, etc. in the gas flow direction are not considered. Up to now, the whole generator performances have been analysed by the conventional quasi-one-dimensional MHD theory* [41, 42]. However, in this theory, the diagonal constraints (4.3) are used which are derived under the following assumptions: (1) all electrical quantities are constant in the region where a pair of electrode is settled, (2) diagonal angle is constant in the range of

---

* See Appendix I.

adjacent electrode pair, (3) cross-section of the duct is constant in the gas flow direction. In the actual generator, however, the assumption (2) is not held in the both inlet and exit regions, the assumptions (1) and (3) are not kept in general even in the central region of the duct. Consequently, the theory in which diagonal constraints are not used is needed.

In this chapter, first, we will introduce a new theory to analyse numerically whole electrical and gasdynamical performances of the single-load diagonal type generator with no boundary layer [59-63]. Distributions of the electrical quantities in the duct are calculated by means of the two-dimensional ECM and distributions of the gasdynamical ones by a modified quasi-one-dimensional theory with an iterative technique. Therefore, it is named a quasi-two-dimensional theory by the author.

Next, with many numerical calculation results concerning a large scale diagonal type generator of constant square cross-section driven by combustion gas of heavy oil fuel, the influences of the applied magnetic flux distribution, the finite electrode segmentation, the number of output electrodes, etc. on the output power and electrical efficiency of the whole generator, current concentration at the electrode end, etc. are made clear. Also the results obtained by the quasi-two-dimensional and an ideal quasi-one-dimensional theories are comparatively studied.

5.2 Quasi-Two-dimensional Theory

5.2.1 Arrangement of electrodes and distribution of applied magnetic flux

Figure 5.1 shows a schematic diagram of the region from the inlet to the central part of the diagonal type MHD generator duct,

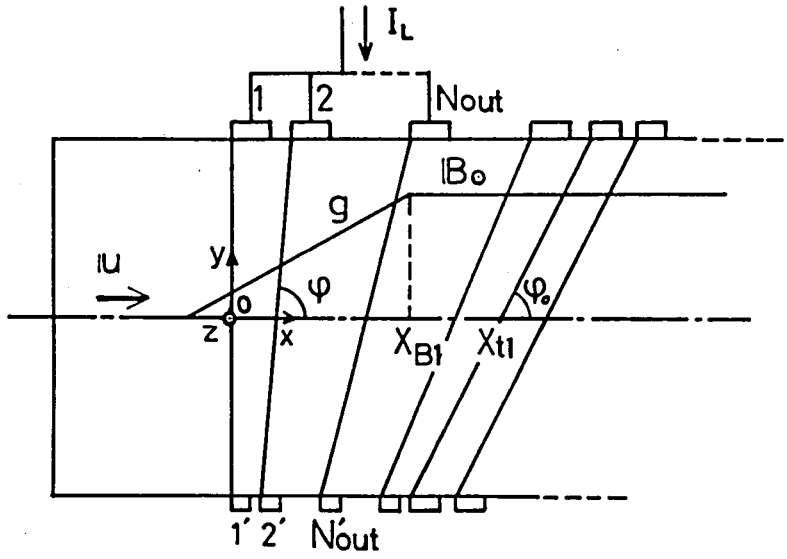

Fig. 5.1 Schematic diagram of duct inlet region of diagonal type generator.

which is adopted as the research object in this chapter, with the electrode arrangement and the applied magnetic flux distribution. In the figure, each symbol has the same content as in Fig. 4.1, and the diagonal angle φ and the magnetic flux density B are assumed as follows:

$$\varphi = \begin{cases} \cot^{-1}\left(x \cot \varphi_0 / x_{t1} \right) & \text{for } 0 < x < x_{t1}, \\ \varphi_0 & \text{for } x_{t1} \leqq x \leqq x_{t2}, \\ \cot^{-1}\left[\cot \varphi_0 \left\{ 1 - (x - x_{t2}) / (L - x_{t2}) \right\} \right] & \text{for } x_{t2} < x < L, \end{cases} \tag{5.1}$$

and

$$B = \begin{cases} 0 & \text{for } x \leqq x_{B1} - B_0/g, \text{ or } x \geqq B_0/g + x_{B2}, \\ B_0 + g\,(x - x_{B1}) & \text{for } x_{B1} - B_0/g < x < x_{B1}, \\ B_0 & \text{for } x_{B1} \leqq x \leqq x_{B2}\ , \\ B_0 - g\,(x - x_{B2}) & \text{for } x_{B2} < x < x_{B2} + B_0/g\ , \end{cases} \tag{5.2}$$

as in Eqs. (4.1) and (4.2), respectively.

5.2.2 Two-dimensional analysis of electrical quantities

Let us divide the generator duct shown in Fig. 5.1 into many space elements and replace each element with the equivalent circuit derived in chapters 2 to 4. Then we can express whole generator duct by an equivalent network.

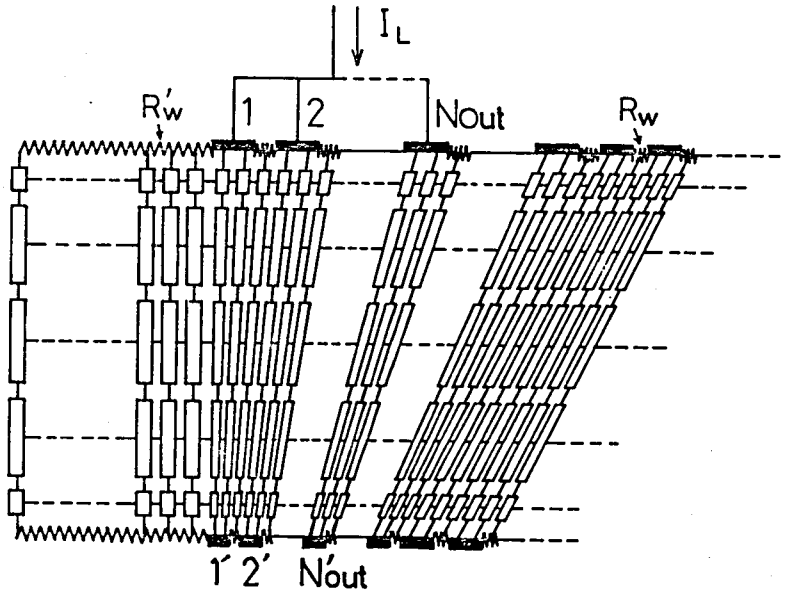

Fig. 5.2 Illustration of duct inlet region by using equivalent network.

It has been already shown in chapters 3 and 4 that generator characteristics obtained by the ECM sufficiently agree with those by the FDM or the FEM when appropriate magnitude and number of space elements are selected in both center and end regions of the duct. From the results, the generator duct shown in Fig. 5.1 can be expressed by an equivalent network as shown in Fig. 5.2. In addition, as described in subsection 2.3.2, the values of the electromotive force and the resistances in each space element can be numerically determined when the values of p, T, u, and B in each space element are given.

Next, many simultaneous circuit equations for the unknown currents flowing in the resistances in the equivalent network are obtained by Kirchhoff's laws. When they are solved numerically, the values of the currents and further the x and y components of the current density $\mathbb{J}$ and electric field $\mathbb{E}$ in each element are determined.

Input power p_{ei} in the space element i of the volume Δv_i, which is mechanical work done by the gas in pushing itself against Lorentz force, is given by

$$\left.\begin{aligned} p_{ei} &= \int_{\Delta v_i} \mathbb{J} \cdot (\mathbb{u} \times \mathbb{B})\, dv = J_{yi}\, u_i\, B\, \Delta v_i \\ &= (u\, B\, h_e\, I_\eta)_i, \\ i &= 1,2, \ldots, N_t \quad , \end{aligned}\right\} \qquad (5.3)$$

where N_t is total number of space elements in the whole generator. Also, electrical output power P and electrical efficiency η_e of the generator duct are given by

$$P = -\sum_{i=1}^{N_t} (E_{xi}\, J_{xi} + E_{yi}\, J_{yi})\, \Delta v_i \qquad (5.4)$$

$$\eta_e = P / \sum_{i=1}^{N_t} Pei \ . \qquad (5.5)$$

5.2.3 Quasi-one-dimensional analysis of gasdynamical quantities

By applying the assumptions in Eqs. (2.2) to the electric field $\mathbf{E}$, current density $\mathbf{J}$, the gas flow velocity $\mathbf{u}$, and the magnetic flux $\mathbb{B}$, ideal quasi-one-dimensional MHD equations, in which friction loss and heat transfer in the boundary layer and finite electrode segmentation effect are ignored, are given as follows:

the continuity equation

$$\rho u A = m_0, \qquad (5.6)$$

the momentum equation

$$\rho u \, du/dx + dp/dx = J_y B , \qquad (5.7)$$

the energy equation

$$\rho u \, d(h + u^2/2)/dx = - P_o, \qquad (5.8)$$

where P_o is the output power density which is given by

$$P_o = - (E_x J_x + E_y J_y) , \qquad (5.9)$$

and the state equation for the working gas is given by

$$p = \rho R T. \qquad (5.10)$$

In the above equations, A is the duct cross-section, and h, m_0, p, R,

T, and ρ are the enthalpy, mass flow rate, pressure, gas constant, temperature, and mass density of the working fluid, respectively.

5.2.4 Quasi-two-dimensional theory

When Eqs. (5.6) to (5.10) are applied to quasi-two-dimensional analysis, $\langle J_y \rangle$ and $\langle P_o \rangle$ must be used instead of J_y and P_o, respectively, in Eqs. (5.7) to (5.9), where $\langle J_y \rangle$ and $\langle P_o \rangle$ are the average values of J_y and P_o, respectively, in the y-direction within a small interval (x, x+Δx) in the duct. Those are given by

$$\langle J_y \rangle = \sum_i J_{yi} \Delta v_i \Big/ \sum_i \Delta v_i \quad , \tag{5.11}$$

$$\langle P_o \rangle = -\sum_i (E_{xi} J_{xi} + E_{yi} J_{yi}) \Delta v_i \Big/ \sum_i \Delta v_i \quad , \tag{5.12}$$

where Δv_i is the volume of the space element i which is located in the above interval.

Now, first, when the values of the duct cross-section A, the applied magnetic flux density B, the pressure p_0, temperature T_0, and velocity u_0 at the duct inlet are given, Eqs.(5.6) to (5.10) can be numerically solved. Here, only in the first process, Ex, Ey, Jx, and Jy in Eqs. (5.7) and (5.9) are determined by using Eqs. (2.3), (3.3), and (4.3). Then, the ideal one-dimensional distributions of the gas-dynamical quantities such as p, T, and u are obtained.

Next, the distributions p(x), T(x), and u(x) of p, T, and u, respectively, are applied to the two-dimensional numerical analysis by the equivalent circuit. Namely, by using p(x), T(x), and u(x), the values of σ, β, e_η, R_ξ, etc. in each space element are numerically determined. Then, by solving the simultaneous circuit equations for unknown currents as mentioned in subsection 2.5.2, the values of the currents are obtained. Next, with those values, Ex, Ey, Jx, and Jy in each space element are calculated.

the duct inlet and exit heights, respectively. The total number N of the electrode pairs is varied to investigate finite electrode segmentation effect, and the number N_{out} of the output electrodes is done in proportion to N. Next, the load current I_L and the pressure p_0, the temperature T_0, and the velocity u_0 at the duct inlet are appropriately determined from the many results of one-dimensional numerical analysis of the generator performances. And β_i is assumed to be zero.

In this thesis, the gas enthalpy h and constant R are given as follows:

$$h = \begin{cases} 2.103\times10^{6} + 1.320\times10^{3}(T-1800) & \text{for } T < 1800\text{K}, \\ 2.103\times10^{6} + 1.320\times10^{3}(T-1800) + 1.066\, p^{-0.2847} & \\ \quad \times (T-1800)^{2.478} & \text{for } T \geq 1800\text{K}, \end{cases} \tag{5.13}$$

$$R = \begin{cases} 2.898\times10^{2} & \text{for } T < 1800\text{K}, \\ 2.898\times10^{2} + 2.574\times10^{-7} p^{-0.396} (T-1800)^{3.243} & \\ & \text{for } T \geq 1800\text{K}, \end{cases} \tag{5.14}$$

where h is in J/kg, R in J/kg/K, p in atm., T in K, and the values of these constants for the used combustion gas are derived from the data in Ref. [41].

5.4 Performance Characteristics

5.4.1 Influence of distribution of applied magnetic flux

Table 5.2 shows the calculated results of P, P', P/P', η_e, η_e',

Further, by using the above E_x, E_y, J_x, and J_y, the distributions of $\langle J_y \rangle$ and $\langle P_o \rangle$ along the x-axis are newly obtained. Then, substituting those $\langle J_y \rangle$ and $\langle P_o \rangle$ instead of J_y and P_o in Eqs. (5.6) to (5.10), the new one-dimensional distributions of the gasdynamical quantities are determined.

After some repetitions of such calculation processes, two-dimensional distributions of the electrical quantities and one-dimensional distributions of the gasdynamical quantities in the generator duct are obtained.

In this connection, the conductivity σ and the Hall parameter β are calculated by Eqs. (3.3).

5.3 Numerical Conditions

Working gas used in calculation is a combustion product of heavy oil fuel and oxygen of a stoichiometric factor 1.1, where KOH and K_2SO_4 are seeded so that the potassium atom is contained in a ratio of 1 wt% to the combustion gas, as described in subsection 3.2.2.

The numerical conditions for calculation are shown in Table 5.1, where L_N and L_D are the length of nozzle and diffuser regions used in calculation, respectively, and those are assumed to be equal to

Table 5.1 Numerical conditions used in calculation.

$H \times D \times L$	(m)	1.5×1.5×10	$x_{B1}=L-x_{B2}$	(m)	0, 1, 1.5, 2
L_N, L_D	(m)	1.5	g	(T/m)	0, 2.5
φ_0	(°)	30	I_L	($\times 10^4$A)	1.5, 1.8
N		30 to 110	P_0	(atm)	5.5
N_{out}		1 to 11	T_0	(K)	2700
x_{t1}	(m)	2	u_0	(m/s)	175, 200
x_{t2}	(m)	8	B_0	(T)	6

Table 5.2 Influence of magnetic flux distribution ($N_{out} = 5$, $N = 70$, $I_L = 1.8\times10^4$A, $u_0 = 175$m/s).

g (T/m)	x_{B1} (m)	P (MW)	P' (MW)	P/P'	η_e (%)	η_e' (%)	J_{max} ($\times10^4$A/m^2)
0	0	111.2	115.5	0.963	48.0	62.2	9.2
2.5	1	96.6	104.4	0.925	51.5	60.7	5.9
	1.5	83.2	90.4	0.927	53.2	58.4	3.3
	2	69.2	73.4	0.942	53.0	54.7	3.6

and J_{max} when $N_{out} = 5$, $N = 70$, $I_L = 1.8\times10^4$A, and $u_0 = 175$m/s, where P and η_e are the output power and the electrical efficiency, respectively, obtained by the quasi-two-dimensional theory, P' and η_e' the same ones by the qusi-one-dimensional theory, and J_{max} the maximum current density by the former.

In the table, P and η_e are less than P' and η_e', respectively. This is probably caused by end effect and finite electrode segmentation effect. Furthermore, P decreases as x_{B1} increases, since a part of the duct with $B = B_0$ becomes short as x_{B1} increases. On the other hand, η_e is tend to increase and lastly saturate as x_{B1} increase.

Next, the values of J_{max} in the table indicate that remarkable current concentration appears when B does not attenuate in the end regions of the generator duct.

Furthermore, from the calculated results of current patterns, it was seen that large current concentration appeared at the down stream end of the lower last output electrode, except when $x_{B1} = 2$m. This is interpreted as follows: Firstly, since effective width of the exit output electrode is larger than that of central one, the Hall voltage induced in the vicinity of the electrode is short-circuited through the electrode. Secondly, the Hall parameter β in the exit

region of the generator is larger than that in the inlet region.

5.4.2 Influence of finite electrode segmentation

It has been often indicated so far that finite electrode segmentaion causes considerable reduction in performance characteristics of the generator [32]. In this subsection, let us discuss influence of finite electrode segmentation on generator performances.

In Fig. 5.3, there are plotted relations of P and η_e to N and <s/H> for $x_{B1} = 1.5$m, $g = 2.5$T/m, $I_L = 1.5\times10^4$A, and $u_0 = 200$m/s, where <s/H> is the averaged value of s/H with respect to L, and $N_{out}/N = 5/70$. From the figure, it is seen that the generator characteristics are not improved so much even when <s/H> < 0.1, namely influence of finite electrode segmentation on P and η_e is little found when <s/H> < 0.1, but it fairly comes out when <s/H> ≒ 0.2.

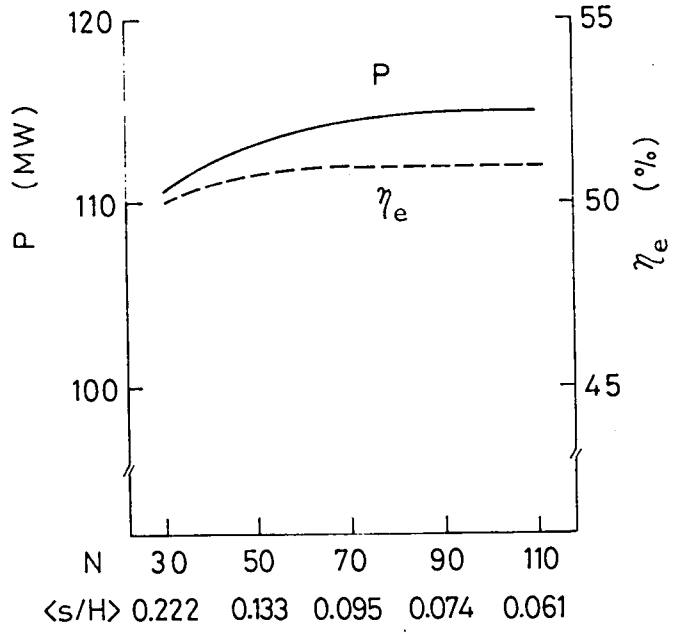

Fig. 5.3 Influence of finite segmentation on P and η_e ($x_{B1} = 1.5$m, $g = 2.5$T/m, $I_L = 1.5\times10^4$A, $u_0 = 200$m/s).

Next, Fig. 5.4 shows the distributions of p, T, and u along x-axis obtained by both the quasi-two-dimensional and the ideal quasi-one-dimensional theories with the same numerical conditions, where N = 70. It is found that p and T obtained by the former theory become a little high, but inversely the value of u slightly low compared with those by the latter.

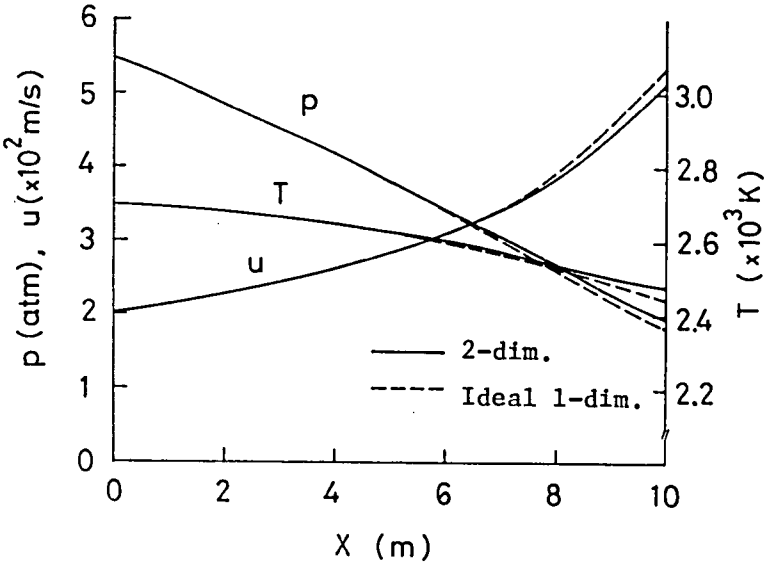

Fig. 5.4 Distribution of p, T, and u ($N_{out} = 5$, $N = 70$, $x_{B1} = 1.5$m, $g = 2.5$T/m, $I_L = 1.5\times10^4$A, $u_0 = 200$m/s).

Also Fig. 5.5 shows the distributions of $\langle -Jy \rangle$, $-Jy$, $\langle P_o \rangle$ and P_o along the x-axis obtained by both the quasi-two-dimensional and the ideal one-dimensional analyses with the same numerical conditions as in Fig. 5.4. Figure 5.5 tells that those abruptly vary within about 2m from the duct inlet and exit ends. Next, let us consider why the difference between the calculation results by the quasi-two-dimensional and the ideal analyses appears. As is well known, in the ideal

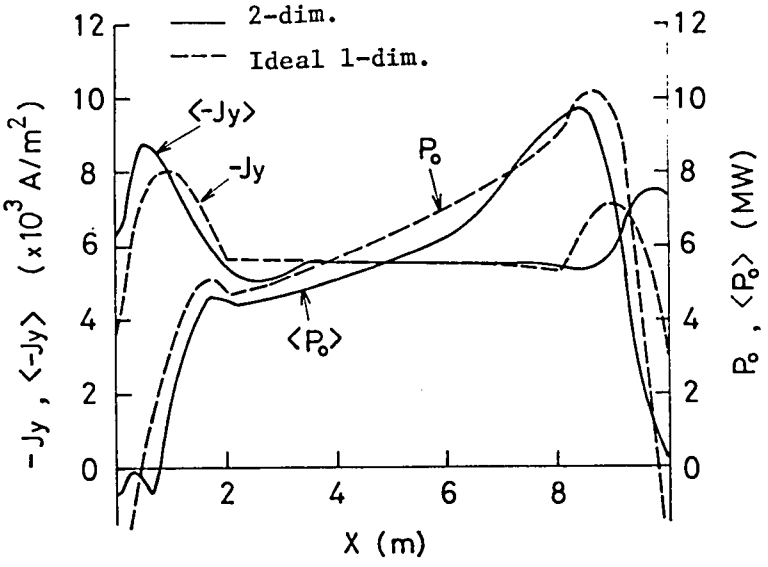

Fig. 5.5 Distribution of $-J_y$, $\langle -J_y \rangle$, P_o, and $\langle P_o \rangle$ ($N_{out} = 5$, $N = 70$, $x_{B1} = 1.5$m, $g = 2.5$T/m, $I_L = 1.5\times10^4$A, $u_0 = 200$m/s).

analysis, the already shown one-dimensional diagonal constraints (4.3) are used. The constraints are obtained under the assumption that all electrical quantities are constant within the wide range of electrode number in the generator duct. However, in the inlet and exit regions, such assumption can not be held, since the electrical quantities vary in the x and y directions because of existence of output electrodes, variation of φ and B, etc. Also even in the central region of the duct, the electrical quantities such as J, E, σ, and β are not essentially uniform. Therefore, Eqs. (4.3) can be applied no longer when accurate analysis is needed.

Figures 5.6(a) and (b) show the current patterns by current density vectors in each element under the same condion as in Figs.

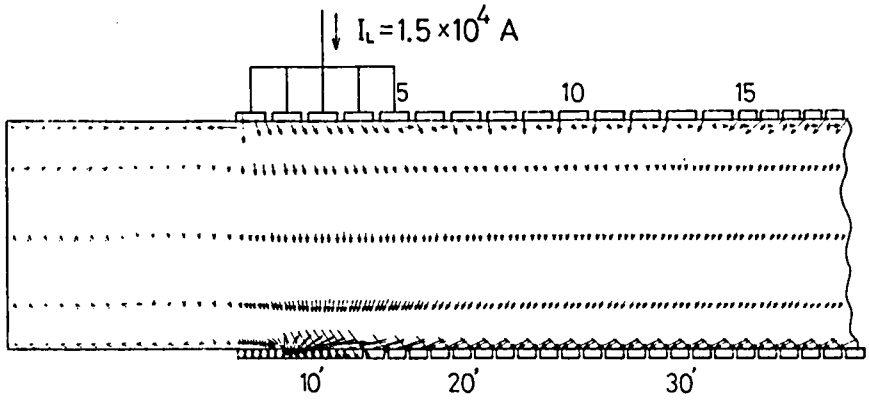

(a) Inlet region.

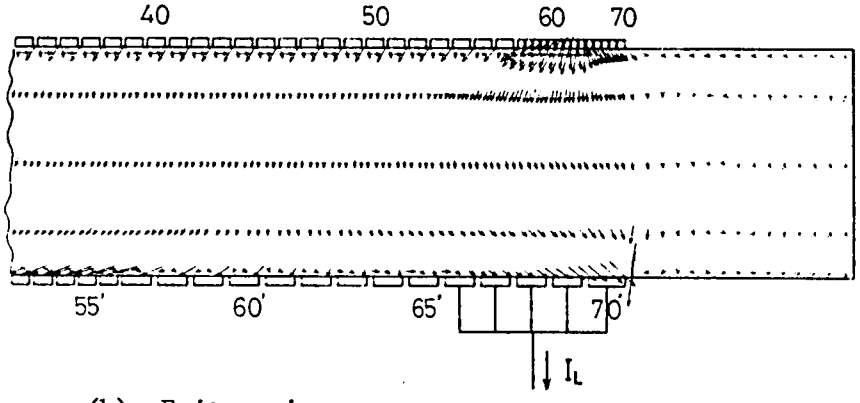

(b) Exit region.

Fig. 5.6 Current distribution in generator duct ($N_{out} = 5$, $N = 70$, $x_{B1} = 1.5$m, $g = 2.5$T/m, $I_L = 1.5\times10^4$A, $u_0 = 200$m/s).

5.4 and 5.5. In Fig. 5.6, the maximum current density $J_{max} = 4.4\times10^4$ A/m^2 appears at the down stream end of the lower last output electrode.

5.4.3 Influence of number of output electrodes

Figure 5.7 shows P , η_e, and J_{max} vs. N_{out} when $N = 70$, $x_{B1} = 1.5$m, $g = 2.5$T/m, $I_L = 1.5\times10^4$A, and $u_0 = 200$m/s. It should be noted that

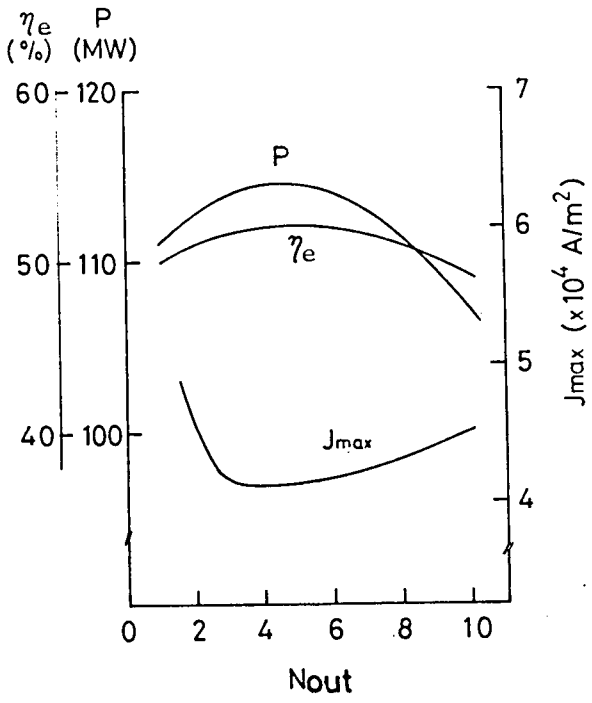

Fig. 5.7 Influence of N_{out} on P, η_e, and J_{max} ($N = 70$, $x_{B1} = 1.5$m, $g = 2.5$T/m, $I_L = 1.5\times10^4$A, $u_0 = 200$m/s).

when N_{out} is small or large, J_{max} is fairly large, but P and η_e are low. When $N_{out} \fallingdotseq 4$, J_{max} is minimum, and in the range of $4 < N_{out} < 6$, P and η_e are maximum. Therefore, we can say that there is a suitable value of N_{out}, which is 4 to 6 under the present numerical conditions.

5.5 Concluding Remarks

The main results obtained in this chapter are as follows:

(1) A new quasi-two-dimensional theory was derived, in which the whole electrical and gasdynamical quantities of the generator with no boundary layer are calculated by using the two-dimensional ECM and a modified quasi-one-dimensional MHD equations, respectively,

with an iterative technique.

(2) Influence of finite electrode segmentation on the output power and efficiency is little found when $\langle s/H \rangle < 0.1$, but it fairly comes out when $\langle s/H \rangle \fallingdotseq 0.2$.

(3) It was shown that the gas pressure and temperature obtained by the quasi-two-dimensional analysis become a little high, but inversely the output power, the electrical efficiency, the gas velocity, etc. low compared with those by the ideal quasi-one-dimensional analysis.

(4) The generator characteristics are considerably influenced by the number of the output electrodes. When N_{out} becomes small or large, the output power and the efficiency decrease and current concentration become remarkable. On the other hand, when N_{out} is chosen suitablly, high output power and efficiency can be obtained, and current concentration is weakened.

CHAPTER 6

QUASI-TWO-DIMENSIONAL ANALYSIS OF LINEARLY-DIVERGING GENERATOR CONSIDERING BOUNDARY LAYER

6.1 Introduction

Up to now, whole electrical and gasdynamical performances of MHD generators have been discussed by the conventional quasi-one-dimensional analysis. Therefore, as introduced in the preceding chapter, the author has derived a quasi-two-dimensional theory for analysing the whole performances of the diagonal type generator with no boundary layer.

In this chapter, first, an improved quasi-two-dimensional theory is proposed for evaluating the whole performances of the single-load diagonal type generator in which turbulent velocity and thermal boundary layers are assumed to occur. Distributions of the electrical quantities in the duct are obtained two-dimensionally by the ECM as well as in the preceding chapter. On the other hand, distributions of the gasdynamical quantities in the core flow region are calculated by a similar modified quasi-one-dimensional theory to the one for the gasdynamical quantities in the whole duct, and those in the boundary layer are calculated separately from the core flow region by using the momentum integral equation and the 1/7th power profiles for the gas temperature and velocity.

Next, much numerical calculations are carried out for a large scale linearly-diverging diagonal type generator with the thermal input of about 2,000 MW driven by combustion gas of heavy oil. Influences of the length, wall temperature, diverging angle of the duct, the diagonal angle, the load current, etc. on performance characteristics of the single-load generator are investigated in detail.

Furthermore, the characteristics of the multiple-load generator are examined and compared with the ones of the single-load generator.

6.2 Quasi-Two-Dimensional Theory Considering Boundary Layer

6.2.1 Two-dimensional analysis of electrical quantities

The electrode arrangement and the applied magnetic flux distribution of the generator are the same as those shown in Fig. 5.1 and subsection 5.2.1. The electrical characteristics of the generator can be evaluated enough accurately by the equivalent network of the same form as in Fig. 5.2, in which the central three horizontal layers correspond to the core flow and the uppermost and lowest layers to the boundary ones, where for large δ such as $\delta/H > 0.1$ one boundary layer must be divided horizontally into two or three ones to keep accuracy of numerical calculation.

6.2.2 Quasi-two-dimensional analysis of gasdynamical quantities

Gas temperatures, velocities, etc. in the core flow and in the boundary layer are calculated separately in different methods.

First, it is assumed that the gasdynamical quantities in the core flow are governed by the following modified quasi-one-dimensional MHD equations

$$\rho u A^* = m_0 \ , \tag{6.1}$$

$$\rho u \, du/dx + dp/dx = \langle J_y \rangle_c B \quad , \tag{6.2}$$

$$\rho u \, d(h + u^2/2)/dx = -\langle P_o \rangle_c \quad , \tag{6.3}$$

and the state equation

$$p = \rho R T \quad , \tag{6.4}$$

where $\langle J_y \rangle_c$ and $\langle P_o \rangle_c$ are the average values of J_y and P_o, respectively, in the y-direction within a small interval (x, x+Δx) of the core flow. Those are given by

$$\langle J_y \rangle_c = \sum_i J_{yi} \Delta v_i \; / \sum_i \Delta v_i \quad , \tag{6.5}$$

$$\langle P_o \rangle_c = \sum_i P_{oi} \Delta v_i \; / \sum_i \Delta v_i \quad , \tag{6.6}$$

in which Δv_i is the volume of the space element i which exists in the above interval. In Eq. (6.1), also,

$$A^* = A - 2 \delta^* D, \tag{6.7}$$

where

$$\delta^* = \int_0^{\delta} \left(1 - \frac{\rho_b u_b}{\rho u} \right) dy, \tag{6.8}$$

in which δ^* and ρ_b are the displacement thickness and the mass density in the boundary layer, respectively.

Next, in the boundary layer, provided that the gas flow is turbulent, from the mass continuity and the momentum equations, the momentum integral equation for the momentum thickness θ is derived as follows [71, 72]:

$$\frac{d\theta}{dx} = \frac{c_f}{2} \quad , \tag{6.9}$$

where

$$\theta = \int_0^{\delta} \frac{\rho_b u_b}{\rho u} \left(1 - \frac{u_b}{u} \right) dy \quad , \tag{6.10}$$

in which the electromagnetic force in the boundary layer and the variations of u_b and ρ_b in the x-direction are ignored, and c_f is the skin friction factor which is given by

$$\left.\begin{aligned} c_f &= [\ 2.87 + 1.58 \log \{ (1+x) / k_s \}\ ]^{-2.5} \\ &\quad \times \{ 1 + r\,(\gamma - 1)\, M^2/2 \}^{-1} \quad , \\ &\text{where} \\ r &= \sqrt[3]{P_r} \quad , \end{aligned}\right\} \tag{6.11}$$

for the compressible turbulent flow on a rough plate, or by

$$c_f = 0.0592\ R_e^{-0.2} \quad , \tag{6.12}$$

for the same flow on a smooth plate [73]. In these equations, k_s, r, γ, M, P_r, and R_e are the equivalent sand roughness, the recovery factor, the specific heat ratio, the Mach number, the Prandtle number, and the Reynolds one, respectively. Furthermore, distributions of gas velocity and temperature in the boundary layer are assumed to be given by Eqs. (3.7) and (3.8), respectively, and the gas pressure in the layer is assumed to be equal to that in the core flow.

Additionally, in this chapter, as one of estimation functions of the generator, the isentropic efficiency η_i is used, which gives a measure of the amount by which the real prosess departs from a isentropic process. And η_i is defined by

$$\eta_i = \frac{h_{s0} - h_{s1}}{h_{s0} - h'_{s1}} \quad , \tag{6.13}$$

where h_{s0} is the stagnation or total enthalpy at the duct inlet, and h_{s1} and h'_{s1}* are the ones at the exit in the actual and the isentropic processes, respectively, in which h_{s0} and h_{s1} are calculated by Eq. (5.13).

6.3 Numerical Conditions

The working gas employed in calculation is the combustion gas of heavy oil fuel as previously described. The numerical conditions for calculation are listed in Table 6.1, where Q_{fu}, Q_{co}, and T_{pr} are the reaction heat of fuel, the sum of Q_{fu} and the heat input by preheated air or the tatal heat in the combustor, and the temperature of the air, respectively, H_0, D_0, and M_0 the duct height, width, and the Mach

Table 6.1 Numerical conditions used in calculation.

Q_{fu}	(MW)	2085	x_{t1}	(m)	1.5
T_{pr}	(K)	1500	x_{t2}	(m)	8.5 , 10.5 , 11.5
Q_{co}	(MW)	2843	$x_{B1} = L - x_{B2}$	(m)	1.5
m_0	(kg/s)	674	g	(T/m)	2.5
$H_0 \times D_0$	(m)	1.04 × 1.04	I_L	($\times 10^4$A)	3 to 5
L	(m)	12, 14, 16	p_0	(atm)	5.85
θ_0	(°)	7 to 16	T_0	(K)	2721
L_N	(m)	1.0	T_w	(K)	1500 to 2100
L_D	(m)	2.9 to 4.5	u_0	(m/s)	853
φ_0	(°)	25 to 45	M_0	(Mach)	0.9
N		100	B_0	(T)	6
N_o		8	$R_w = R'_w$	(Ω)	10^4

* See Appendix II.

number, respectively, at the inlet, θ_0 the diverging angle of the duct.

In the table, also, it is assumed that $x_{t1} = 8.5$, 10.5, and 11.5 m for $L = 12$, 14, and 16m, respectively. In this connection, L_D and x_{t2} are determined so that the following relations

$$L_D = H_1 \quad , \tag{6.14}$$

$$L - x_{t2} > (H_1/2) \cot \varphi_0 \ , \tag{6.15}$$

are kept, where H_1 is the duct height at the exit. Next, p_0, T_0, and u_0 are chosen so that $M_0 = 0.9$ is kept under the condition of the stagnation pressure $p_{s0} = 9$atm in the combustor. Also, $k_s = 4\times10^{-4}$ and $P_r = 1$ are assumed [50].

6.4 Performance Characteristics of Single-Load Generator

6.4.1 Influence of duct length

In Table 6.2, there are listed calculation results of the output power P, the isentropic efficiency η_i, and the pressure p_1, temperature T_1, velocity u_1 and Mach number M_1 of the gas at the exit of the

Table 6.2 Influence of L on whole generator characteristics ($\theta_0 = 8.8°$, $\varphi_0 = 30°$, $I_L = 4\times10^4$A, $T_W = 1800$K).

L (m)	12	14	16
P (P') (MW)	467 (557)	514 (602)	556 (626)
η_i (η_i') (%)	55.7 (59.6)	57.8 (61.3)	59.1 (61.6)
p_1 (p_1') (atm)	1.55 (1.20)	1.39 (1.10)	1.22 (1.03)
T_1 (T_1') (K)	2454 (2398)	2424 (2377)	2392 (2366)
u_1 (u_1') (m/s)	376 (468)	336 (411)	315 (365)
M_1 (M_1') (Mach)	0.417 (0.526)	0.375 (0.464)	0.354 (0.412)

generator duct with rough wall surface for L = 12, 14, and 16m, where $\theta_0 = 8.8°$, $\varphi_0 = 30°$, $I_L = 4\times10^4$A, $T_w = 1800$K, and $L_D = 2.9$, 3.2, and 3.5m, respectively, for L = 12, 14, and 16m. In the table, for comparison, the values of the same ones P', η_i', p_1', T_1', u_1', and M_1' obtained by the quasi-one-dimensional theory are also shown in round brackets.

The table shows that P and η_i increase but inversely p_1, T_1, and u_1 decrease as L increses. Since the working gas plasma in rear end region of x > 12m has yet ability to generate fair electric power, P and η_i increase when L becomes large and the domain where the applied magnetic flux density is constant is extended.

Next, from Table 6.2, we see that P' shows 10 to 20% larger values compared to P. We also get P/P' = 0.838, 0.854, and 0.882 for L = 12, 14, and 16m, respectively, and the ratio seems to depend only a little on L. Also η_i' is 2 to 4% larger than η_i.

In this connection, what should be emphasized here is that the diverging generator can produce much more output power than the constant cross-section one which is discussed in the preceding chapter. In the constant cross-section generator, choking phenomenon is apt to occur when the gas velocity u_0 at the duct inlet is large. Accordingly, u_0 must be taken fairly low, and so the gas velocity in the central part is not so large on the average. Then the output power is small, because it is proportional to u^2. On the other hand, since in the diverging generator u_0 can be taken large, a large amount of the output power can be extracted from it.

Next, Figure 6.1 shows the distributions of $\langle -J_y \rangle$, $-J_y'$, $\langle P_o \rangle$, and P_o' along the x-axis, and those of p, p', T, T', u, and u' in the case of L = 16m in Table 6.2. The figure tells that the distributions of the electrical and gasdynamical quantities in the duct inlet and exit by both the quasi-two and the quasi-one-dimensional theories fairly differ each other.

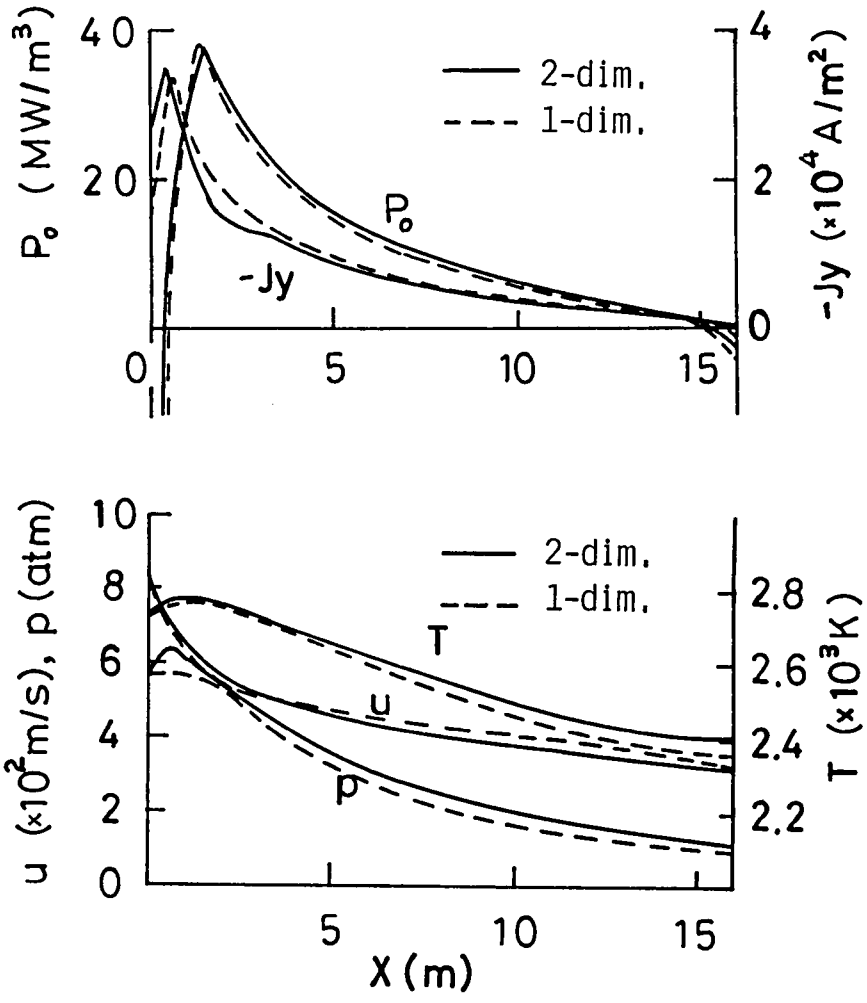

Fig. 6.1 Distributions of <-Jy>, -Jy', <P_o>, and P_o' along the x-axis, and those of p, p', T, T', u, and u' (L = 16m, θ_0 = 8.8°, L_D = 3.5m, φ_0 = 30°, x_{t2} = 11.5m, Tw = 1800K).

6.4.2 Influence of duct wall temperature

Figure 6.2(a) shows the influence of Tw on P and η_i, where L = 16m, $\theta_0 = 8.8°$, $\varphi_0 = 30°$, and $I_L = 4\times10^4$A. The figure shows that P and η_i decrease with Tw, and the generator with the smooth wall surface gives larger P and η_i than that with the rough one, because the boundary layer occuring near the rough wall surface becomes considerably thicker than that near the smooth one.

Figure 6.2(b) presents the variations of p_1, T_1, and u_1 by Tw. Since the values of p_0, T_0, and u_0 have been already given in Table 6.1, we can roughly image the distributions of p, T, and u along the gas flow. In both generators with the rough and smooth wall surfaces, p_1 and T_1 increase but u_1 decreases as Tw lowers. Since the conductivity σ is heightened by high T_1 but u_1 decreases with Tw, it is supposed that P which is proportional to σu^2 lowers with Tw.

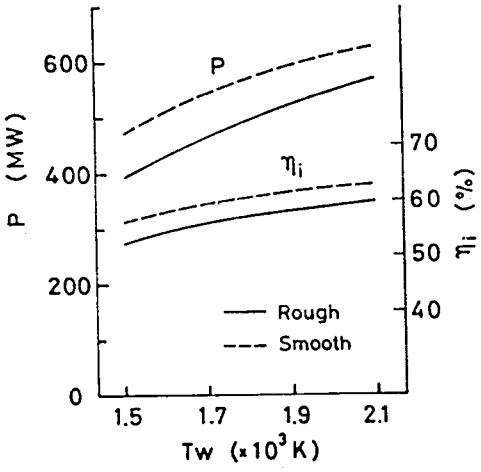

(a) P and η_i.

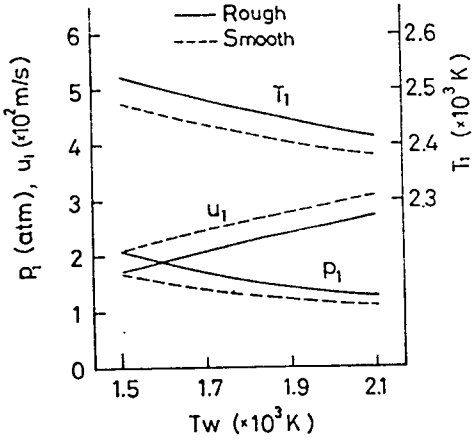

(b) p_1, T_1, and u_1.

Fig. 6.2 Influence of Tw on P, η_i, p_1, T_1, and u_1 (L = 16m, $\theta_0 = 8.8°$, $L_D = 3.5$m, $\varphi_0 = 30°$, $x_{t2} = 11.5$m).

6.4.3 Influence of diverging angle of duct

In Figs. 6.3(a), (b), and (c), there are shown the variations of P, η_i, and stagnation pressure p_{s1} at the exit by θ_0, H_1 , and I_L in the cases of $\varphi_0 = 25°$, 30°, and 45°, respectively, where L = 16m, $L_D = H_1$, $x_{t2} = 11.5$m, Tw = 1800K, and the duct wall surface is assumed rough. The figures tell that θ_0 has large influence on P and p_{s1}, viz. P increases largely and p_{s1} fairly decreases as θ_0 becomes small. On the other hand, η_i little depends on θ_0.

Next, let us pay attention that all the curves are interrupted at some values of θ_0 on the way of its decrease. This is resulted from the fact that numerical solutions can not be obtained for θ_0 below the above values because of choking phenomenon occurring in the duct. Further, the lower limit of θ_0 which gives the numerical solutions becomes high with φ_0. As the result, it is seen that by using a small θ_0 within the range where the choking phenomenon does not occur, we shall be able to design a generator of high performances which gives large output power, high isentropic efficiency, and low stagnation pressure at the exit.

6.4.4 Influences of diagonal angle and load current

Figures 6.3(a), (b), and (c) show that P < 500 MW for $\varphi_0 = 25°$, but it increases with φ_0, and P ≧ 550 MW is attained for $\varphi_0 = 30°$ and 45° with some suitable values of θ_0 and I_L. Also, η_i nearly reaches 60% for $\varphi_0 = 25°$ and 30°, but it decreases slightly as φ_0 increases and $\eta_i = 56\%$ at most for $\varphi_0 = 45°$.

Further, $P_{s1} > 2$atm for $\varphi_0 = 25°$, but it decreases as φ_0 increases, and $p_{s1} = 1.3$ and 1.0atm for $\varphi_0 = 30°$ and 45°, respectively. Practically, p_{s1} must be a little higher than the atmospheric pressure to exhause the working gas into the air.

When we assume $p_{s1} = 1.3$atm, the relations of P, η_i, and θ_0 to φ_0 plotted in Fig. 6.4 are obtained from Figs. 6.3(a) to (c). From

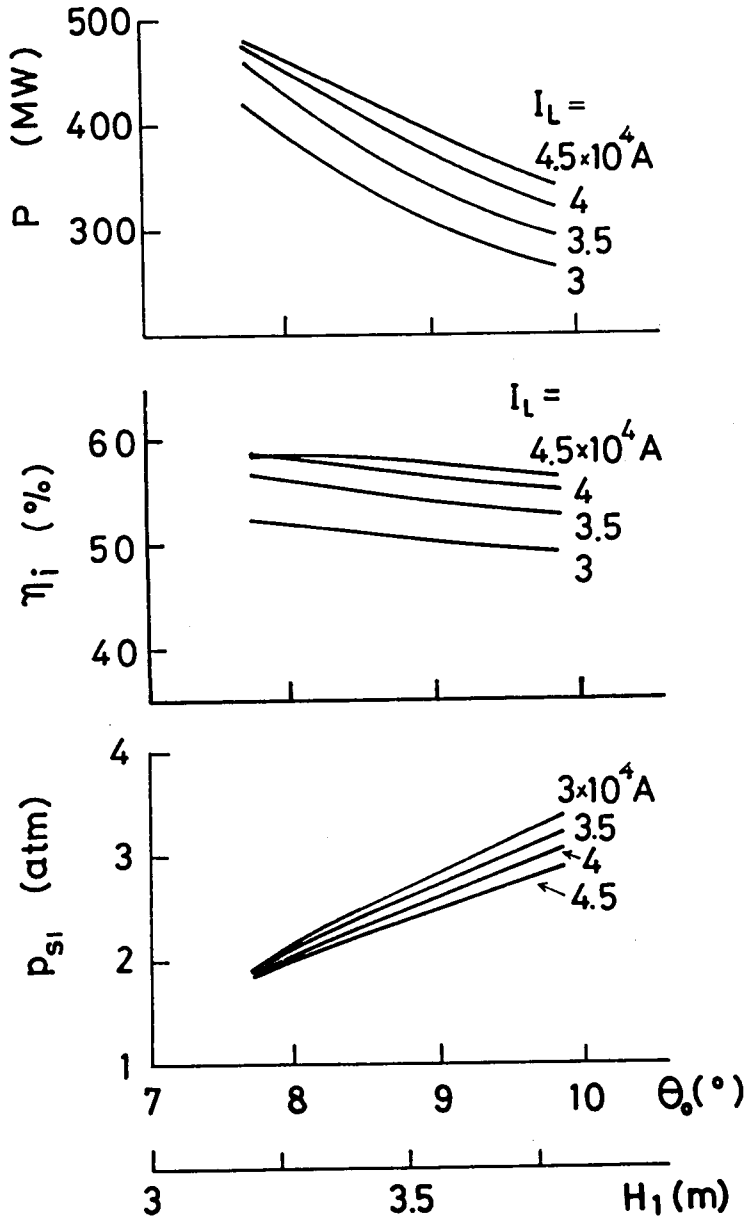

Fig. 6.3 (a) Variations of P, η_i, and p_{s1} by θ_0, H_1, and I_L when $\varphi_0 = 25°$ (L = 16m, x_{t2} = 11.5m, Tw = 1800K).

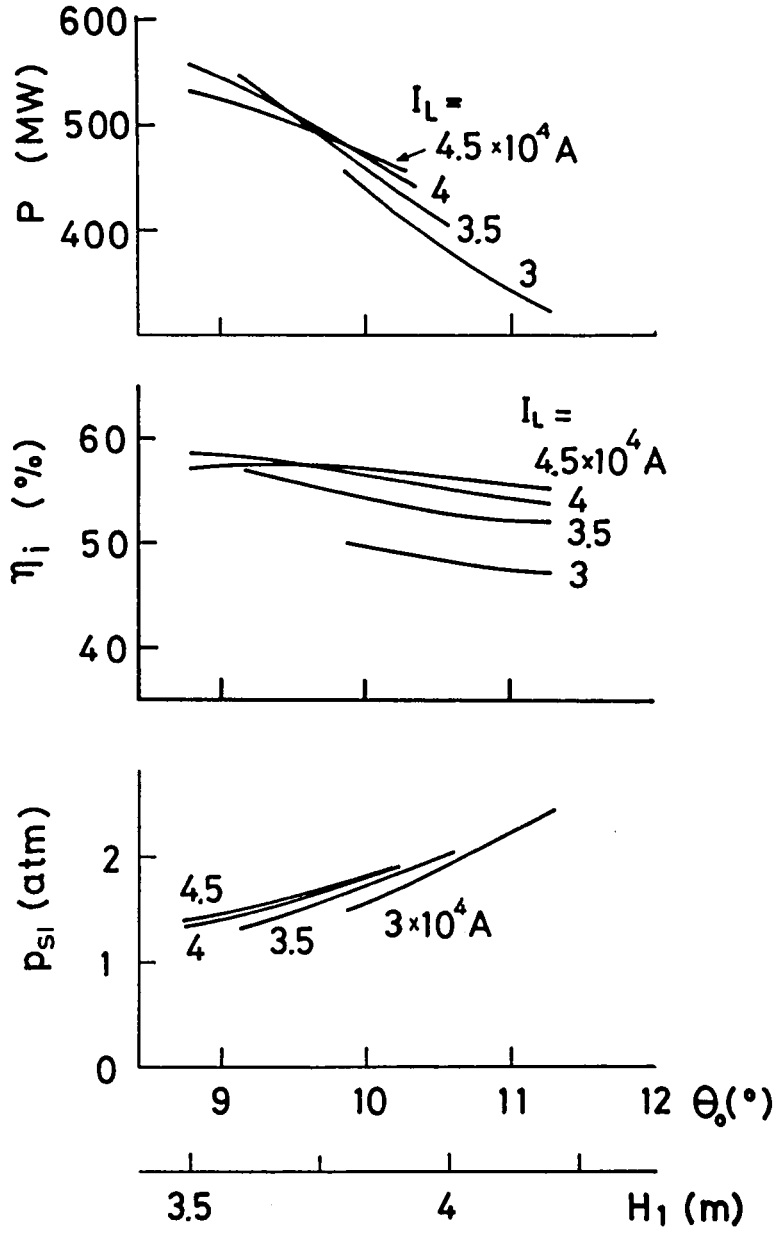

Fig. 6.3 (b) Variations of P, η_i, and p_{s1} by θ_0, H_1, and I_L when $\varphi_0 = 30°$ (L = 16m, x_{t2} = 11.5m, Tw = 1800K).

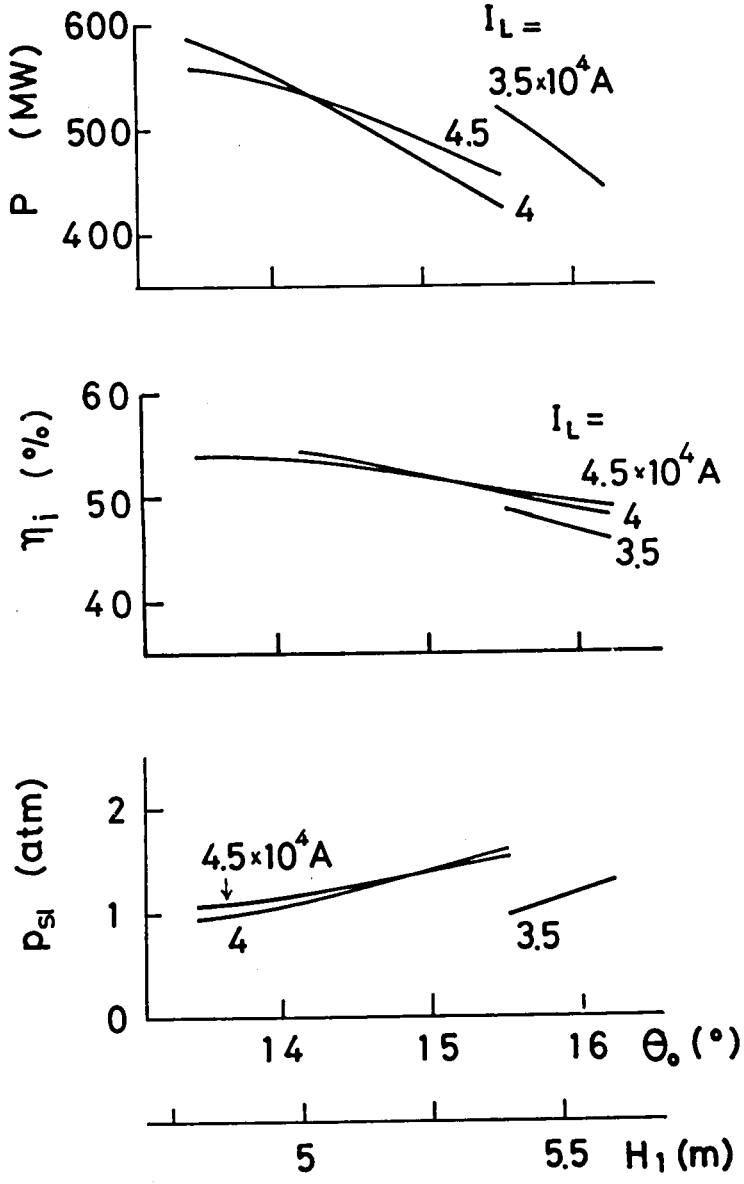

Fig. 6.3 (c) Variations of P, η_i, and p_{sl} by θ_0, H_1, and I_L when $\varphi_0 = 45°$ (L = 16m, x_{t2} = 11.5m, Tw = 1800K).

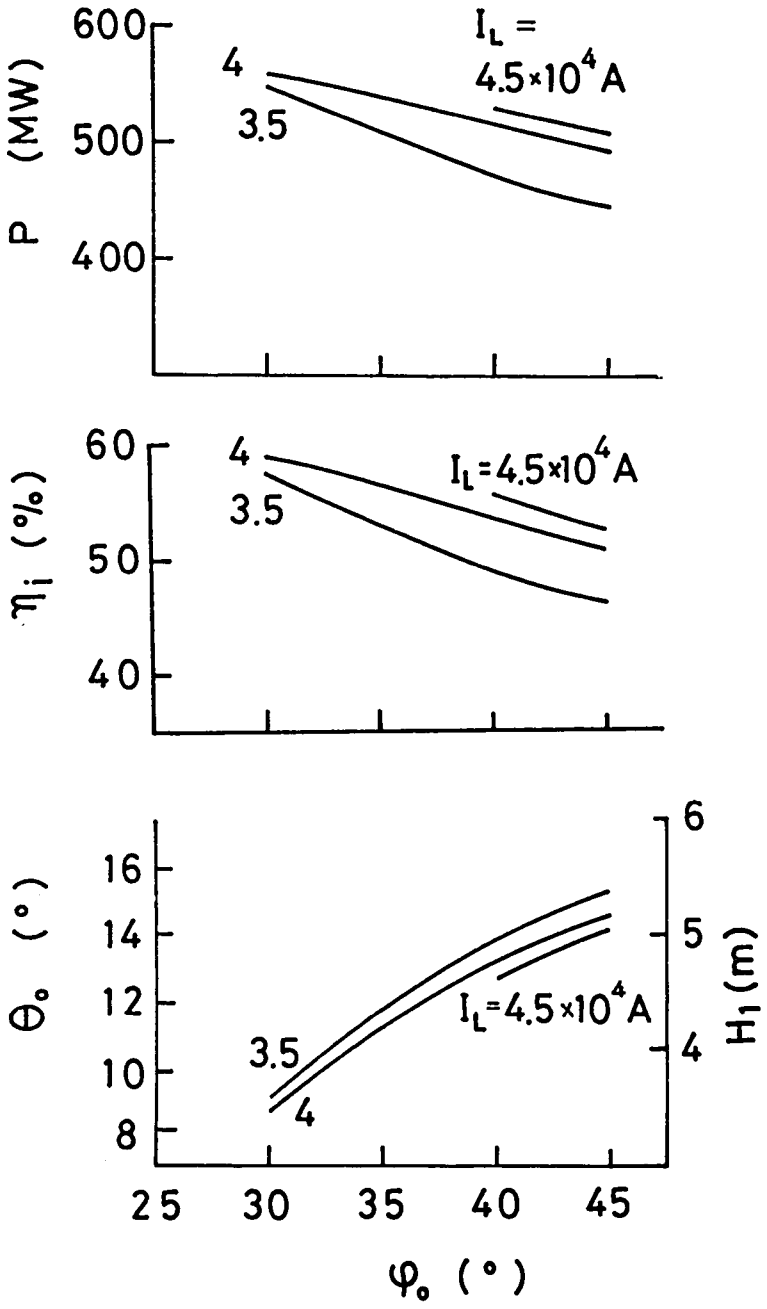

Fig. 6.4 Relations of P, η_i, and θ_0 to φ_0 (L = 16m, x_{t2} = 11.5m, T_W = 1800K).

Fig. 6.4, it is seen that in $30° < \varphi_0 < 45°$ P and η_i gradually increase and inversely θ_0 fairly decreases with φ_0. This represents that by some small value of φ_0 we can make P and η_i high and θ_0 small i.e. H_1 low. This is very useful to save the amount of superconductive material which strongly influences the construction cost of the generator. Also it is known that, when $\varphi_0 = 25°$, H_1 becomes low, but p_{s1} does not lower near the atmospheric pressure and P is not so large. From the above-mentioned, the optimum value of φ_0 is about 30° which makes the generator characteristics almost best under the numerical conditions assumed in this chapter. Also the similar examination of Figs. 6.3 and 6.4 to the above one shows that the optimum value of I_L is 4×10^4A.

In Figs. 6.1(a) and (b), there have been already shown the distributions of the electrical and gasdynamical quantities, respectively, along the x-axis, for $\varphi_0 = 30°$ and $I_L = 4\times10^4$A. Further, Figs. 6.5(a) and (b) show the distribution of the current density vectors in the duct inlet and exit regions, respectively, under the same conditions as in Fig. 6.1. In Figs. 6.5(a) and (b), the maximum current densities 13×10^4 and 3×10^4A/m^2 appear at the down stream ends of the output electrodes 8' and 100', respectively.

6.5 Performance Characteristics of Multiple-Load Generator

6.5.1 Multiple-load generator

As shown in subsection 3.4.6, we can expect that the diagonal type generator give the high output power and electrical efficiency compared favorably with those of the Faraday one when we use some suitable diagonal angle and load factor for a given Hall parameter. In principle, the diagonal type generator can be operated with single load. However, since β varies largely from the inlet to the exit in a practical duct, it will be difficult to give the suitable distri-

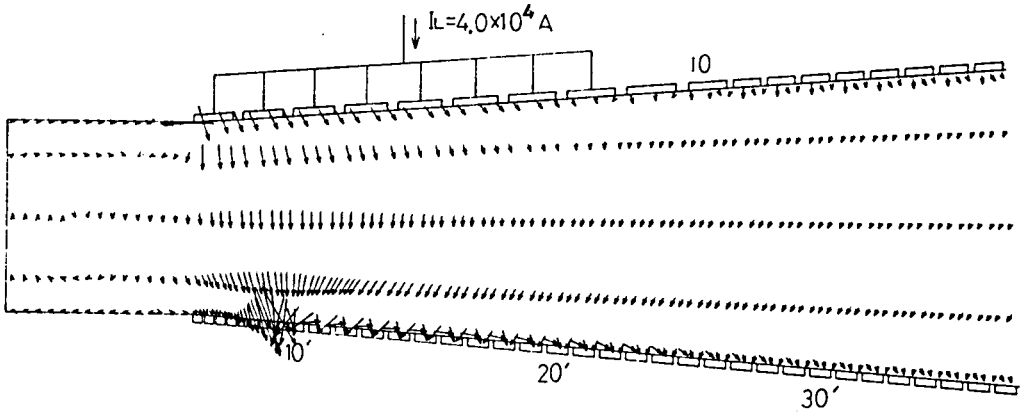

(a) Inlet region.

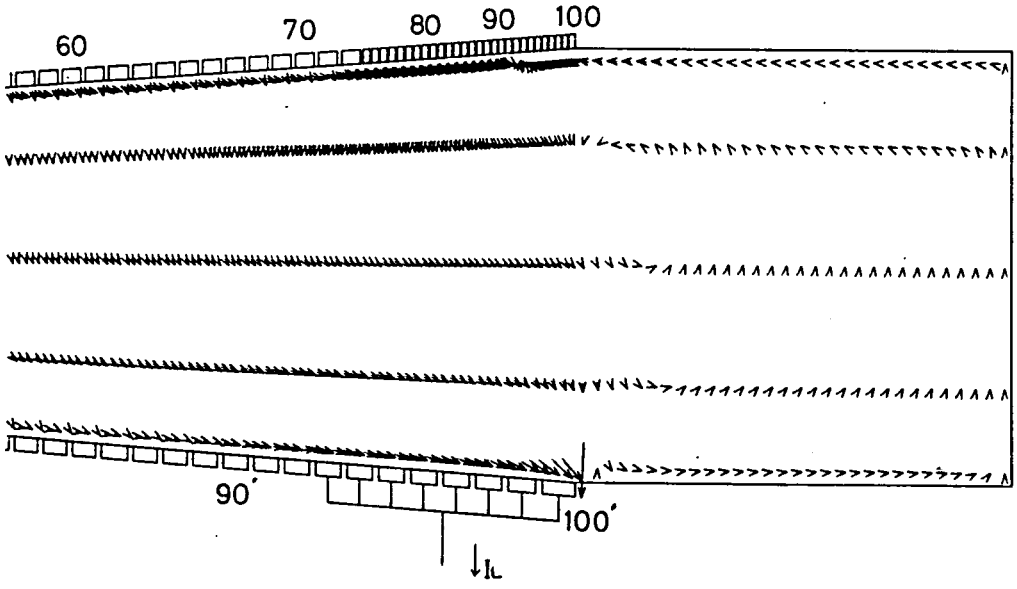

(b) Exit region.

Fig. 6.5 Distribution of current density vectors in the inlet and exit regions ($L = 16m$, $\theta_0 = 8.8°$, $L_D = 3.5m$, $\varphi_0 = 30°$, $x_{t2} = 11.5m$, $Tw = 1800K$).

bution of load factor throughout the whole duct by the single load and to highten the whole performance of the generator more than in the preceding section.

Hence, let us take up a multiple (n-ple) load generator [69, 70] as shown in Fig. 6.6, where I_{L1}, I_{L2}, ..., and I_{Ln} are load currents flowing in the load resistances R_{L1}, R_{L2}, ..., and R_{Ln}, respectively, $N_{Li} = N'_{Li}$ $(i = 0, 1, 2, \ldots, n)$ is a number of the first electrode of the i-th output electrode pairs, and N_{oi} the number of the pairs. If the value of load factor with respect to each load can be appropriately determined, the whole performances of the generator may be expected to be made better than those of the single-load one.

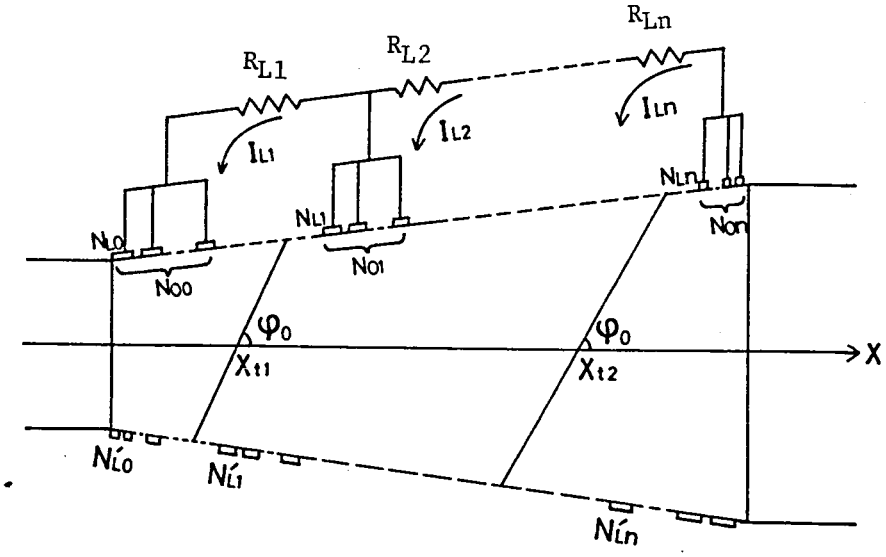

Fig. 6.6 Schematic diagram of multiple-load diagonal type generator.

Next, the electrical and gasdynamical performances of the multiple-load generator can be analysed by the essentially same theory as that of the single-load one which was described in chapter 2, where the number of unknown currents in the equivalent network increases only a few in the multiple-load generator.

6.5.2 Performance characteristics

Figure 6.7 shows the relations of P and η_i to I_{L1} and I_{L2} of a double-load (n = 2) generator, where we employ L = 16m, $\theta_0 = 9.5°$, L_D = 3.8m, $\varphi_0 = 30°$, $x_{t2} = 11.5$m, and Tw = 1800K in Table 6.1. In the figure, the characteristics curves of the single-load (n = 1) generator under the same conditions as the above ones are also plotted for comparison. From the figure, it will be seen that P increases with I_{L1} but inversely decreses as I_{L2} increases, and the output power of the double-load generator can become considerably larger than that of the single-load one.

On the other hand, η_i increases with I_{L1}, but has a peak value with respect to I_{L2}. The isentropic efficiency of the double-load generator can become also higher than that of the single-load one. In this connection, when $I_{L1} \geqq 5\times10^4$A, numerical solutions are not obtained because of occurrence of choking phenomenon.

Figure 6.8 shows the relations of P and η_i to N_{L1} and N_{L2} of a triple-load (n = 3) generator with the same ones of the double-load generator, which have been calculated under the same conditions as in Fig. 6.7, where $I_{L1} = 5\times10^4$A, $I_{L2} = 4\times10^4$A, and $I_{L3} = 3\times10^4$A. The characteristics of the former are better than those of the latter.

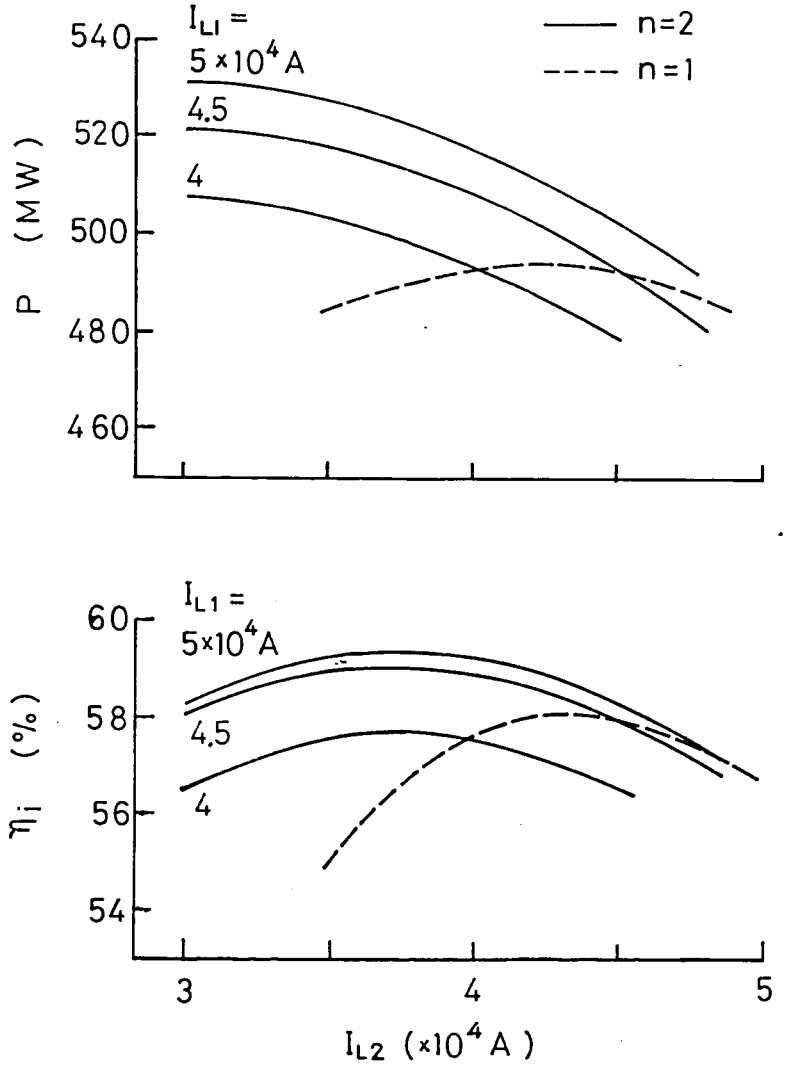

Fig. 6.7 Relations of P and η_i to I_{L1} and I_{L2} of a double-load generator (L = 16m, θ_0 = 9.5°, L_D = 3.8m, φ_0 = 30°, x_{t2} = 11.5m, Tw = 1800K, N_{L1} = 60, N_{o1} = 3).

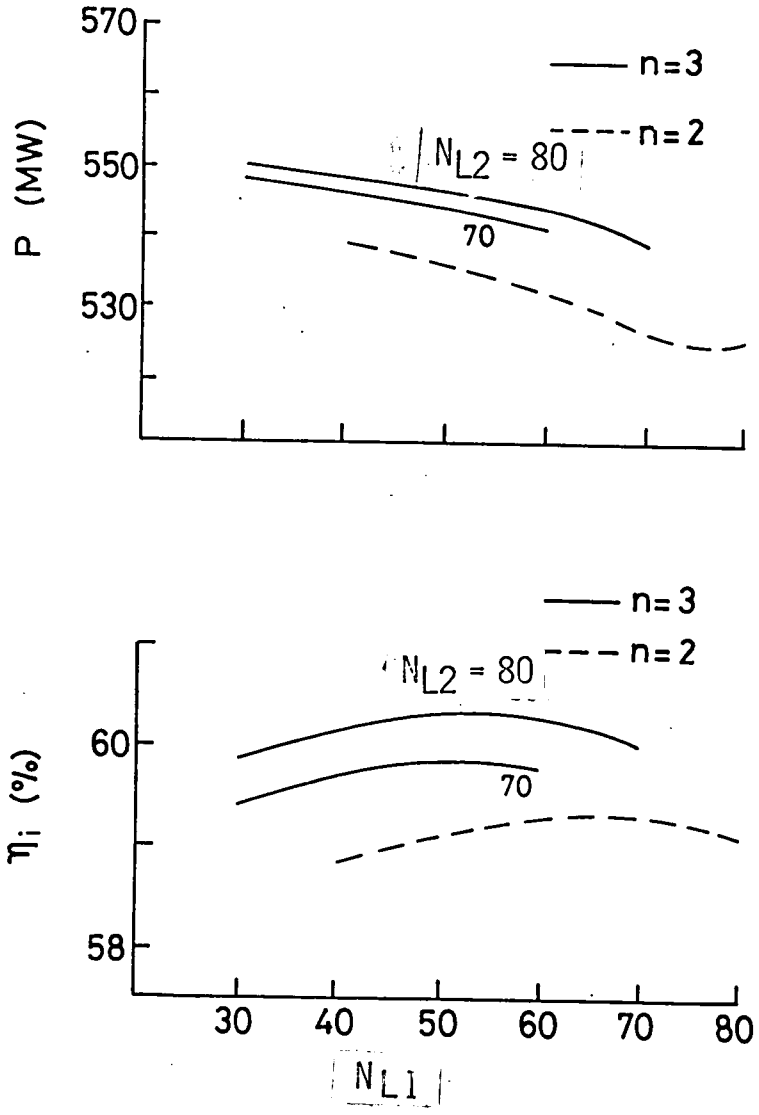

Fig. 6.8 Relations of P and η_i to N_{L1} and N_{L2} of a triple-load generator (L = 16m, $\theta_0 = 9.5°$, $L_D = 3.8$m, $\varphi_0 = 30°$, x_{t2} = 11.5m, Tw = 1800K, $I_{L1}=5\times10^4$A, $I_{L2} = 4\times10^4$A, $I_{L3} = 3\times10^4$A).

6.6 Concluding Remarks

The main results obtained in this chapter are as follows:

(1) An improved quasi-two-dimensional theory was proposed to evaluate the whole electrical and gasdynamical quantities of the diagonal type generator in which turbulent boundary layer occurs.

(2) The generator output obtained by the quasi-one-dimensional calculation shows 10 to 20% larger values compared with the results of the quasi-two-dimensional calculation. And the distributions of the electrical and gasdynamical quantities in the duct inlet and exit regions gotten by the former fairly differ from the ones by the latter.

(3) When the duct length becomes long and the range where the applied magnetic flux density is constant is extended, the output power and isentropic efficency increase.

(4) The output power and efficiency decrease with the duct wall temperature, and those are smaller when the duct wall surface is assumed rough than when it is assumed smooth.

(5) When the diverging angle of the duct is too small, choking phenomenon is apt to occur. However, when small value of the diverging angle is selected suitablly, large output power and high efficiency are obtained.

(6) The diagonal angle and load current have fairly great influences on the generator performances, which are almost best when the former and the latter are about 30° and 4×10^{4}A, respectively, under the numerical conditions in this chapter.

(7) The multiple-load generator can give considerably larger output power and efficiency than the single-load one by suitablly sharing the load current with several loads.

REFERENCES

[1] Oshima, K.: "Latest International Situation and Future Energy Development of Our Country," Trans. I.E.E.J. Vol. 99, No. 9, pp, 797-802, (1972).

[2] Esaki, K.: "New Energy, Part 1," Trans. I.E.E.J. Vol. 94, No. 10, pp. 872-879, (1974).

[3] Momota, T.: "New Energy, Part 2," ibid., Vol. 94, No. 12, pp. 1095-1102, (1974).

[4] Kubota, K.: "New Energy, Part 3," ibid., Vol. 95, No. 1, pp. 9-16, (1975).

[5] Nomura, S.: "Nuclear Generation," Nuclear Eng. Vol. 24, No. 5, pp. 38-44, (1978).

[6] Joint NEA/IAEA International Liaison Group: "MHD Electric Power Generation," 1976 Status Report, (1977).

[7] Rosa, R. J.: "An Experimental Magnetohydrodynamic Power Generator," J. Appl. Phys., 31, pp. 735-736, (1960).

[8] Barshak, A. E., V. A. Bityurin, A. E. Buznikov, A. V. Karpukhin, V. I. Kovbasiuk, V. I. Maksimenko, S. A. Medin, and S. I. Pishchikov: "Diagonal Frame RM Channel of The U-25 Power Plant," 17th Symp. Eng. Aspects MHD, F.2, (1978).

[9] Petty, S., A. Solbes, G. Enos, and A. Dunton: "Progress on The Mark VI Long-Duration MHD Generator," 15th Symp. Eng. Aspects MHD, IV.5, (1976).

[10] Wu, Y. C. L., J. B. Dicks, K. E. Tempelmeyer, L. W. Crawford, I. W. Muehlhauser, and G. Rajagopal: "Experimental and Theoretical Investigation on a Direct Coal Fired MHD Generator," 6th Int. Conf. on MHD Elect. Power Gen., Vol. I, pp. 199-214, (1975).

[11] Wu, Y. C. L., J. B. Dicks, J. W. Muehlhauser, M. H. Scott, G. Kroeger, and Tran My: "Experimantal Investigation on a Direct

Coal-Fired MHD Generator," 15th Symp. Eng. Aspects MHD, IV.6, (1976).

[12] Enos, G., J. Morenski, S. Petty and A. Solbes: "Design Description and Performance Predictions for The First CDIF Power Train," 18th Symp. Eng. Aspects MHD, A.1, (1979).

[13] Fushimi, K., et al. (ETL Mark V Research Group): "Experiment on MHD Generator with a Large-Scale Superconducting Magnet (ETL Mark V)," 14th Symp. Eng. Aspects MHD, I.4, (1974).

[14] Mori, Y., T. Homma, S. Korenaga, K. Onda and K. Takano: "Recent Experimental Results of ETL Mark VI," 6th Int. Conf. on MHD Elect. Power Gen., Vol. I, pp. 155-166, (1975).

[15] Ikeda, S., T. Masuda, Y. Kusaka and T. Honda: "Experiment on MHD Generator with a Large-Scale Superconducting Magnet (ETL Mark V)," 15th Symp. Eng. Aspects MHD, IV.4, (1976).

[16] Kusaka, Y., T. Masuda, S. Ikeda, and T. Honda: "Experiment on MHD Generator with a Large Scale Super Conducting Magnet (ETL Mark V)," 16th Symp. Eng. Aspects MHD, I.1, (1977).

[17] Kerrebrock, J.L.: "Conduction in Gases with Elevated Electron Temperature," Proc. Second Symp. Eng. Aspects MHD, Columbia Univ. Press, New York, pp. 327-346, (1962).

[18] Nakamura, T. and W. Riedmuller: "Investigation of Nonequilibrium MHD Plasma under the Conditions of Fully Ionized Seed," 5th Int. Conf. on MHD Elect. Power Gen., Vol. II, pp.291-302, (1971).

[19] Yoshikawa, K. and I. Michiyoshi: "Ionization Instability and Stable Region in Potassium Seeded Argon Gas Plasma MHD Generation," Plasma Physics, 16, pp. 1085-1099, (1974).

[20] Ishikawa, M., J. Umoto, and T. Hara: "Two Dimensional Analysis of a Diagonal Type Nonequilibrium Plasma MHD Generator," Trans. I.E.E.J., Vol. 96-A, No. 12, pp. 559-566, (1976).

[21] Tanaka, D. and Y. Hattori: "Stable Operating Points of Non-equilibrium MHD Generator under the Conditions of Fully Ionized

Seed," Bulletin of the Institute of Atomic Energy, Kyoto Univ., 54, p. 24, (1978).

[22] Sheindlin, A. E., Barshak, V. A., Bityurin, V. I., Kovbasiuk, V. I., Maksimenko, S. A., Medin, D. S., Pinkhsik, S. I., Pishchikov, and S. A. Pashkov: "Investigation of Diagonal-Conducting Wall Channel for U-25 Power Plant," 15th Symp. Eng. Aspects MHD, IV.1, (1976).

[23] Rosa, R. J., S. W. Petty, and G. R. Enos: "Long Duration Testing in the Mark VI Facility," 14th Symp. Eng. Aspects MHD, I.5, (1974).

[24] Petty, S., R. Rosa, and G. Enos: "Developments with the Mark VI Long Duration MHD Generator," 6th Int. Conf. on MHD Elect. Power Gen., Vol. I, pp. 231-250, (1975).

[25] Wu, Y. C. L., J. B. Dicks, L. W. Crawford, J. W. muehlhuser, M. A. Scott, and N. Sood: "Theoretical and Experimental Studies of Magnetohydrodynamic Power Generation with Char," 12th Symp. Eng. Aspects MHD, II.1, (1972).

[26] Wu, Y. C. L., J. B. Dicks, L. W. Crawford, R. V. Shanklin, W. D. Jackson, J. W. Muehlhauser, J. F. Martin, G. Rajagopal, and G. D. Roy: "Investigation of Diagonal Conducting Wall Generator," 13th Symp. Eng. Aspects MHD, II.5, (1973).

[27] Wu, Y. C. L., J. B. Dicks, K. E. Tempelmeyer, L. W. Crawford, J. W. Muehlhauser, J. F. Martin, G. Roy and G. Rajagopal: "On Direct Coal Fired MHD Generator," 14th Symp. Eng. Aspects MHD, I.2, (1974).

[28] Muehlhauser, J. W., Tran My, M. H. Scott, Y. C. L. Wu, and J. B. Dicks: "Experimental Investigation of Multipleload Diagonal Conducting Wall Generators," 16th Symp. Eng. Aspects MHD, I.3, (1977).

[29] Kirillin, V. A., A. E. Sheindlin, A. V. Karpukhin, V. I. Maksimenko, S. A. Pashkov, D. S. Pinkhasik, N. P. Prvaloy, V. D. Semenov, U. S. Sidorov, Yu. D. Sokirko, Yu. N. Sololov, E. M.

Shelkov, R. V. Shanklin, A. L. Liccardi, G.Rudins, W. D. Jackson, E. Levi, M. Petrick, R. Niemann, B. Wang, R. P. Smith: "The U-25B Facility for Studies in Strong Magnetohydrodynamic Interaction," 17th Symp. Eng. Aspects MHD, F.1, (1978).

[30] Iserov, A. D., V. I. Maksimenko, G. I. Maslennikov, A. P. Nefedov, M. Ya. Panovko, D. S. Pinkhasik, V. D. Semenov, Yu. N. Sokolov, I. A. Vasilyeva, K. Tempelmeyer, T. Zinneman, M. Kraimer, E. Doss, C. Lenzo, W. Unkel, J. Louis, R. Rosa, and Y. Wu: "Study of the U-25B MHD Generator System in Strong Electric and Magnetic Fields," 18th Symp. Eng. Aspects MHD, A.5, (1979).

[31] Hurwitz, H., R. W. Kilb, and G. W. Sutton: "Influence of Tensor Conductivity on Current Distribution in a MHD Generator," J. Appl. Phy., Vol. 32, No. 2, pp. 205-216, (1961).

[32] Dzung, L. S.: "Favourable Configurations of Segmented Electrodes for MHD Generators," Brown Boveri Review, Vol. 53, No. 3, pp. 238-250, (1966).

[33] Demetriades, S. T., G. S. Argyropoulos, and C. D. Maxwell: "Scaling Parameters for the Electrical Performance of Open-Cycle MHD Generators," 13th Symp. Eng. Aspects MHD, II.4, (1973).

[34] Oliver, D. A.: "Inter-Electrode Breakdown on Electrode Walls Parallel and Inclined to the Magnetic Field," 6th Int. Conf. on MHD Elect. Power Gen., Vol. I, pp. 329-344, (1975).

[35] Hara, T. and J. Umoto: "A Finite Element Approach to Three-Dimensional Current Distributions in Diagonal Wall Channels," 17th Symp. Eng. Aspects MHD, B.5, (1978).

[36] Gruber, O. H.: "Electrical Equivalent Circuit of D.C. Magneto-plasmadynamic Converter," 4th Int. Conf. on MHD Elect. Power Gen., Vol. I, pp. 385-395, (1968).

[37] Ogiwara, H.: "The Voltage Distributions in the Channel of the Faraday-Type MHD Generator with the Segmented Electrodes,"

Trans. Inst. Elect. Engrs. Japan, Vol. 89-9. No. 972, pp. 1719-1726, (1969).

[38] Celinski, Z. N.: "Electrical Equivalent Circuits of D.C. MHD Generators," 3rd Int. Symp, on MHD Power Gen. Vol. I, pp. 323-331, (1966).

[39] Celinski, Z. N.: "Effects of Temperature and Velocity Profile in Faraday-Type MHD Generator," Energy Conversion, Vol. 10, pp. 105-112, Pergamon Press, (1970).

[40] Shirakata, H.: "Analysis of Electrical Characteristics of the Nonequilibrium MHD Generator by the Four-Terminal Network Theory," Jap. Journ. of Appl. Phys., Vol. 11, No. 12, pp. 1837-1850, (1972).

[41] Takano, K., K. Onda, and Y. Mori: "Calculation of Performances of Large Scale Diagonal MHD-Steam Plants," ibid., V.6.

[42] Sheindlin, A. E., B. Ya, Shumyatsky, V. I. Kovbasyuk, P. P. Ivanov, and G. M. Koryagina: "Optimization of Open Cycle Power Plant MHD Generator," 14th Symp. Eng. Aspects MHD, III.4, (1974).

[43] Yoshida, M. and J. Umoto: "Two Dimensional Analysis of Diagonal Type MHD Generator by Means of Equivalent Circuit (The First Report)," Convention Records at the Annual Meeting in Kansai District of I.E.E.J., No. G1-8, (1974).

[44] Yoshida, M. and J. Umoto: "Two Dimensional Analysis of Diagonal Type MHD Generator by Means of Equivalent Circuit (The Second Report)," Convention Records at the Annual Meeting of I.E.E.J., No. 828, (1975).

[45] Yoshida, M. and J. Umoto: "Two Dimensional Analysis of MHD Generator by Means of Equivalent Circuit," Mem. Facul. Eng. Kyoto Univ., Vol. 36, Part 4, April (1975).

[46] Rosa, R. J.: "Magnetohydrodynamic Energy Conversion," McGraw-Hill, New York, p. 74, (1968).

[47] Yoshida, M. and J. Umoto: "Two Dimensional Analysis of Diago-

nal Type MHD Generator by Means of Equivalent Circuit (The Third Report)," Convention Records at the Annual Meeting in Kansai District of I.E.E.J., No. G1-15, (1975).

[48] Technical Report of the Investigation Committee of MHD Generator Plant in Japan, (1973).

[49] Celinski, Z. N.: "Numerical Calculations of the Electrical Parameters in a Faraday-Type MHD Generator with Two-Dimensional Gas Flow," Arch. Electrot. Vol. XIX, No. 4, (1970).

[50] Schlichting, H.: "Boundary-Layer Theory," McGraw-Hill, New York, 6th Edition, p. 40, 312, (1968).

[51] Uchida, H., et al., "Advanced Lectures on Heat and Mass Transfer," Syo-ka-bou, p. 46, (1977).

[52] Ishikawa, M.:"Study on Performance Characteristics of Diagonal Type Nonequilibrium Plasma MHD Generator," Doctral Thesis, Chap. 2, Institute of Atomic Energy Kyoto Univ. Kyoto, Japan, (1978).

[53] Yoshida, M. and J. Umoto: "Two-Dimensional Analysis of Diagonal Type MHD Generator by Means of Equivalent Circuit," Trans. I.E.E.J. Vol. 97-A, No. 3, pp.117-124, (1977).

[54] Yoshida, M., and J. Umoto: "Two-Dimensional Analysis of Diagonal MHD Generator via Equivalent Circuit," Elect. Eng. Japan Vol. 97, No.2, pp. 1-7, (1977).

[55] Ishikawa, M.: "Study on Performance Characteristics of Diagonal Type Nonequilibrium Plasma MHD Generator," Doctral Thesis, Chap. 5, Institute of Atomic Energy Kyoto Univ. Kyoto, Japan, (1978).

[56] Yoshida, M. and J. Umoto: "Analysis of End Effects in Diagonal Type MHD Generator by Means of Equivalent Circuit," Mem. Facul. Eng. Kyoto Univ., Vol.39, Part 4, October (1977).

[57] Umoto, J., M. Yoshida, and K. Komaya: "Relaxation of Current Concentration at End of Diagonal MHD Generator," Convention Records at the Annual Meeting of I.E.E.J., No. 980, (1977).

[58] Yoshida, M., K. Komaya, and J. Umoto: "Analysis of End of Diagonal Type MHD Generator by Means of Equivalent Circuit," Convention Records at the Annual Meeting in Kansai District of I.E.E.J., No. G1-41, (1977).

[59] Yoshida, M. and J. Umoto: "Two Dimensional Analysis of Diagonal Type MHD Generator by Means of Equivalent Circuit (The 4th Report)," Convention Records at the Annual Meeting in Kansai District of I.E.E.J., No. G1-12, (1976).

[60] Yoshida, M. and J. Umoto: "Effect of Finite Segmentation of Electrode on Diagonal Type MHD Generator," Convention Records at the Annual Meeting of I.E.E.J., No.979, (1977).

[61] Yoshida, M. and J. Umoto: "Analysis of Generator Characteristics of Diagonal Type MHD Generator," Prep. 1977 Annual Meeting At. Energy Soc. Japan, A34, (1977).

[62] Yoshida, M. and J. Umoto: "Quasi-Two-Dimensional Analysis of Diagonal Type MHD Generator," MHD Symp. in Japan, pp. 99-104, (1978).

[63] Yoshida, M. and J. Umoto: "Quasi-Two-Dimensional Analysis of Diagonal Type MHD Generator," Trans. I.E.E.J., Vol.99-A, No. 3, pp. 105-112, (1979).

[64] Yoshida, M. and J. Umoto: "Two-Dimensional Analysis of Diagonal Type MHD Generator," Prep. 1978 Annual Meeting At. Energy Soc. Japan, B4, (1978).

[65] Yoshida, M. and J. Umoto: "Two-Dimensional Analysis of Diagonal Type MHD Generator Considering Boundary Layer," Convention Records at the Annual Meeting in Kansai District of I.E.E.J., No. G1-32, (1978).

[66] Yoshida, M. and J. Umoto: "Quasi-Two Dimensional Analysis of Large Scale Diverging Diagonal Type MHD Generator," MHD Symp. in Japan, pp. 209-215, (1979).

[67] Yoshida, M. and J. Umoto: "Quasi-Two-Dimensional Analysis of Large Scale Diagonal Type MHD Generator," Prep. 1979 Annual

Meeting At. Energy Soc. Japan, B6, (1979).

[68] Yoshida, M. and J. Umoto: "Quasi-Two-Dimensional Analysis of Diagonal MHD Generator," Convention Records at the Annual Meeting of E.E.E.J., No. 909, (1979).

[69] Yoshida, M. and J. Umoto: "Study on Improvement of Large Scale Diverging Diagonal Type MHD Generator," 2nd Symp. Energy Utilization and Direct Generation, (1980).

[70] Yoshida, M., T. Inui, and J. Umoto: "Characteristics of Multiple-Load Diagonal Type MHD Generator," Convention Records at the Annual Meeting of I.E.E.J., No. 906, (1980).

[71] Schlichting, H., "Boundary-Layer Theory," 6th ed., McGraw-Hill, New York, p. 146, (1968).

[72] Uchida, H., N. Isshiki, Y. Mori, T. Ueda, and Y. Katto: "Advanced Lectures on Heat and Mass Transfer," 3rd ed., Shoka-bo, Tokyo, (1977).

[73] Schlichting, H., "Boundary-Layer Theory," 6th ed., McGraw-Hill, New York, p. 612 and 676, (1968).

[74] Okada, M. and Y. Arata: "Plasma Engineering," Nikkan Kogyo Shinbun-sya, Tokyo, p.642, (1965).

APPENDIX I

QUASI-ONE-DIMENSIONAL ANALYSIS

As is well-known, the MHD flow in a diagonal type generator duct are described quasi-one-dimensionally by the conventional set of the mass continuity equation

$$\rho u A = m_0 \ , \tag{A.1}$$

the momentum equation

$$\rho u \frac{du}{dx} + \frac{dp}{dx} = J_y B - f, \tag{A.2}$$

the energy equation

$$\rho u \frac{d}{dx} \left(h + \frac{u^2}{2} \right) = E_x J_x + E_y J_y - q \ , \tag{A.3}$$

the state equation

$$p = \rho R T \ , \tag{A.4}$$

the Ohm's law (2.3) and the diagonal constraints (4.3).

In the above equations, f and q are the friction and the heat transfer losses, respectively, on the duct wall, which are given as follows [73]:

$$f = 2 \rho u^2 \, c_f / D \ , \tag{A.5}$$

$$q = \frac{4 \rho u \, c_p}{D} \frac{c_f}{2} \left(T_s - T_w \right) \left(1 + \beta_n \sqrt{c_f / 2} \right)^{-1}, \tag{A.6}$$

where

$$D = \sqrt{A}\ ,$$

$$\beta_n = 0.52\ (\rho\, u\, k_s \sqrt{c_f / 2}\ )^{0.45} P_r^{0.8}\ . \qquad \text{(A.7)}$$

Next, let us transform Eqs. (2.3) and (4.3) so as to contain effects of finite electrode segmantation and nonunifromity of the working gas plasma. First, when the former effect is considered, E_x and J_y can be expressed by the following equations

$$E_x = \frac{I_L \{ 1 + s_h c_4 + \beta^2 (1 + s_h c_4) \} - \sigma u B A \{ \beta (1 + s_h c_3) - a - s_h c_1 \}}{\sigma A \Delta}, \qquad \text{(A.8)}$$

$$J_y = \frac{I_L \{ -a + s_h c_2 - \beta (1 + s_h c_4) \} - \sigma u B A (1 + s_h c_1)}{A \Delta}, \qquad \text{(A.9)}$$

where

$$\Delta = 1 + s_h (c_3 + c_4) + s_h c_3 s_h c_4) - (s_h c_1 + a)(s_h c_2 - a)$$
$$+ \beta \{ (1 + s_h c_3)(s_h c_2 - a) + (a + s_h c_1)(1 + s_h c_4) \}\ , \qquad \text{(A.10)}$$

by applying Dzung's conformal transformation [32] to the diagonal type generator. In these equations, $s_h = s/H$, and c_1, c_2, c_3, and c_4 are the correction coefficients which are represented by u, u', v, and v', respectively, in Ref. [32].

Next, when we consider the plasma nonunifromity in the y-direction as in boundary layer, E_x and J_y are rewritten with Rosa's G factor [23] as follows:

$$E_x = \frac{I (G + \langle \beta \rangle^2) - \langle \sigma \rangle \langle u B \rangle A (\langle \beta \rangle - a)}{\langle \sigma \rangle A (G + a^2)}\ , \qquad \text{(A.11)}$$

$$J_y = \frac{I\,(\langle\beta\rangle + a) - \langle\sigma\rangle\langle u B\rangle A}{A\,(G + a^2)} \quad , \tag{A.12}$$

where

$$G = \langle\sigma\rangle\left\langle\frac{1+\beta^2}{\sigma}\right\rangle - \langle\beta\rangle^2 \quad . \tag{A.13}$$

In these equations < > denotes the average in the y-direction.

Lastly, when both effects of the finite electrode segmentation and the plasma nonuniformity are considered, from Eqs. (A.8) to (A.13), it is assumed that E_x and J_y are given by the following expressions

$$E_x = [\, I_L \{ G + s_h c_4 + \langle\beta\rangle^2 (1 + s_h c_4) \} + \langle\sigma\rangle\langle u B\rangle A \{ a + s_h c_1 - \langle\beta\rangle^2 (1 + s_h c_3) \}] \,/\, (\langle\sigma\rangle A \Delta) \tag{A.14}$$

$$J_y = [\, I_L \{ -a + s_h c_2 - \langle\beta\rangle(1 + s_h c_4) \} - \langle\sigma\rangle\langle u B\rangle A(1 + s_h c_1)] \,/\, (A \Delta) \tag{A.15}$$

where

$$\Delta = G + s_h(c_3 + c_4) + (a + s_h c_1)(a - s_h c_2) + \langle\beta\rangle\{(1 + s_h c_3)(s_h c_2 - a) + (a + s_h c_1)(1 + s_h c_4)\} \tag{A.16}$$

In addition, E_y and J_x are derived from Eqs. (4.3) and (A.14) to (A.16). In this connection,

$$E_y = a\, E_x \,, \tag{A.17}$$

$$J_x = \frac{I_L}{A} - a\, J_y \quad . \tag{A.18}$$

Besides, in the ideal generator, it is assumed that the electrode segmentation is infinitesimally small and boundary layer does not exist. Then in Eqs. (A.2), (A.3), and (A.14) to (A.16),

$$\left.\begin{aligned} f &= 0 \quad , \\ q &= 0 \quad , \\ s_h &= 0 \quad , \\ G &= 1 \quad , \end{aligned}\right\} \tag{A.19}$$

and < > is insignificant. In this connection, the output power P and electrical efficiency η_e are calculated by

$$P = -\int_0^L (E_x J_x + E_y J_y)\, A \, dx \quad , \tag{A.20}$$

$$\eta_e = \frac{P'}{-\int_0^L J_y \, u \, B \, dx} \quad , \tag{A.21}$$

respectively.

APPENDIX II

CALCULATION OF h'_{s1} IN EQ. (6.13)

In an adiabatic process, the following relation

$$dh = \frac{1}{\rho}\, dp. \tag{A.22}$$

is held. Since h is a function of p and T in the actual combustion gas as shown in Eq. (5.13), Eq. (A.22) is rewritten as

$$\frac{\partial h}{\partial T}\, dT + \frac{\partial h}{\partial p}\, dp = \frac{RT}{p}\, dp, \tag{A.23}$$

by using the state equation (6.4). Therefore,

$$\frac{dT}{dp} = \frac{\dfrac{RT}{p} - \dfrac{\partial h}{\partial p}}{\dfrac{\partial h}{\partial T}}. \tag{A.24}$$

Here, R is also the function of p and T as shown in Eq. (5.14). The boundary condition of Eq. (A.24) is, in the present case, given by

$$T = T_{s0} \quad \text{at } p = p_{s0}. \tag{A.25}$$

So integration of Eq. (A.22) yields

$$T'_{s1} = T_{s0} + \int_{p_{s0}}^{p_{s1}} \frac{\dfrac{RT}{p} - \dfrac{\partial h}{\partial p}}{\dfrac{\partial h}{\partial T}}\, dp, \tag{A.26}$$

where T'_{s1} is a stagnation temperature at the duct exit under the adiabatic process. Then h'_{s1} is numerically calculated by substituting the values of p_{s1} and T'_{s1} into Eq. (5.13) instead of p and T, respectively.